Adsorption of simple molecules on structured surfaces

Markus Lischka

Technische Universität München
Physik-Department T30
Univ.-Prof. Dr. A. Groß

Adsorption of simple molecules on structured surfaces

Markus Lischka

Vollständiger Abdruck der von der Fakultät für Physik der Technischen Universität München zur Erlangung des akademischen Grades eines

Doktors der Naturwissenschaften (Dr. rer. nat.)

genehmigten Dissertation.

Vorsitzender:		Univ.-Prof. Dr. U. Stimming
Prüfer der Dissertation:	1.	Univ.-Prof. Dr. A. Groß
	2.	Univ.-Prof. Dr. W. Brenig, em.

Die Dissertation wurde am 20. Februar 2003 bei der Technischen Universität München eingereicht und durch die Fakultät für Physik am 8. April 2003 angenommen.

Abstract

The adsorption of molecules on structured surfaces was studied using *ab initio* density-functional theory. The adsorption of H_2 and CO on the rather open Pd(210) surface is characterized and the corresponding binding energies and geometries are determined in the first part of this thesis. In contrast to low-index Pd surfaces, a molecular H_2 adsorption state is found to be stabilized by the presence of atomic hydrogen on the surface. The second part of this thesis is concerned with the chemical properties of pseudomorphic platinum multilayers on the Ru(0001) surface. The chemical reactivity as a function of the layer thickness is examined using the adsorption of atomic and molecular oxygen as well as carbon monoxide. The reactivity of the surface is changed by about the same magnitude through both the compression of the Pt multilayers as well as the direct interaction of the ruthenium substrate with the first two Pt layers.

Zusammenfassung

Mit Hilfe von *ab initio*-Dichtefunktionalrechnungen wurde die Adsorption von Molekülen auf strukturierten Oberflächen untersucht. Im ersten Teil der Arbeit wurde die Adsorption von H_2 und CO auf der offenen Pd(210)-Oberfläche charakterisiert und die entsprechenden Bindungsenergien und -geometrien bestimmt. Im Gegensatz zu ungestuften Pd-Oberflächen findet sich ein stabiler molekularer H_2-Adsorptionszustand bei mit Wasserstoff vorbedeckter Oberfläche. Im zweiten Teil der Arbeit wurden die chemischen Eigenschaften von pseudomorphen Platin-Multilagen auf der Ru(0001)-Oberfläche betrachtet. Anhand der Adsorption von atomarem und molekularem Sauerstoff sowie Kohlenmonoxid wurde die sich mit der Schichtdicke verändernde chemische Reaktivität untersucht. Die Reaktivität der Oberfläche wird dabei in gleicher Größenordung sowohl durch die Kompression der Pt-Multilagen als auch durch die direkte Wechselwirkung des Ruthenium-Substrats mit den ersten beiden Pt-Lagen beeinflusst.

Acknowledgments

First and most importantly, it is a pleasure to thank my supervisor, Prof. Dr. Axel Groß, for giving me the opportunity to work on this interesting and exciting topic. I am grateful for his constant support, the freedom I could enjoy over the past three years, and the chance to present and discuss my results at a number of conferences.

I would also like to thank my colleagues of the T30g group, Christian Bach, Areezo Dianat, Thomas Markert, Christian Mosch, Ata Roudgar, Sung Sakong, and Prof. Dr. Wilhelm Brenig, for all the interesting discussions we had together.

I owe a considerable debt to the experimental colleagues with whom I worked together: The Pd(210) adsorption experiments by Uwe Muschiol, Pia K. Schmidt and Prof. Dr. Klaus Christmann inspired the computations in Chapter 3. The adsorption calculations for nPt/Ru(0001) of Chapter 4 were motivated by simultaneous experiments of Andreas Schlapka, Dr. Peter Jakob and Prof. Dr. Dietrich Menzel. Without these close collaborations, the presented results would not have been possible.

Moreover, I wish to thank Georg Kresse, the main author of VASP, for the assistance with his enormous piece of software, and especially Andreas Eichler for providing me with his software tools for computing the orbital-resolved density of states and discussing some of the results with me. Special thanks also go to Thomas Voigtmann for answering (almost) all the software questions I had no answer to.

Most of the computational work was done on the high performance computing facilities of the Leibniz-Rechenzentrum within the t2101 project, and I am indebted to their administrative team for providing such an excellent computational working environment and support. Furthermore, I am thankful to Dr. Herbert Müller for helping out in all technical problems of the Physics Department's computer cluster.

Part of this work was supported by the Deutsche Forschungsgemeinschaft through Sonderforschungsbereich 338. Furthermore, I would like to acknowledge financial support by the European Science Foundation for my visits to the Ψ_k 2000 conference and the EURESCO conference on "Electronic Structure of Solids" 2001, by the Wilhelm und Else Heraeus-Stiftung for attending the DPG-Frühjahrstagungen 2000/2001/2002, as well as by the Leonhard-Lorenz-Stiftung for my visit to the APS March meeting 2002.

Finally, I would like to thank my family and my wife Elke for the support and encouragement over the past few years.

München
January 2003

Markus Lischka

Contents

Abstract iii

Zusammenfassung v

Acknowledgments vii

1 Introduction 1

2 Theoretical Background 3
- 2.1 Density-Functional Theory 3
  - 2.1.1 Kohn-Sham Equations 4
  - 2.1.2 Exchange-Correlation Functionals 6
  - 2.1.3 Plane Wave Basis Sets 7
  - 2.1.4 Pseudopotential Approximation 8
  - 2.1.5 Supercell Approach 10
- 2.2 Physical Properties and Concepts 12
  - 2.2.1 Geometry Relaxations 12
  - 2.2.2 Adsorption Energies and Potential Energy Surfaces 13
  - 2.2.3 Work Function 15
  - 2.2.4 Charge Density Analysis 16
  - 2.2.5 Density of States 17

3 Adsorption on a stepped surface: Pd(210) 21
- 3.1 The clean (210) surface 23
- 3.2 Atomic hydrogen adsorption on Pd(210) 28
- 3.3 Molecular hydrogen adsorption 32
- 3.4 CO adsorption 42
- 3.5 Coadsorption of H and CO 48

4 Adsorption on metal overlayers: nPt/Ru(0001) 51
- 4.1 Layer structure of nPt/Ru(0001) 52
- 4.2 Atomic adsorption of oxygen 59

4.3 Molecular adsorption of O_2 64
4.4 CO adsorption 69

5 Conclusions 75

A Numerical accuracy of DFT calculations 79

B Computer resources 87

Bibliography 89

List of Publications 101

List of Figures

2.1 Schematic illustration of the pseudopotential approximation 9
2.2 Supercell approach 11
2.3 Contour plots of the PES of H_2/Pd(100) 14
2.4 Charge density and density difference of the H_2 molecule 17
2.5 Splitting of H 1s level upon adsorption on Pd(210) 19
2.6 Illustration of the d-band interaction 20

3.1 Side and top view of the (210) surface 22
3.2 Bulk lattice constant of Pd 23
3.3 Pd(210): Layer-resolved LDOS 25
3.4 Interlayer distances of Pd(210) 27
3.5 Potential curve of the H_2 molecule 28
3.6 Potential energy surface of atomic hydrogen adsorption on Pd(210) . . 29
3.7 Hydrogen adsorption on Pd(210) for $\theta = 2$ and $\theta = 3$ 31
3.8 H-induced LDOS change of top Pd atom 31
3.9 Thermal desorption spectra of H_2/Pd(210) 33
3.10 Potential energy surfaces for H_2/Pd(210) 34
3.11 Potential energy surfaces for H_2/H/Pd(210) 36
3.12 Side view of the H_2/H/Pd(210) slab 37
3.13 LDOS analysis of the H_2/H/Pd(210) system. 38
3.14 Potential energy surface for H_2/H(O_d)/Pd(210) 39
3.15 Adiabatic reaction path energies for H_2 adsorption 39
3.16 Average electrostatic potential of H_2/H/Pd(210) 40
3.17 Electron density and density difference plot of H_2/H/Pd(210). 41
3.18 CO adsorption sites and bonding parameters on Pd(210) 44
3.19 Adsorption geometries for CO on Pd(210) 45
3.20 Adsorption geometry of CO/Pd(210) at a coverage of $\theta = 1.5$ 46
3.21 LDOS analysis of the CO/Pd(210) system. 47

4.1 Rigid band model 52
4.2 Side and top view of the 1Pt/Ru(0001) surface. 53
4.3 Stacking sequence of nPt/Ru(0001). 55

4.4 nPt/Ru(0001): Top-layer LDOS 57
4.5 Charge density and electrostatic potential of 5Pt/Ru(0001) surface . . 58
4.6 Atomic oxygen adsorption energies on nPt/Ru(0001) 60
4.7 Top view of the fcc hollow and hcp hollow adsorption geometry 62
4.8 Contours of constant charge density for $p(2 \times 2)$-O/nPt/Ru(0001). . . . 63
4.9 Side and top view of O_2^-/1Pt/Ru(0001) and O_2^{2-}/1Pt/Ru(0001) 65
4.10 O_2 molecular adsorption energies on nPt/Ru(0001) 66
4.11 O_2 adsorption energy versus d-band center 68
4.12 On-top CO adsorption energies on nPt/Ru(0001) 70
4.13 CO adsorption energy versus d-band center 72
4.14 Desorption temperatures of CO on nPt/Ru(0001) 73

A.1 Convergence of total energy with respect to plane wave energy cut-off . 80
A.2 Numerical errors due to basic set incompleteness 80
A.3 Convergence of total energy with respect to the number of **k** points . . 81
A.4 Numerical errors due to coarser finite FFT grids 83
A.5 Influence of the projection radius on the local DOS 84

List of Tables

3.1 Surface energy and work function of Pd(210) 24
3.2 Layer relaxations of the Pd(210) surface 26
3.3 Characteristic data of H_2 molecule 28
3.4 Adsorption energies for H/Pd(210) 30
3.5 Adsorption energies for H_2/Pd(210) 38
3.6 Characteristic data of CO molecule 43
3.7 Adsorption energies for CO/Pd(210) 44
3.8 Adsorption geometries for CO/Pd(210) 45
3.9 Adsorption energies for H and H_2 on CO/Pd(210) 48

4.1 Bulk properties of Pt and Ru 54
4.2 Layer relaxations of nPt/Ru(0001) 56
4.3 Computed d-band centers and work functions of nPt/Ru(0001) 58
4.4 Characteristic data of O_2 molecule 59
4.5 Adsorption energies and geometries for $p(2 \times 2)$-O/nPt/Ru(0001) . . . 61
4.6 Bond lengths for $p(2 \times 2)$-O/nPt/Ru(0001) 64
4.7 Adsorption energies and geometries for O_2/nPt/Ru(0001) 67
4.8 Adsorption energies and geometries for CO/nPt/Ru(0001) 71

Chapter 1

Introduction

> *Great stories, many of them true, are constructed about structures and reactions on the basis of a few evanescent bumps in an often hard-to-come-by spectrum.* [1]

Catalytic processes, or reactions at surfaces in general, are abundant in all aspects of our lives. Enzymatic catalysis constitutes the basis for most of the biochemical reactions of living beings, and more than 90% of the world's chemical manufacturing processes rely on one or more catalytic reactions [2].

The importance of catalytic surfaces, being promoters of a specific chemical reaction without being consumed themselves in the process, was already discovered almost two centuries ago. Around 1820, Davy observed that platinum surfaces greatly facilitate the oxidation of hydrogen to water [3]. Since then, a wealth of industrially relevant catalytic processes have been developed. One of the most prominent examples is the Haber-Bosch process [4]: At high pressures and temperatures, ammonia, NH_3, is synthesized from gas-phase nitrogen and hydrogen in the presence of an iron catalyst. Nevertheless, most of these traditional catalysts have been developed and improved by an empirical trial and error approach.

Although substantial scientific knowledge on reactions at surfaces and their influence on catalysis design had been obtained, a detailed explanation of the microscopic basis of catalysis, however, was still missing till the early 1960s. The advent of ultrahigh vacuum (UHV) technology finally allowed control of specific experimental conditions under which surfaces could be studied [5]. At last, adsorption experiments could be performed on well-characterized, clean surfaces. Together with the development of new electron spectroscopy methods, such as Auger spectroscopy, an experimental determination of the chemical species and its concentration on the surface was possible.

Since these early days of surface science, with the microscopic knowledge based on "a few evanescent bumps in an often hard-to-come-by spectrum" [1], significant experimental progress has been made [3]: A wealth of surface-sensitive techniques, from low-energy electron diffraction (LEED) to high-resolution electron energy loss spectroscopy (HREELS), are available for the study of surface species. For example, it is now possible to use ultrafast x-ray pulses to directly monitor a surface chemical reaction and probe changes in local bonding on a femtosecond time scale [6]. Moreover, direct manipulations of atoms became feasible with the invention of the scanning tunneling microscope (STM). It cannot only be used to assemble atoms in an arbitrary pattern, but also to induce reactions such as the oxidation of a CO molecule released from an STM tip near an adsorbed oxygen atom [7].

Furthermore, this experimental progress was accompanied by significant theoretical advances: *Ab initio* total-energy calculations based on electronic structure theory were able to enlighten and explain the geometrical and electronic structure of clean, low-index surfaces as well as reactions on these surfaces. Modern *ab initio* calculations might even be considered “a virtual chemistry lab” [2]: For instance, linear scaling electronic structure methods, also called $O(N)$ methods [8], or multiscale methods, which combine different methods from the quantum regime up to the continuum level, allow for ever larger system sizes and more realistic simulations [9]. Standard *ab initio* density-functional calculations are routinely applied to a wide range of problems, starting from combinatorial materials science [10] to biochemical systems such as the enzymatic synthesis of ammonia [11].

Nevertheless, both experimental and theoretical studies of surface reactions suffer from the so-called “structure gap” [12]. Real catalysts contain the reactive metal in a highly dispersed state as small particles, with a high concentration of steps and facet edges, whereas surface science studies traditionally concentrated on well-defined low-index surfaces. This is especially important as these defect sites are often assumed to be the catalytically active sites. It is thus not surprising that current experiments try to close this structure gap by using well-defined stepped surfaces as a more realistic model for a real catalyst. However, the reactivity of a surface is not only determined by its defect structures, but even more importantly by its electronic properties. Alloying a surface, or growing heteroepitaxial overlayers on a surface can significantly alter its reactivity.

In this thesis, we will address both of these issues using density-functional theory calculations for two systems recently investigated in adsorption experiments. The outline of this thesis is as follows: We start with an introduction to density-functional theory and its application to surface science problems. The main part consists of our results for adsorption of simple molecules on two different metal surfaces: In Chapter 3, adsorption of H_2 and CO on the stepped Pd(210) surface is studied and compared to experimental data by Muschiol et al. [13] and Schmidt et al. [14]. We then investigate the chemical properties of pseudomorphic platinum multilayers on the Ru(0001) surface as a function of the layer thickness in Chapter 4, using atomic and molecular oxygen as well as CO as probe molecules. These calculations allow for a disentanglement of the effect of lattice strain within the grown multilayers and of the residual electronic influence of the ruthenium substrate. They were motivated by and are compared to experiments of Schlapka et al. [15, 16]. We finally summarize our findings in Chapter 5.

Chapter 2

Theoretical Background

2.1 Density-Functional Theory

When studying molecules on surfaces, or chemical reactions in general, both static properties such as geometrical configurations or vibrational frequencies and dynamic properties such as sticking and diffusion are of interest. All these properties can be obtained from the full solution of the many-body Schrödinger equation. It is said that

> "... shortly after Schrödinger's equation for the electronic wave function Ψ had been put forward and spectacularly validated for small systems like He and H_2, P. M. Dirac declared that chemistry had come to an end – its content was entirely contained in that powerful equation. Too bad, he is said to have added, that in almost all cases, this equation was far too complex to allow solution." [17]

To solve the many-body Schrödinger equation, a whole machinery of methods was developed, starting from the Hartree-Fock approximation and leading to a zoo of modern quantum chemical models [18]. However, all these wave-function based methods have the severe limitation that the effort involved for computing and storing the wave function increases exponentially with the number of electrons. They are thus limited to problems with a rather small number of chemically active electrons.

In 1964, Hohenberg and Kohn [19] proposed the basic lemma of density-functional theory (DFT). Its main implication was the shift from the wave function to the ground-state density as the core variable, thus basing the theory on a simple three-dimensional function $n(\mathbf{r})$ instead of the multi-dimensional wave function $\Psi(\mathbf{r}_1, \mathbf{r}_2, \ldots, \mathbf{r}_N)$. This approach, despite the need for an approximation of the exchange-correlation functional, proved so successful that it became the standard approach for obtaining ground-state properties in solid-state physics and surface science over the past decades. It is now applicable with good accuracy to a wide variety of physical problems, such as molecule-surface interactions [20], phononic properties of crystals [21], or even to study the properties of liquid iron under Earth's core conditions [22].

In the following sections, we will briefly describe the fundamentals of density-functional theory and the numerical approximations involved in applying it to surface science problems. All calculations presented in Chapter 3 and 4 are done within this framework. It should be emphasized however, that although density-functional theory is in principal an exact theory, actual implementations of DFT are based on approximations of the exchange-correlation functional. Despite all its successes, its results thus need to be checked against experimental data or more evolved and accurate theoretical results, e.g., Quantum Monte Carlo computations [23].

2.1.1 Kohn-Sham Equations

The foundation for the theory of electronic structure is the time-independent, non-relativistic Schrödinger equation for the many-electron wave function Ψ,

$$E\Psi = \hat{T}\Psi + \hat{V}\Psi + \hat{V}_{\text{ext}}\Psi, \tag{2.1}$$

where $\hat{T}$ represents the kinetic energy operator, $\hat{V}$ the electron-electron interaction potential and $\hat{V}_{\text{ext}}$ any externally applied potential including the Coulomb interaction with the nuclei [17, 24]. This equation already incorporates the Born-Oppenheimer approximation that, due to the large mass mismatch between electrons and ions, the electrons are following the movements of the nuclei and staying in their respective ground state [25]. Ionic and electronic degrees of freedom are thus effectively decoupled, and ionic coordinates enter Eq. (2.1) only as parameters.

As Hohenberg and Kohn have first proven in their seminal paper [19], there exist two bijective maps,

$$n(\mathbf{r}) \mapsto |\Psi[n]\rangle\,, \qquad \text{and} \qquad n(\mathbf{r}) \mapsto V_{\text{ext}}(\mathbf{r}), \tag{2.2}$$

which establish unique one-to-one relations between the ground-state charge density and the corresponding wave function as well as the corresponding external potential. Using the Rayleigh-Ritz variational principle, the ground-state solution of the Schrödinger equation can be obtained by minimizing the energy with respect to a trial wave function and, by using Eq. (2.2), with respect to the charge density,

$$E_0 = \min_{\Psi} \langle\Psi| T + V + V_{\text{ext}} |\Psi\rangle = \min_{n(\mathbf{r})} E[n(\mathbf{r})], \tag{2.3}$$

where

$$E[n] = T[n] + V_{\text{H}}[n] + E_{xc}[n] + V_{\text{ext}}[n]. \tag{2.4}$$

$T[n]$ is the kinetic energy functional for non-interacting electrons and $V_{\text{ext}}[n]$ the functional of the external potential, respectively. $V_{\text{H}}[n]$ denotes the functional of the classical Coulomb interaction energy, i.e., the Hartree energy, given by

$$V_{\text{H}}[n] = \frac{1}{2}\int d\mathbf{r}d\mathbf{r}' \frac{e^2}{4\pi\varepsilon_0}\frac{n(\mathbf{r})n(\mathbf{r}')}{|\mathbf{r}-\mathbf{r}'|}. \tag{2.5}$$

All non-trivial many-body quantum-mechanical effects have been separated in $E_{xc}[n]$, the unknown exchange-correlation functional. It is this functional which needs to be approximated and determines the accuracy of any DFT calculation. The important advantage of this approach, however, is that $E_{xc}[n]$ is a well-defined functional dependent only on the three-dimensional charge density and universal with respect to the quantum-mechanical problems.

To actually solve Eq. (2.3), one typically writes the charge density as a sum of fictitious single-particle states,

$$n(\mathbf{r}) = \sum_{i=1}^{N} |\varphi_i(\mathbf{r})|^2 , \tag{2.6}$$

where N denotes the total number of electrons. Inserting this expansion in Eq. (2.3) and minimizing it under the constraint that all φ_i are normalized and orthogonal to each other leads to the set of Kohn-Sham equations [26],

$$\left[-\frac{\hbar^2}{2m} \nabla^2 + V_{\text{eff}}(\mathbf{r}) \right] \varphi_i(\mathbf{r}) = \varepsilon_i \varphi_i(\mathbf{r}). \tag{2.7}$$

The effective potential, V_{eff}, is given by

$$V_{\text{eff}}(\mathbf{r}) = V_H(\mathbf{r}) + V_{xc}(\mathbf{r}) + V_{\text{ext}}(\mathbf{r}), \tag{2.8}$$

with $V_{xc}(\mathbf{r}) = \frac{\delta E_{xc}[n]}{\delta n}$ being the functional derivative of the exchange-correlation functional with respect to the charge density. This set of coupled single-particle equations is almost identical to what one obtains by applying the simple Hartree approximation, i.e., writing the many-electron wave function as a product of single-particle wave functions,

$$\Psi(\mathbf{r}_1, \mathbf{r}_2, \ldots, \mathbf{r}_N) = \psi_1(\mathbf{r}_1)\psi_2(\mathbf{r}_2) \cdots \psi_N(\mathbf{r}_N), \tag{2.9}$$

and inserting it directly in Eq. (2.1). By doing so, the only absent term is the exchange-correlation potential, V_{xc}, and one thus misses all exchange and correlation effects. However, the approach of solving the set of coupled equations is similar: From an initially guessed electron density, the eigenfunctions φ_i are obtained as a solution of the Kohn-Sham equations where V_H and V_{xc} are computed using this initial guess. Mixing the resulting density with the old one, one obtains a better estimate of the correct charge density and again solves the Kohn-Sham equations. This procedure is repeated until one finally obtains a converged charge density within this so-called self-consistency cycle. Advanced mixing techniques, such as the modified Broyden's method [27], can significantly speed up convergence in such a self-consistency cycle by utilizing more than just the charge density of the current step and damping spurious Fourier components of the intermediate charge density. Finally, the self-consistent charge density is used to compute the ground-state energy as

$$E[n] = \sum_{i=1}^{N} \varepsilon_i - \frac{1}{2} \int d\mathbf{r}\, V_H(\mathbf{r}) n(\mathbf{r}) - \int d\mathbf{r}\, V_{xc}(\mathbf{r}) n(\mathbf{r}) + E_{xc}[n]. \tag{2.10}$$

2.1.2 Exchange-Correlation Functionals

Solving the Kohn-Sham equations, Eq. (2.7), requires knowledge of the correct form of the exchange-correlation functional, $E_{xc}[n]$. This functional comprises the many-body quantum-mechanical effects and is currently not known in a closed and analytic form. However, its form is universal and its asymptotic properties are thus at least derivable from the simplest many-body problem, the homogeneous electron gas.

The first attempt at obtaining a faithful representation of the exchange-correlation functional is the local density approximation (LDA) [28]:

$$E_{xc}[n] \approx \int d\mathbf{r}\, n(\mathbf{r})\varepsilon_{xc}(n(\mathbf{r})). \tag{2.11}$$

$\varepsilon_{xc}(n(\mathbf{r}))$ is the exchange-correlation energy per particle in a homogeneous electron gas, whose density is just taken to be the density at position $\mathbf{r}$. The LDA exchange-correlation potential is then a fully local function depending only on the density at position $\mathbf{r}$,

$$V_{xc}^{\mathrm{LDA}}(\mathbf{r}) = \frac{\partial}{\partial n} n\varepsilon_{xc}(n)\bigg|_{n=n(\mathbf{r})}. \tag{2.12}$$

The exchange-correlation energy itself can be obtained and parameterized using an interpolation scheme between analytic asymptotic behaviors and intermediate results based on quantum Monte Carlo calculations of the homogeneous electron gas [29]. The LDA already gives rather satisfactory results for lattice constants and geometrical configurations. Binding energies of molecules [30], and energy barriers for chemical reactions [31], however, are not accurate enough.

To improve the accuracy of the approximation enough to be applicable to surface science problems where one needs to compute adiabatic electronic properties of rather inhomogeneous systems, the gradient of the density has to be included in the approximation. Straightforward expansion of the exchange-correlation functional, however, has generally been disappointing when applied to real systems as the truncated series violates important physical properties such as the sum rule for the exchange-correlation hole [17, 24]. This is remedied in the construction of the generalized gradient approximation (GGA), where the exchange-correlation functional is written as

$$E_{xc}[n] = \int d\mathbf{r}\, n(\mathbf{r})\varepsilon_{xc}(n(\mathbf{r}), |\nabla n(\mathbf{r})|), \tag{2.13}$$

by obeying and making use of the appropriate sum rules, general scaling properties, and asymptotic behavior of effective potentials. Binding energies are significantly improved within the semi-local GGA functionals, and the absolute error for many small molecules is less than 0.3 eV [32]. All calculations reported in this thesis were being done using the GGA in the form proposed by Perdew and Wang (PW91) [33]. The PW91 functional leads to practically the same results as the simpler, but later proposed Perdew-Burke-Ernzerhof functional (PBE) [34].

It has to be noted that the search for a truly universal functional is far from over: There, e.g., exists a revised version of the PBE functional (RPBE) [35], and so-called meta-GGAs such as the PKZB functional [36, 37] which incorporate information about the kinetic energy density or the Laplacian of the charge density. These functionals are slightly closer to experimental data, but their general applicability remains to be seen. Moreover, in the field of theoretical chemistry, mostly hybrid functionals partially including exact exchange are employed, which significantly improve binding energies of small molecules, but fail to correctly reproduce extended systems such as metal surfaces [30, 32].

2.1.3 Plane Wave Basis Sets

It was demonstrated in the preceding sections that the many-body problem given by Eq. (2.1) can be effectively transformed into a set of quasi-single particle equations, Eq. (2.7). Solving these Kohn-Sham equations, however, still remains a formidable task for any solid-state system. For a system with a finite number of electrons, such as molecules or clusters, the Kohn-Sham equations might be solved using, e.g., a finite difference approximation on a real-space mesh [38]. For a periodic system, however, the natural choice is to expand the wave function in a discrete plane wave basis set,

$$\varphi_{\mathbf{k},i}(\mathbf{r}) = \sum_{\mathbf{G}} c_{i,\mathbf{k}+\mathbf{G}} \exp\left[i(\mathbf{k}+\mathbf{G})\cdot\mathbf{r}\right], \tag{2.14}$$

where $\mathbf{G}$ represent the reciprocal lattice vectors and $\mathbf{k}$ is supposed to lie within the first Brillouin zone. Plane waves as in Eq. (2.14) are already of the form required by Bloch's theorem. For practical purposes, the expansion at each $\mathbf{k}$ point has to be truncated at some kinetic energy cutoff,

$$E_{\text{cutoff}} = \frac{\hbar^2}{2m}\left|\mathbf{k}+\mathbf{G}\right|^2. \tag{2.15}$$

The quality of this approximation can then simply be controlled by enlarging E_{cutoff}.

For an infinite solid, the number of $\mathbf{k}$ points is infinite. As each occupied state at some given $\mathbf{k}$ point contributes to the electrostatic potential, one would have to solve the Kohn-Sham equations using an infinite number of plane-wave expansions of the form of Eq. (2.14). In practice, however, the wave function at $\mathbf{k}$ points close together will be almost identical so that it is possible to represent the total wave function using a finite number of $\mathbf{k}$ points. When choosing this $\mathbf{k}$ point set, it is desirable to exploit intrinsic symmetries and reduce any integration or summation to the irreducible part of the Brillouin zone. The most common sets of special $\mathbf{k}$ points are those first described by Monkhorst and Pack [39], which simply consist of an equispaced grid of $\mathbf{k}$ points. Thus, it is possible to compute any expectation value,

$$\langle X\rangle = \frac{1}{V}\sum_{n}\int_{V} d\mathbf{k}\, X_n(\mathbf{k}) f(\varepsilon_n(\mathbf{k})), \tag{2.16}$$

given by the integral over the volume V of the reciprocal unit cell and summation over all bands n, by simply replacing the integral with a finite summation of the chosen $\mathbf{k}$ point set. To improve the accuracy of this discrete approximation to the Brillouin zone integration, broadening methods such as the Methfessel-Paxton smearing [40] or an improved interpolation scheme such as the linear tetrahedron method [41] are employed. In surface science problems, one **k** point in the direction normal to the surface is sufficient due to the fact that no periodicity and thus no band dispersion is assumed in this direction. Therefore, one commonly uses a broadening approach, whereas interpolation methods would require more than one **k** point to be used in each direction.

Using a plane wave expansion, Eq. (2.7) is turned into a matrix equation,

$$\sum_{\mathbf{G}'} \left[\frac{\hbar^2}{2m} \left|\mathbf{k}+\mathbf{G}\right|^2 \delta_{\mathbf{G}\mathbf{G}'} + V_{\text{eff}}(\mathbf{G}-\mathbf{G}') \right] c_{i,\mathbf{k}+\mathbf{G}'} = \varepsilon_i c_{i,\mathbf{k}+\mathbf{G}}, \tag{2.17}$$

where the kinetic energy is diagonal and $V_{\text{eff}}(\mathbf{G}-\mathbf{G}')$ is the Fourier transform of the effective potential. The eigenvalues ε_i can be obtained by diagonalizing the Hamiltonian matrix of Eq. (2.17). The size of this matrix is determined by the chosen energy cutoff, and will be intractably large already for reasonably sized systems. Fortunately, using modern iterative algorithms, the explicit storage and direct diagonalization of the Hamiltonian matrix can be avoided [42].

The discussed approach is implemented in the Vienna *ab initio* simulation package (VASP) [43–46]: The wave function is expanded in plane waves on a finite **k** point mesh, and the resulting Hamiltonian matrix is iteratively solved either by a sequential conjugate gradient (CG) minimization or by a residual minimization method (RMM) using a direct inversion in the iterative subspace [45, 46]. Both methods yield identical results, but the RMM approach offers significant performance gains for larger systems.

Using a plane wave basis set also offers the advantage that the force $\mathbf{F}_I$ on an ion at position $\mathbf{R}_I$ can be computed easily using the Hellmann-Feynman theorem,

$$\mathbf{F}_I = -\frac{dE}{d\mathbf{R}_I} = -\frac{\partial E}{\partial \mathbf{R}_I}, \tag{2.18}$$

as derivatives of the basis set with respect to position of the ion, the so-called Pulay forces, happen to cancel each other for a plane wave basis set [42, 47]. This allows for an efficient and accurate geometry optimization.

2.1.4 Pseudopotential Approximation

Within the framework described in the previous subsection, the wave functions are expanded using a discrete set of plane waves. However, although Bloch's theorem guarantees the convergence of the expansion, this approach is rather inadequate for describing the rather tightly bound core electrons with their rapidly oscillating wave functions. All-electron computations thus usually separate core and interstitial regions and use different basis sets in both regions. One prominent example is the linearized augmented plane wave (LAPW) method where plane waves in the interstitial region are supplemented by a radial expansion of the wave function in the core regions (muffin-tin) [48]. These all-electron methods provide a very accurate description, but the numerical cost is rather high, especially for calculations involving transition metals and first-row non-metals.

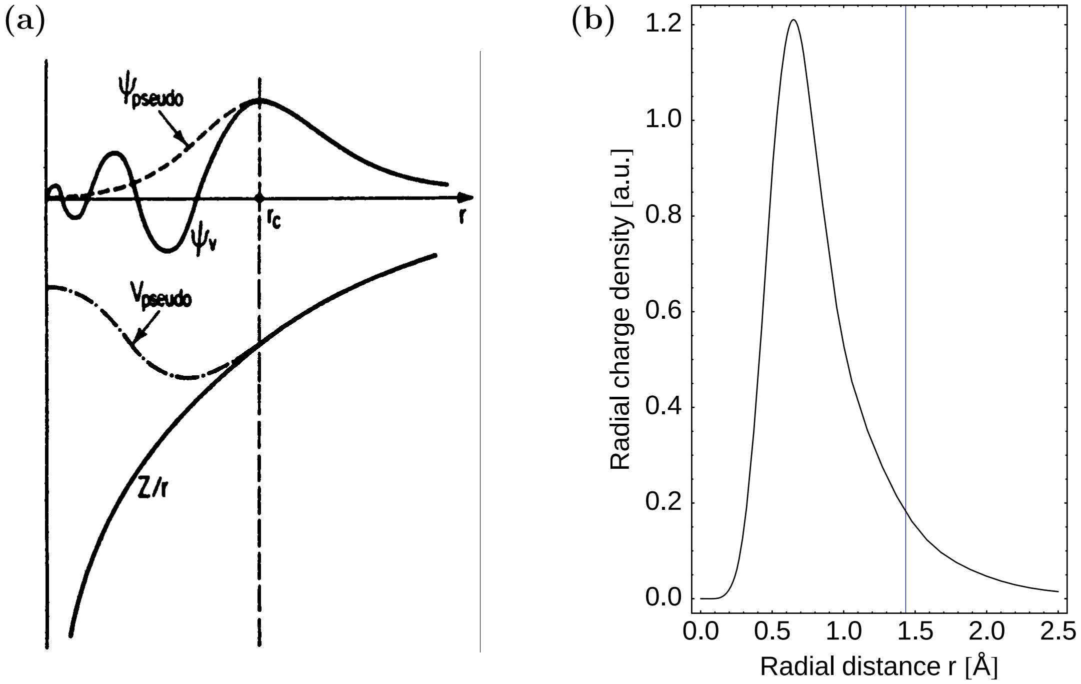

Figure 2.1: (a) Schematic illustration of the pseudopotential approximation. All-electron potential and wave function (solid lines) are replaced by their pseudo counterparts (dashed lines). The radius at which both values match is called the core radius, r_c [42]. (b) Pseudo charge density for the valence electrons of palladium. The core radius is at $r_c = 1.434$ Å.

For most physical systems, it is a well known fact that the properties of the solid, e.g., are much more dependent on its valence electrons than on its very localized core electrons [49]. It is thus desirable to exploit this fact and replace the core electrons together with the strong ionic potential by a weaker and smoother pseudopotential within the core region. This ansatz is illustrated in Fig. 2.1(a): Outside the core radius, r_c, both the pseudopotential and the pseudo wave function are identical to the true potential and wave function. Inside the core radius, all radial nodes of the wave function are removed, but at the same time preserving the norm of the wave function and all scattering properties of the full system. Norm-conserving pseudopotentials are of the form,

$$V_{\text{pseudo}}(\mathbf{r}) = \sum_{lm} |Y_{lm}\rangle \, V_l(\mathbf{r}) \, \langle Y_{lm}| \, , \tag{2.19}$$

where the spherical harmonics are denoted by $|Y_{lm}\rangle$, and are called semi-local as they are only local in the radial part, but non-local in the angular part. Efficient implementations of this pseudopotential approach for plane wave basis sets were proposed, for example, by Troullier and Martins [50] or Rappe et al. [51].

The use of norm-conserving pseudopotentials significantly reduces the computational effort by simultaneously maintaining an accurate description for most systems. For palladium, for example, the number of electrons to be dealt with in the computation is reduced from a total of 46 electrons to the 10 d electrons of Pd, and the resulting pseudo charge density as depicted in Fig. 2.1(b) is already rather smooth. By giving up the constraint of norm conservation, however, one can even further reduce the computational effort: This approach of using ultra-soft pseudopotentials (USPP) was first suggested by David Vanderbilt [52–54] and is implemented in VASP [55, 56]. The trade-off compared to traditional pseudopotentials is a rather complicated mathematical description as the Schrödinger equation is transformed to a generalized eigenvalue problem involving a nonlocal overlap matrix. The full, norm-conserving charge density itself has to be reconstructed using augmentation charges derived from the overlap matrix. Using Vanderbilt's approach, it is nevertheless possible to accurately describe transition metals with energy cutoffs as low as 200 eV.

Another approach to disentangle core and valence states is the so-called projector augmented-wave (PAW) method [57]. Its key idea is to introduce a linear transformation from the pseudo to the all-electron wave function. This linear transformation only differs from identity by a sum of local, atom-centered contributions acting only within augmentation regions enclosing the respective atom. One thus directly works with the all-electron wave function using radial support grids around each atom. Keeping the core states frozen, it is thus possible to almost achieve the computational efficiency of ultra-soft pseudopotentials, but at the same time preserving the accuracy of all-electron calculations under the constraint that the frozen core approximation is valid. It is indeed possible to show that Vanderbilt's USPP approach can be directly derived as a special, further linearized case of the PAW approach [58].

For most systems where the charge density distribution closely resembles that of the reference system of the isolated atom within the core region, both methods will yield almost the same numerical accuracy. However, for systems with large magnetic moments like iron or atoms such as oxygen where molecular bonding energies depend sensitively on the core charge density[35], the PAW approach clearly gives much better results and is almost capable of reproducing the accuracy of full all-electron computations at a much lower computational cost.

It has to be noted that, for both approaches, the pseudopotential is constructed from an exact all-electron calculation of the free atom. The transferability of the pseudopotential to molecular or bulk systems crucially depends on the chosen core radius and has to be explicitly verified. Furthermore, the exchange-correlation functional should be the same when constructing and applying the pseudopotential approximation as an inconsistent use might yield significant errors [59]. Both US and PAW pseudopotentials as supplied with VASP and employed in this work fulfill these requirements [55, 58].

2.1.5 Supercell Approach

To be able to employ Bloch's theorem and to use a plane wave basis set, the problem has to be periodic in all three spatial dimensions. For bulk metal calculations, this is naturally satisfied. By introducing a surface, however, periodicity in one direction is removed. Assuming the surface is normal to the z direction, one would have to deal

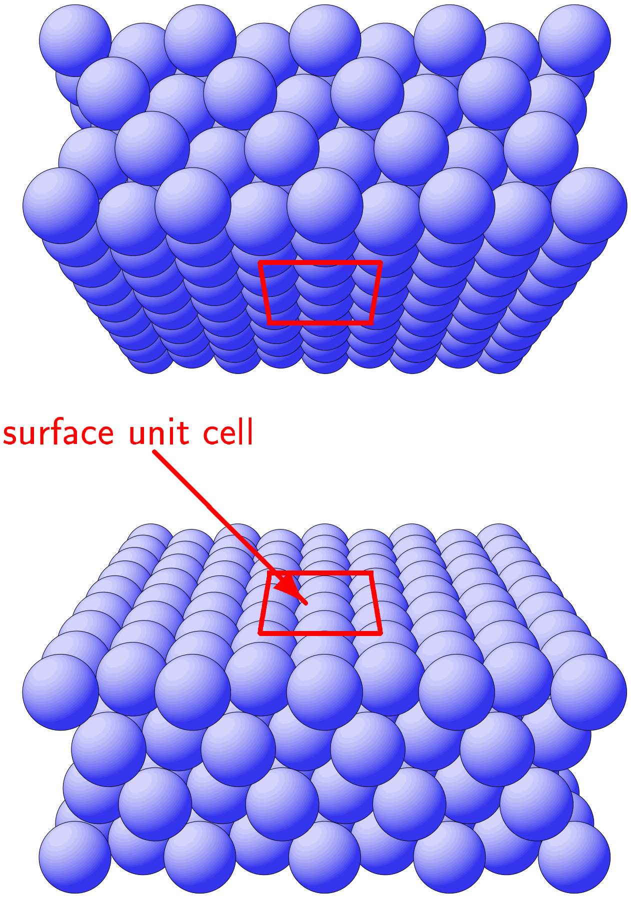

Figure 2.2: Supercell approach: A slab with a finite number of layers and a sufficiently large vacuum region are periodically repeated to model a metal surface [60].

with a semi-infinite bulk region and a semi-infinite vacuum region along the z axis with periodicity only preserved in the x-y plane [20].

In the so-called slab approach, however, one replaces the semi-infinite metal by a slab with two surfaces and a finite number of layers. By doing so, one obtains a two-dimensional lattice where the periodicity is given by the surface unit cell. To recover three-dimensional periodicity, the slab is now repeated in the z direction by adding a sufficiently large vacuum region in between them as illustrated in Fig. 2.2. This allows the computationally efficient expansion of the wave function in a plane wave basis set even for a non-periodic surface problem.

However, one has to check that this artificial supercell is still close enough to the physical reality: The vacuum region must be large enough ($\Delta z \geq 10$ Å) to separate both surfaces of the slab and to avoid any interactions of opposing surfaces or adsorbates. Moreover, the slab has to be thick enough to accurately model bulk states and any surface relaxations. For low-index metal surfaces, four or more layers are already sufficient to achieve convergence. Finally, the size of the surface unit cell has to be chosen such that it either corresponds to known experimental coverages or is large enough to exclude any lateral interactions between adsorbates.

2.2 Physical Properties and Concepts

Using the numerical methods described in Sec. 2.1 combined with current computing resources, it is possible to tackle a large range of surface science problems. In the following, we will briefly describe the general concepts and calculated physical properties especially used in theoretical studies of adsorption processes. Some of these properties are directly comparable to experimental data, e.g., adsorption energies or work function changes, and help to confirm experimental observations. Others such as the density of states are not only relevant for comparison to measured band structures or, within the Tersoff-Hamann picture [60], to scanning tunneling microscope (STM) images, but furthermore prove to be valuable theoretical tools to model and predict the reactivity of surfaces.

2.2.1 Geometry Relaxations

To correctly describe chemical reactions at surfaces, a reliable model of the surface needs to be employed. Using the slab approach described in Sec. 2.1.5, an accurate description in the surface plane including a proper infinite, periodic extension is easily available. Given a thick enough slab and vacuum region, it is also possible to reproduce the bulk properties of the examined metal.

The first crucial step when setting up the slab model is the determination of the bulk lattice constant. Numerically it is rather difficult to determine the precise energetical minimum of the cohesion energy with respect to the lattice constant. Given only small changes in the volume of the unit cell, errors in the total energy of a few meV might be introduced as the number of plane waves included in the finite basis set or the number of grid points used for the Fourier transforms of the charge density might change discontinuously with the unit cell volume (cf. Appendix A, [43]). To avoid these numerical errors, it is customary to evaluate the total energy per crystal unit cell for a set of distinct lattice constants separated by a few hundredth of an angstrom. The calculated total energies are then fitted to the Murnaghan's equation of state [61–63],

$$E(V) = E(V_0) + \frac{B_0 V}{B_0'(B_0' - 1)} \left[B_0' \left(1 - \frac{V_0}{V} \right) + \left(\frac{V_0}{V} \right)^{B_0'} - 1 \right], \tag{2.20}$$

where V is the volume, and B_0 and B_0' are the bulk modulus and its pressure derivative at the equilibrium volume V_0. This formula yields a good approximation for all cubic crystals.

As a second step, the surface slab is then constructed using this numerically self-consistent lattice constant. For the close-packed (111) and (100) surfaces, it is usually sufficient to include 4 or 5 bulk layers. However, the configuration in which the atoms are positioned at their bulk positions is not at its energetic minimum: At any surface, the electrons are rearranging their spatial distribution to compensate for the sudden change of electron density towards the vacuum. This results in a smoothing of the surface charge density, and in turn leaves the ion cores at a non-equilibrium position. For most metal surfaces, this smoothing leads to an inward relaxation of the first surface layer. For a faithful model of the surface, the slab layers thus need to be relaxed. This can be easily achieved by using the ionic forces computed with the Hellmann-Feynman theorem, Eq. (2.18), and thus optimizing the geometrical structure of the slab layers until the energetical minimum and, equivalently, a force-free situation is found.

If the adsorption process is modeled asymmetrically anyway, i.e., the atom or molecule is adsorbed only on one side of the slab, it is possible to improve the accuracy of the slab model by keeping layers one side of the slab fixed at their bulk position. Only the “top” half of the slab layers are allowed to relax. Although this sacrifices a correct description of the surface structure on one side, it slightly enhances the representation of sub-surface layers on the slab side on which the molecule is adsorbed.

Starting from such a fully self-consistent, force-free slab representation of the surface, it is now possible to search for atomic and molecular adsorption sites and obtain stable adsorption geometries: By fully relaxing the adsorbed molecule together with the top slab layers, one obtains a correct description of both the molecule geometry and any influence of the adsorbate on the surface structure. Bonding lengths and angles of adsorbed molecules, surface buckling or even adsorbate-induced surface reconstructions can thus be predicted.

The accuracy of geometrical data is already rather accurate even when only using the local-density approximation. Furthermore, the geometrical predictions are easily comparable to experimental data obtained, e.g., using low-energy electron diffraction (LEED) techniques.

2.2.2 Adsorption Energies and Potential Energy Surfaces

In DFT calculations of chemical reactions, it is always assumed that the electrons of the reactants are in their respective ground state and follow their nuclei adiabatically. This is true for most reactions, but there are important exceptions such as photo-chemical reactions or scattering processes involving charge transfer processes [64].

Given these constraints, one usually obtains the DFT total energy, $E[n]$, per super cell at a fixed set of ionic coordinates, $\{\mathbf{R}_I\}$. The adsorption energy per adsorbed atom or molecule can then be defined as the difference of the total energy of the adsorbate system and the total energies of the separated clean substrate and the adsorbing atom or molecule. For adsorption of H_2 on Pd(100), this gives, e.g.,

$$E_{\mathrm{ad}} = -\left(E[\mathrm{H_2/Pd(100)}] - E[\mathrm{Pd(100)}] - E[\mathrm{H_2}]\right). \tag{2.21}$$

Using this definition, a larger positive adsorption energy indicates a stronger attractive interaction between the surface and the adsorbate. For atomic adsorption, special attention has to be paid to where the energy reference is set to for the separated system. One may either use the total energy of the separated atom in the gas phase or the total energy of a stable compound. For atomic hydrogen adsorption, we will determine the adsorption energy per adsorbed atom as

$$E_{\mathrm{ad}} = -\left(E[\mathrm{H/Pd(100)}] - E[\mathrm{Pd(100)}] - \frac{1}{2}E[\mathrm{H_2}]\right). \tag{2.22}$$

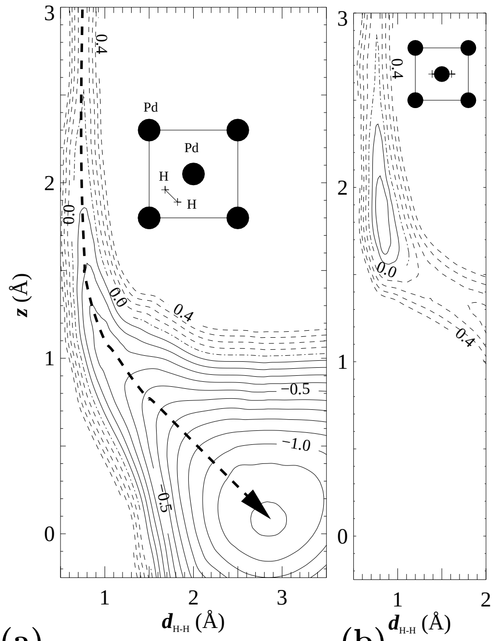

(a) (b)

Figure 2.3: Contour plots of the PES along two two-dimensional cuts through the six-dimensional coordinate space of H_2/Pd (100) (from [68]). The contour spacing is 0.1 eV per H_2 molecule.

The cost of breaking the bond of the stable H_2 molecule in the gas phase is thus already included. If the adsorption energy of Eq. (2.22) is positive, it is energetically favorable for an H_2 molecule to adsorb and dissociate in thermodynamic equilibrium.

These adsorption energies are then usually compared to experimental data obtained, e.g., by thermal desorption spectroscopy (TDS). It has to be emphasized, however, that the theoretical DFT total energy is related to these experimental quantities in a restricted way: The DFT total energy is computed at zero temperature, fixed volume, and fixed particle numbers. Moreover, ionic degrees of freedom are not treated quantum-mechanically. It thus corresponds to the Helmholtz free energy at zero temperature and neglects any zero-point vibrational energies [65]. Nevertheless, it usually is a good enough approximation to the correct physical energies.

Adsorption energies do not yet give a full picture of the adsorption process. Even when not performing dynamical simulations of the adsorption process [66], it is desirable to compute the potential energy of the adsorbate as a function of the coordinates of the nuclei using DFT. This quantity, $E(\{\mathbf{R}_I\})$, is called the potential energy surface (PES), a scalar function of all ionic coordinates. For adsorption calculations, it is often customary to assume that the substrate is rigid and its relaxation in the adsorption process is negligible. For a system like H_2/Pd(100), this is a good approximation due to the large mass mismatch between H and Pd. However, there are systems such as H_2 adsorption on Si where a movement of substrate ions, i.e., phonon-assisted sticking, is known to be essential for the adsorption process [67].

For diatomic molecular adsorption processes, the potential energy surface is usually plotted along two-dimensional cuts along high symmetry planes of the six-dimensional coordinate space (considering the substrate to be frozen). Two examples of such so-called "elbow plots" are depicted in Fig. 2.3. Shown are two sections of the PES of H_2 adsorption on Pd(100): The energy contours are plotted as a function of the bond length between the two hydrogen atoms, $d_{\mathrm{H-H}}$, and the height of the center of mass of H_2 above the first surface layer, z. The other four degrees of freedom of the approaching molecule, i.e., its orientation and lateral position within the unit cell are indicated by the inset with respect to the surface Pd atoms.

Such sections of high-symmetry planes often yield much more information than adsorption energies alone: A molecule fixed to the orientation of Fig. 2.3(a) with small kinetic energy would follow the reaction pathway indicated by the dashed arrow. Along this pathway, the potential energy is continually decreasing and the molecule can thus spontaneously dissociate without any hindering barrier. The existence of such non-activated pathways is typical for H_2 adsorption on Pd surfaces. For other initial configurations, as shown in Fig. 2.3(b), the molecule is hitting a barrier and obviously being trapped in a potential energy minimum when approaching the surface over an on-top position. However, the two-dimensional minimum is actually a saddle point in the six-dimensional configuration space and the molecule can thus move further along its reaction path by moving laterally away from the on-top position.

Elbow plots of the potential energy surface therefore help in identifying activated or non-activated pathways, barrier regions and transition states along the reaction path. They, however, only show a restricted subset of the true multi-dimensional PES and the true dynamics of the molecular adsorption process.

2.2.3 Work Function

Another directly accessible variable in surface experiments is a change of the work function induced by adsorbing molecules on a metal surface. The computed work function is thus another piece of information that might be compared to experimental data and be used to test the validity of a DFT calculation.

Theoretically, the work function of a specific metal surface is defined as the difference of the vacuum potential infinitely far away from the surface and the Fermi level [69],

$$\Phi = V(z \to \infty) - \varepsilon_F. \tag{2.23}$$

The potential value at $z \to \infty$ is mainly determined by the charge rearrangements of electrons and ions near the surface, i.e., the formation of a "double layer". Changes in the work function thus allow indirectly to reason on any polarization present in the molecule-substrate interaction.

In a DFT calculation using the supercell approach, the computation of the work function has to be done carefully: The vacuum region has to be chosen large enough so that the electrostatic potential is allowed to relax to its real vacuum level resulting in a truly flat potential. Furthermore, the Fermi level has to be determined accurately enough. If molecules are adsorbed on one side of the slab only, or if the slab is relaxed asymmetrically, there is a further difficulty: At the adsorbate-covered side of the slab, a dipole moment will build up affecting the vacuum level. But given the enforced periodicity of the supercell approach, this dipole moment will be compensated on the other side of the slab resulting in an implied macroscopic electrostatic field across the vacuum region. In an asymmetric supercell setup, it is therefore not possible to directly determine the physical vacuum levels and thus the corresponding work function. To avoid the computational cost of a symmetric setup, implying a thicker slab, one applies a trick and artificially "remedies" the periodicity of the supercell approach. A planar dipole layer is introduced in the middle of the vacuum region to counterbalance the induced electrostatic field. Its dipole strength is calculated self-consistently such that any intrinsic dipole moment is compensated for [70]. The introduction of this dipole layer is possible as there is no charge density present in the vacuum region. Using the described procedure, the left and right side of the slab are effectively decoupled yielding the correct vacuum levels corresponding to their respective surface (cf. Fig. 3.16, where the compensating dipole layer is located right in the middle of the vacuum region at $z = 0.0$ Å).

It is thus possible to compute the work function even in a convenient asymmetric setup. Depending on the adsorbate, the induced difference in the vacuum levels and thus the correcting dipole layer can be quite substantial. Binding energies of adsorbates, for instance, are nevertheless only slightly affected. The error in the binding energy due to the build-up of a dipole moment in an asymmetric situation is usually just a few meV.

2.2.4 Charge Density Analysis

In the previous subsections, we have summarized the most important physical properties that can be obtained by employing density-functional theory calculations. These properties either describe the geometry of the adsorbate-covered surface or the process of bond breaking and formation energetically. They do not however give any insight on how and why adsorption takes place in the context of any quantum-mechanical interaction of the adsorbate's and substrate's electrons.

The most directly available quantity for any analysis of the chemical interactions is the charge density, being the core variable in density-functional theory. The formation of bonding and anti-bonding levels will be directly reflected in the electron density, $n(\mathbf{r})$, as an accumulation or depletion of electrons. This is illustrated in Fig. 2.4(a) for the simple case of an isolated H_2 molecule: There is a distinct charge accumulation between the two hydrogen atoms due to the formation of the bonding σ orbital.

For more complex systems, redistributions of the charge density are not as easily identifiable. In this context, looking at the electron density difference of the coupled and uncoupled system is much more worthwhile. Theoretically, it does not pose any difficulty to "turn off" the interaction between, e.g., an adsorbed molecule and the metal substrate. One can easily compute the charge densities of the molecule and the substrate separately, but at the positions of the interacting adsorbate-substrate system. The electron density difference can then easily be computed as

$$\Delta n = n(\text{interacting system}) - \sum_i n(\text{non-interacting subsystem } i). \tag{2.24}$$

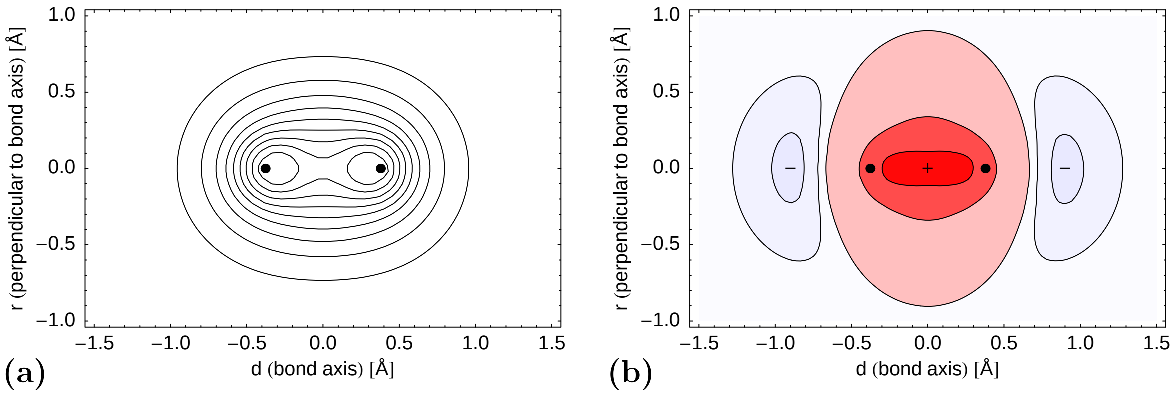

Figure 2.4: (a) Charge density plot of the H_2 molecule obtained within the GGA approximation. The positions of the nuclei are marked by dots. Contour lines are drawn at 10%, 20%, . . . , 90% of the maximum charge density. (b) Charge density difference plot of the H_2 molecule with respect to two non-interacting hydrogen atoms. Electron charge flows from outer regions (−) to the bond region (+). Contour lines are drawn at 50% and 90% levels of the difference minimum or maximum, respectively.

For the bonding of the H_2 molecule, where the two non-interacting subsystems are just the two hydrogen atoms, the resulting density difference is plotted in Fig. 2.4(b). The charge accumulation in the bonding region is now clearly visible, but also the charge depletion of the σ^* orbital to the left and right of the hydrogen atoms. It is thus possible to localize any interaction in real space and get an idea about induced charge redistributions and hybridizations of the interacting system.

The analysis of the charge density can even be pursued further along the ideas of the "atoms in molecules" theory [71, 72] or by directly classifying bonds on a topological basis through the use of the electron localization function (ELF) [73–75]. In this thesis, however, we will stick only to the basic charge density analysis.

2.2.5 Density of States

A more direct view on the interaction of any adsorbate with its substrate is possible by looking at the density of states (DOS). This quantity is directly accessible in DFT calculations, and is defined as

$$N(E) = \sum_{i=1}^{\infty} \delta(E - \varepsilon_i), \tag{2.25}$$

where the sum extends over all eigenstates of the Kohn-Sham Hamiltonian, Eq. (2.7). For a computation with a finite number of eigenstates, this distribution is usually smeared out to get a continuous distribution appropriate for a bulk material, e.g., using a Gaussian or Methfessel-Paxton smearing (cf. Appendix A). The total density of states given in Eq. (2.25) comprises all electrons of the system. In a bond breaking–bond formation process, however, we are typically interested in what happens to the electronic orbitals of the directly involved orbitals of the molecule and the metal partners. Most of the time, this information cannot be identified clearly in the total density of states. It is thus desirable to decompose the DOS into its "building bricks", e.g., the atomic valence orbitals. This can be achieved by computing the state-resolved, or projected DOS as defined by [1, 65, 76]

$$n_\alpha(E) = \sum_{i=1}^{\infty} \left|\langle\phi_\alpha|\varphi_i\rangle\right|^2 \delta(E-\varepsilon_i), \tag{2.26}$$

where ϕ_a is a properly chosen localized function. In a plane wave basis, the wave function is usually truncated to a sphere around an atom and then projected onto the respective atomic s, p, and d orbitals (see Appendix A, [77]). By doing this decomposition, the formation of bonding and anti-bonding hybridization orbitals can be traced down to their atomic origin.

It has to be noted however that the physical meaning of the eigenvalues of Eq. (2.7) is not immediately obvious. Within the framework of density-functional theory, the eigenvalues ε_i only represent eigenenergies of non-interacting quasi-particles, and only their sum, as it enters in Eq. (2.10), is of physical relevance. Furthermore, when solving the Kohn-Sham equations in practice, the exchange-correlation functional will have to be approximated and the obtained eigenenergies of the Kohn-Sham eigenstates will vary according to the chosen approximation of the functional. It can be shown, however, that at least the highest eigenvalue corresponds to the ionization energy of the system or the work function of the metal [28]. In contrast to Hartree-Fock theory, there is no direct relation between an eigenenergy ε_i and the energy required to remove an electron from that orbital i.

There is thus no theoretical justification for the use of the eigenenergies and thus the density of states to be interpreted in the sense of excitation energies or single-electron levels. In practice, however, this is common practice and the errors introduced in such an approach are usually acceptable [28]. For the qualitative analysis of bond formation and breaking, the applicability of the DFT DOS spectrum to the real energy spectrum has proven to be good enough. Nevertheless, one has to keep in mind that any quantitative results will depend on the choice of the exchange-correlation functional.

One of the main goals of surface science is to predict the reactivity of a surface based on its properties alone — without any knowledge of the interacting adsorbate-metal system. The density of states turned out to be a rather successful analysis tool in this regard. When talking about reactivity in this context, it is meant that the more reactive a metal surface is, the larger is the binding energy of an arbitrary adsorbate. In catalysis, on the other hand, "reactivity" usually denotes the overall throughput or effectiveness of the catalytic material which might even be adversely affected by larger binding energies.

Early reactivity concepts were based on the observation that the Pauli repulsion of, e.g, the s electrons of an adsorbing H_2 molecule is reduced by the availability of empty d states near the Fermi level. The local density of states at the Fermi level, $N(\varepsilon_F)$,

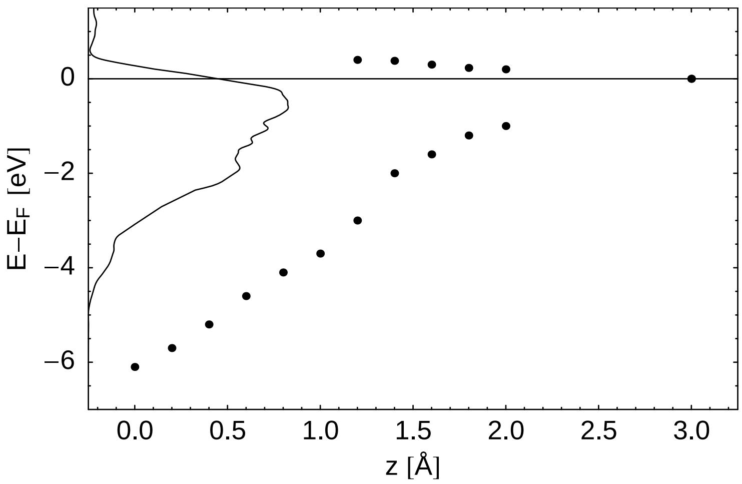

Figure 2.5: Splitting of H 1s level upon adsorption on Pd(210). At $z \approx 1.2$ Å, a clear and distinct bonding resonance peak begins to form at the lower edge of the d-band. The anti-bonding resonance peak in the DFT-computed LDOS gets rather broad and small for $z \leq 1.0$ Å and is thus no longer shown. The (smoothed) d-band density of states of the top Pd atom is shown for comparison along the left axis.

or some average around the Fermi level were thus correlated with the reactivity of the respective metal [78, 79]. Unfortunately, this model proved too simple as there exist examples where a metal with a very low DOS at the Fermi level still exhibits a rather large reactivity.

Instead, another approach was found to be applicable to a wide spectrum of metal surfaces and adsorbates: When an atom or molecule approaches a surface, its atomic or molecular orbitals, which are close to the Fermi level, interact with the metallic valence states and hybridize. For example, the hydrogen 1s level as shown in Fig. 2.5 splits into a bonding and an anti-bonding resonance level due to the interaction with the metal valence electrons. In the final adsorption geometry, a bonding resonance below the metal d-band and an anti-bonding resonance just above the d-band are present. The net result is a strong binding of the atom if the Fermi level is below the anti-resonance peak.

This adsorbate-surface interaction can be separated and is most conveniently considered in a two step process as suggested by Hammer and Nørskov [80]. First, the interaction of the orbital of interest with the metal s and p states leads to a broadening and a down-shift to lower energies of the respective orbital. This first step thus yields a net energy gain. Secondly, the renormalized energy level splits and hybridizes with the metal d-band as shown in Fig. 2.6. Depending on the position of the Fermi level, the anti-bonding state is then empty, partially occupied or completely filled. The filling of the anti-bonding level then decides about the net energy gain of this second step.

The discussed effect can be described quantitatively by introducing the center of the d-band as defined by

$$\varepsilon_d = \frac{\int_{-\infty}^{\infty} E\, n_d(E)\, dE}{\int_{-\infty}^{\infty} n_d(E)\, dE}, \tag{2.27}$$

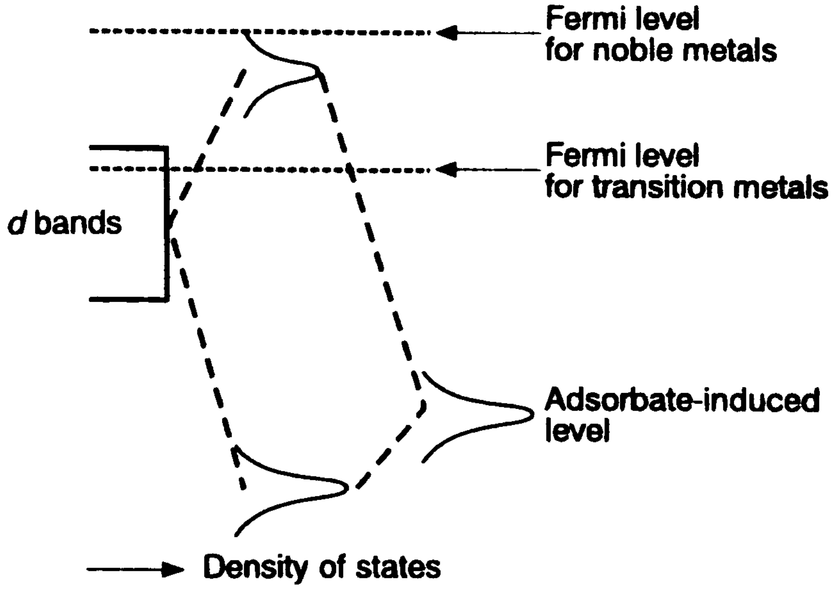

Figure 2.6: Illustration of the interaction of a renormalized adsorbate level with the metal d-band. The down-shift of the bonding level is smaller than the up-shift of the anti-bonding level due the energy cost related to the orthogonalization of the two levels. The overall energy gain of the hybridization is determined by the filling of the anti-bonding level and thus by the position of the Fermi level [80].

where $n_d(E)$ is the density of states projected onto d orbitals. Using results from effective-medium theory [81–83], it can be justified to quantify any change in the interaction energy by a change in the density of states alone. It is then possible to derive a perturbation expression for the change of the chemisorption energy due to the hybridization with the metal d states and approximately determine the coupling matrix. Within this d-band model [80, 83–87], the interaction between an adsorbate level of filling f_a at energy ε_a and a metal d-band of filling f_d with its center at ε_d is determined to be approximately

$$\Delta E = -C(f_a, f_d)\frac{V_{ad}^2}{|\varepsilon_d - \varepsilon_a|} + \alpha V_{ad}^2, \tag{2.28}$$

given a weak coupling ($|V_{ad}| \ll |\varepsilon_d - \varepsilon_\mathrm{a}|$). The first term of Eq. (2.28) describes the energy gain due to resonant interaction, the second term the energetic cost of the orthogonalization. Assuming a constant filling of the d-band and a constant coupling matrix V_{ad} for different but similar configurations, it is only the distance $|\varepsilon_d - \varepsilon_a|$ that determines the energy gain. In its simplest form, the d-band model then yields a linear relationship by applying a Taylor expansion in $\Delta\varepsilon_d$ between a shift in the d-band center and the chemisorption energy,

$$\Delta E = E_0 + \gamma\Delta\varepsilon_d. \tag{2.29}$$

For most adsorbates, Eq. (2.29) translates into the simple rule that the closer the center of the d-band, ε_d, is to the Fermi level, ε_F, the more reactive will be the particular surface or surface site.

Chapter 3

Adsorption on a stepped surface: Pd(210)

In the field of surface science, the study of the interaction of molecules with metal surfaces has traditionally focused on low-index surface planes. The experimental preparation of these well-defined surface in ultra-high vacuum (UHV) chambers and the subsequent adsorption of molecules on them has been a remarkable success over the past decades. On the other hand, however, the surfaces of all technologically relevant catalysts are created as non-ideal, defect-rich surfaces and operated under high pressures. These discrepancies between real-world applications and basic research are called the "structure and pressure gap".

It is a widely known fact that imperfections of the surface, e.g., steps or defect sites, help promote the reactivity of a catalyst. One way to bridge this structure gap between surface science and applied heterogeneous catalysis is to carry out experimental and theoretical studies on well-defined structured surfaces, such as vicinal surfaces of the low-index surface planes, and thus identify the effect of a particular defect structure on the surface reactivity.

In particular, the adsorption of hydrogen on metal surfaces has been studied extensively, both experimentally [88] and theoretically. Hydrogen adsorption served as a model system for analyzing the reactivity of different surfaces and determining the fundamental reaction steps. There exists a wealth of theoretical DFT studies on both atomic and molecular hydrogen adsorption on the (111) [89–91], (100) [68, 77, 92–96], and (110) [97] surfaces of palladium. Based on these DFT studies, dynamical aspects of the adsorption process were also thoroughly studied [66, 98–100]. As far as the H_2/Pd system is concerned, the usefulness of the DFT approach is clearly established and agrees very favorably with experimental results.

Based on these results on the low-index surface planes, it is natural to expand the scope of investigation to a more complex scenario that offers a more realistic descrip-

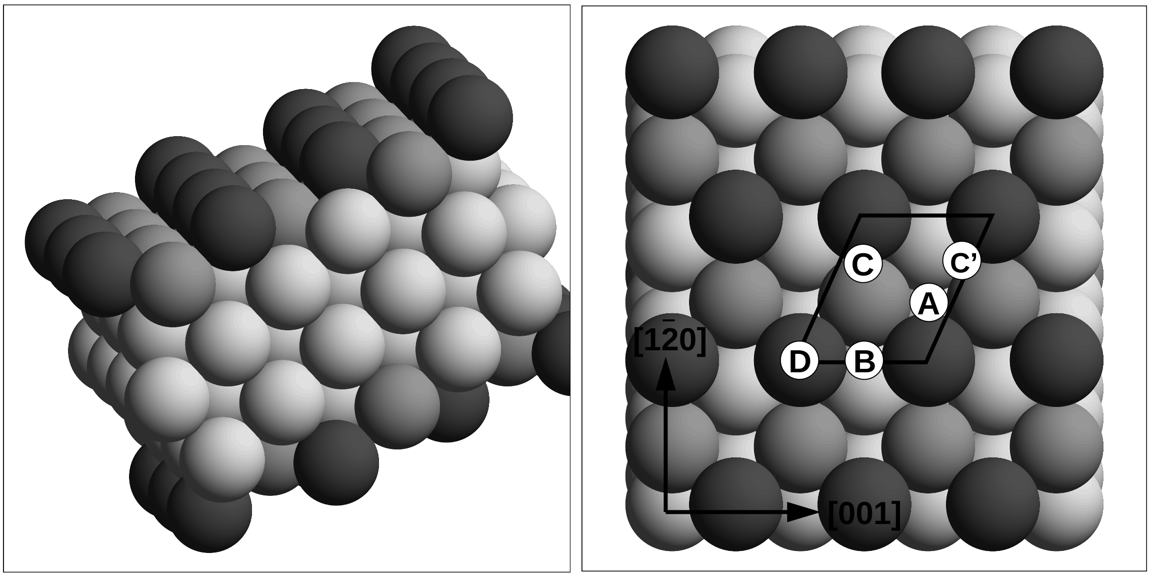

Figure 3.1: Side and top view of the (210) surface. In the right panel the surface unit cell plus the three atomic adsorption sites A, B, and C/C' are included. The site D corresponds to the molecular adsorption site.

tion of an "imperfect" real-world system, but still is simple enough to be reproducible and analyzable both experimentally and theoretically. The Pd(210) surface is such a system, and in this chapter, we will present results of DFT calculations on this surface. The (210) surface is a relatively open surface that can be regarded as a stepped surface with a high density of steps. The geometry of this surface is shown in Fig. 3.1. Vicinal fcc(n10) surfaces have (100) terraces with steps running along the [001] direction and forming open (110)-like microfacets. The theoretical study of this system was motivated by recent experimental results [13, 14, 101, 102]: Due to its specific structure, this system exhibits unique adsorption properties. Three atomic and two molecular adsorption states were identified on Pd(210) for adsorption below 100 K. This is especially remarkable as hydrogen dissociates spontaneously on all low-index Pd surfaces. Unfortunately, as the adsorption of hydrogen on this surface does not lead to any superstructure in low-energy electron diffraction (LEED) experiments, it is experimentally very difficult to identify the exact location and nature of the hydrogen adsorption states. In order to obtain this microscopic information, theoretical calculations are needed.

The outline of this chapter is as follows. In the next section we briefly summarize how the Pd(210) surface is treated computationally within our density-functional theory approach and discuss layer relaxations of the clean (210) surface. The next two sections, Sec. 3.2 and 3.3, contain the results for atomic and molecular hydrogen adsorption, respectively. Finally, CO adsorption and its effect on hydrogen adsorption will be discussed in Sections 3.4 and 3.5.

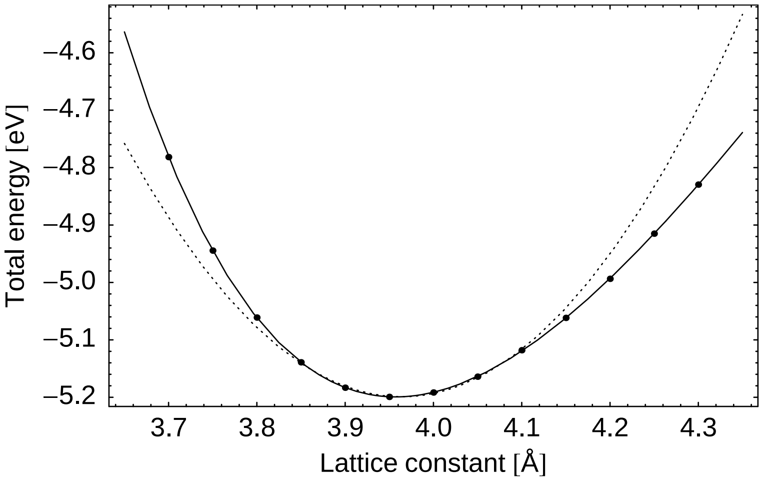

Figure 3.2: Bulk lattice constant of Pd. The solid line is a fit of the Murnaghan equation of state, Eq.(2.20), to the computed total energies per primitive unit cell. For comparison, a harmonic fit to the data around the energy minimum is shown as a dashed line. The minimum of the fit and thus the DFT equilibrium lattice constant is located at $a_0 = 3.95725$ Å.

3.1 The clean (210) surface

Ab initio density-functional theory calculations were used to determine all the structural, electronic and energetic results presented in this chapter. As outlined in Chapter 2, the Kohn-Sham equations were solved in a plane-wave basis set using the Vienna *ab initio* simulation package (VASP) [43, 45, 46, 55] and employing the generalized gradient approximation (GGA) of Perdew and co-workers (PW91) [33]. The electron-ion interaction was described by ultra-soft Vanderbilt pseudopotentials [52] as described in Sec. 2.1.4. To model the surface, the slab supercell approach with periodic boundary conditions was used: The Pd(210) surface is described by periodic slabs of either 11 or 21 layers and a separating vacuum region of 11 Å as depicted in Fig. 3.1.

For a (1 × 1) surface unit cell of Pd(210), we used a Monkhorst-Pack **k** point set [39] of $7 \times 7 \times 1$, corresponding to 16 **k** points in the irreducible Brillouin zone, together with a first-order Methfessel-Paxton smearing [40] of width $\sigma = 0.1$ eV. All reported total energies were extrapolated to $\sigma \to 0$ eV. Relaxation calculations were carried out with a conjugate-gradient minimization using the Hellman-Feynman forces computed at a larger **k** point set of $11 \times 11 \times 1$ (36 **k** points in the irreducible zone) to ensure full convergence of the forces. The plane wave expansion was truncated at an energy cutoff of 200 eV (14.7 Ry) which proved sufficient to obtain converged total energies. Further details on the numerical accuracy and convergence of the DFT calculations are summarized in Appendix A.

The first step of any surface calculation has to be an accurate determination of the equilibrium lattice constant of the bulk crystal. It is necessary to determine the lattice constant self-consistently if one wants to perform an accurate calculation of layer relaxations. Otherwise, a small error in the lattice constant would lead to horizontal forces pushing the slab layers artificially apart or pulling them together. The bulk lattice constant of Pd was determined as discussed in Sec. 2.2.1: Fitting the Murnaghan equation of state to the computed total energies per primitive unit cell yields a GGA equilibrium lattice constant of 3.95725 Å. The obtained value is thus slightly larger (1.7%) than the experimental lattice constant of 3.89 Å [103]. The bulk modulus of Pd is determined to be 165.9 GPa, compared to the experimental value of 181 GPa [103]. Computing the lattice constant with a larger **k** point set and using the more accurate linear tetrahedron method instead of Methfessel-Paxton smearing results in a lattice constant of $a_0 = 3.96083$ Å. The numerical errors in the lattice constant, ignoring the overall error due to the exchange-correlation functional, are thus very small, and, most importantly, negligible in comparison to the expected absolute layer relaxations.

To determine the surface properties shown in Table 3.1 and Fig. 3.3, both an 11 and 21 layer slab was used and allowed to relax freely until the absolute values of the forces on each atom were smaller than 0.02 eV/Å. It was found that the 11 layer slab was sufficient to reproduce all surface properties and layer relaxations correctly compared to the larger 21 layer slab.

The given work function is determined using the approach of Sec. 2.2.3. Relaxing the (210) surface effects changes the work function by less than 0.05 eV. Surface energies (in units of eV/atom) [104–106] were obtained from

$$\sigma = \frac{1}{2}\left(E_{\text{slab}} - N_{\text{atom}} E_{\text{bulk}}\right), \tag{3.1}$$

where E_{slab} is computed using the primitive surface unit cell, N_{atom} is the number of atoms in the slab model and E_{bulk} is the total energy of the respective bulk primitive unit cell. For comparison with other surface orientations, the surface energy is also stated in units of J/m^2 in Table 3.1. Compared to the experimental value for a polycrystalline sample, it is significantly smaller, although one would expect higher surface energies the less close-packed the surface is. Computing the surface energy for the (111) and (100) surface using a similar setup, however, yields $\sigma_{(111)} \approx 1.3$ J/m^2 and $\sigma_{(100)} \approx 1.5$ J/m^2, respectively. The expected trend is thus clearly observed, and GGA-USPP calculations seem to underestimate the surface energy.

That an 11 layer slab is also sufficient for representing the electronic structure of the (210) surface can be seen by looking at the layer-resolved local density of states (LDOS). The LDOS of the first three Pd layers are shown in Fig. 3.3. The data was obtained as described in Sec. 2.2.5 and Appendix A. A clear trend from the narrower

Table 3.1: Surface energy and work function of Pd(210) in comparison to experimental data. For a comprehensive comparison of surface energies computed using theoretical methods, see Methfessel et al. [104], Vitos et al. [105] or Mehl and Papaconstantopoulos [106].

		Surface energy		Work function	
	Surface	[eV/atom]	[J/m^2]	[eV]	
Pd	(210)	1.759	1.610	4.92	11-layer slab
	(210)	1.763	1.613		21-layer slab
	Avg.		2.00	5.1	Exp. [107, 108]

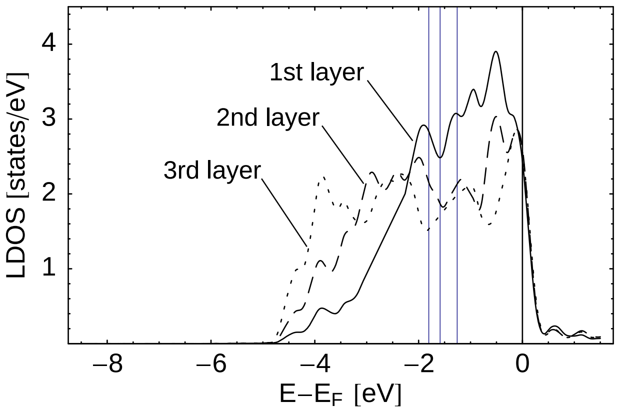

Figure 3.3: Layer-resolved, local *d*-band density of states of Pd(210). Indicated by vertical lines are the Fermi level and the center of the *d*-band. The third-layer LDOS is already very close to the bulk density of states of palladium.

d-band of the first layer atom to the very bulk-like density of states of the third layer atom can be seen (cf. Fig. A.5, [109]). This clearly shows that an 11 layer slab is a good enough model for the following relaxation and adsorption calculations.

As the (210) surface is a rather open surface, the interlayer distances should change considerably compared to their bulk values. On the other hand, as illustrated in Fig. 3.4, the bulk interlayer distance is only 0.88 Å so that small absolute relaxations already represent large relative changes. To determine the layer relaxations, an asymmetric 11 layer slab was set up with the lower six slab layers fixed to their bulk truncated positions using the theoretical bulk lattice constant. The top five layers were allowed to relax until the absolute value of the forces on each atom was smaller than 0.02 eV/Å.

The optimized interlayer distances are given in Table 3.2. The DFT results suggest that there is indeed a very pronounced layer contraction of the first layer (−17%) compensated by an outward relaxation of the third layer (+10%). Lateral displacements along the [$1\bar{2}0$] direction have been found to be very small: Only the first and third layer atoms exhibit a somewhat significant displacement by 0.04 Å and 0.05 Å, respectively.

In Table 3.2, the calculated layer relaxations are compared to experimental LEED results for Pd(210) [110]. The relative experimental values with respect to the bulk (210) layer spacing differ significantly from the calculations. One has to note, however, that the absolute discrepancies between experiment and theory are still rather small ($<$ 0.1 Å). In fact, the experimental determined layer relaxations are surprisingly small for such an open surface. This becomes evident when the experimental Pd(210) results are compared to the interlayer relaxations measured for Pt(210) [111]. One would expect similar relaxations for Pd and Pt since they have the same number of valence electrons and an almost identical lattice constant. Still the measured Pd(210) results are considerably smaller than the Pt(210) results.

These experimental results for Pt(210) are in fact rather close to our calculated values for Pd(210). And indeed, Kolthoff et al. [110] speculated that residual hydrogen coverages during the LEED experiments which were estimated to be lower than a quar-

Table 3.2: Layer relaxations of the Pd(210) surface. The DFT-GGA relaxations were computed for the pure Pd(210) surface, Pd(210) with one monolayer of hydrogen adsorbed as well as Pd(210) with half a monolayer of subsurface hydrogen (in the octahedral position). The relative change to the bulk interlayer distance (in %) is given in parentheses. Positive numbers correspond to a surface expansion away from the bulk substrate. Labels are as defined in Fig. 3.4.

Interlayer	Theory			Experiment	
distance	Pd(210)	Pd(210)/H($\theta = 1$)	Pd(210)/H($\theta_s = \frac{1}{2}$)	Pd(210)[110]	Pt(210)[111]
d_{12} [Å]	0.730 (−17)	0.791 (−11)	0.816 (−8)	0.84 ± 0.04 (-3 ± 6)	(-23 ± 4)
d_{23} [Å]	0.854 (−3)	0.859 (−3)	0.856 (−3)	0.93 ± 0.04 ($+7 \pm 5$)	(-12 ± 5)
d_{34} [Å]	0.976 (+10)	0.966 (+9)	0.974 (+10)	0.90 ± 0.04 ($+3 \pm 5$)	($+4 \pm 7$)
d_{45} [Å]	0.847 (−4)	0.860 (−3)	0.866 (−2)	0.86 ± 0.04 (-1 ± 5)	(-3 ± 7)
d_{Bulk} [Å]	0.885	0.885	0.885	0.870	0.877

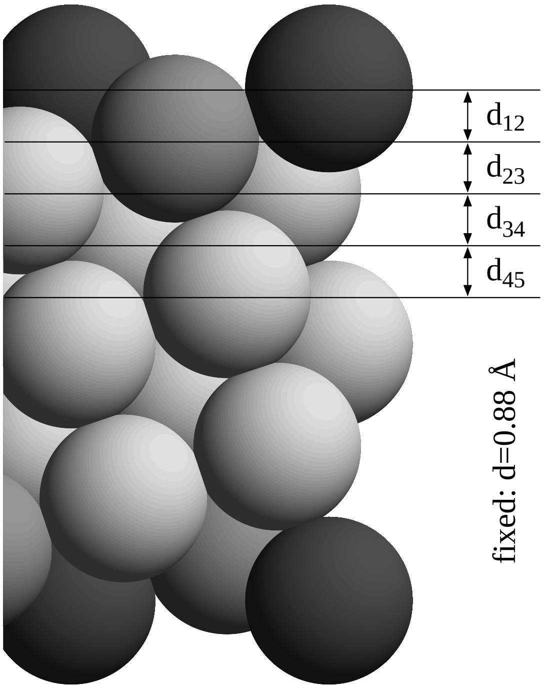

Figure 3.4: Definition of the interlayer distances of Pd(210). Due to the openness of the surface, the bulk interlayer distance is only 0.88 Å. The obtained values for the interlayer distances d_{ij} are given in Table 3.2.

ter monolayer might be responsible for the small Pd(210) relaxations measured in their experiment. We tested this suggestion by determining the relaxations for hydrogen-covered Pd(210). As Table 3.2 shows, one monolayer of adsorbed hydrogen atoms leads to a reduction in the interlayer relaxations, but not enough to reproduce the experimental results. Therefore we also checked whether subsurface hydrogen can account for the observed discrepancies. And indeed, already half a monolayer of hydrogen in the octahedral subsurface positions reduces the first layer contraction considerably (cf. Table 3.2), but the other layer relaxations remain almost unchanged. This is also true for a full monolayer of subsurface hydrogen that just expands the first to second layer distance further to almost its bulk truncated value. Overall, the effect of adsorbed or subsurface hydrogen resembles the findings on the (111), (100) and (110) surfaces of palladium [97]. Still we conclude from our calculations that subsurface hydrogen could be the cause for the small interlayer relaxations of Pd(210) observed in the experiment by Kolthoff et al. [110].

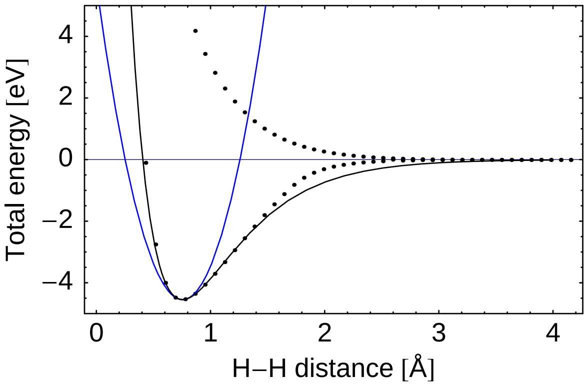

Figure 3.5: Potential curve of the H_2 molecule: The solid line represents a Morse potential fit to the attractive potential curve. For comparison, a harmonic fit to the data around the energy minimum is shown as a blue line.

3.2 Atomic hydrogen adsorption on Pd(210)

Hydrogen adsorption on palladium has been studied in great detail, both experimentally and theoretically. One of the reasons is that palladium can absorb hydrogen in sub-surface positions [112–114] and even in the bulk in huge amounts. Moreover, palladium is used as a catalyst for hydrogenation and dehydrogenation reactions. As far as the Pd(210) system is concerned, experimental thermo-desorption spectroscopy (TDS) data is available [13, 14, 101, 102], but direct microscopic knowledge of the adsorption sites is difficult to obtain. In the following, we will thus identify atomic adsorption sites and energies using DFT calculations and compare them to experimental data.

For a comparison of the adsorption energies of atomic hydrogen to experimentally accessible TDS data, it is essential to know the ground state properties of the H_2 molecule. As hydrogen adsorbs or desorbs on the metal surface from or to gas-phase H_2, it is essential to reference all DFT total energies to the ground-state energy of the H_2 molecule in the gas phase. The H_2 ground-state properties were extracted from a Morse potential fit as illustrated in Fig. 3.5. They are summarized and compared to the experimental data in Table 3.3. The DFT total energy (as employed in VASP) has been corrected for the error induced by treating the two isolated hydrogen atoms as having a spin-compensated charge density (ΔE = 1.10 eV, [116]) to get the total

Table 3.3: Binding energy, bond length, and stretching frequency for the H_2 molecule. Experimental data is taken from Herzberg and Huber [115].

	H_2			
	E_b [eV]	d [Å]	ω [cm^{-1}]	$\hbar\omega$ [eV]
GGA-USPP	4.55	0.75	4402	0.546
GGA-PAW	4.59	0.75	4331	0.537
Exp.	4.75	0.74	4401	0.546

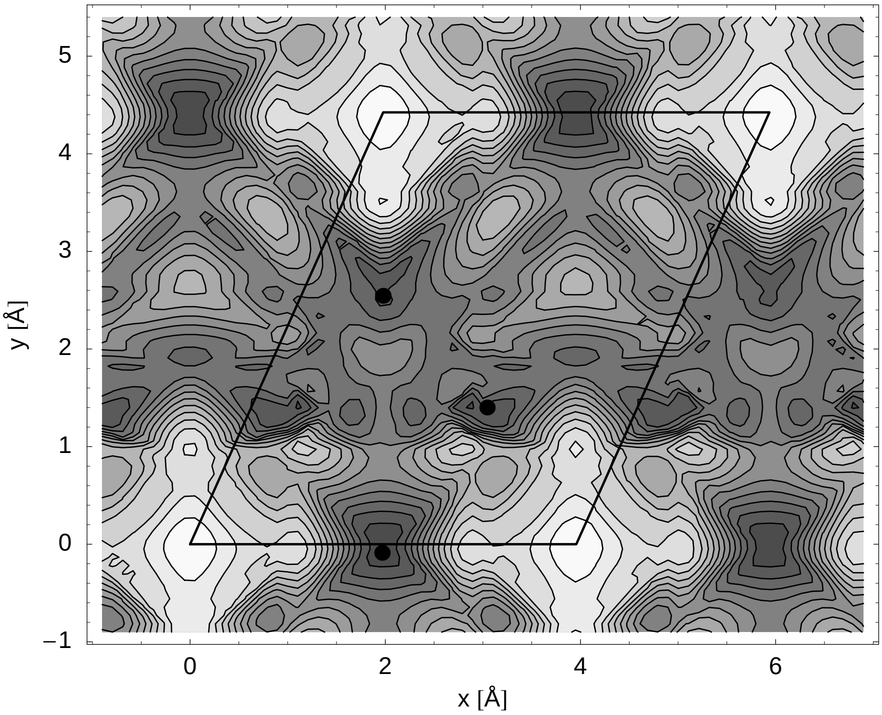

Figure 3.6: Potential energy surface of atomic hydrogen adsorption on Pd(210): $E(x_{\mathrm{H}}, y_{\mathrm{H}}) = \min_{z_{\mathrm{H}}} E_{\mathrm{total}}(x_{\mathrm{H}}, y_{\mathrm{H}}, z_{\mathrm{H}})$. Dark regions correspond to large adsorption energies, light regions to smaller adsorption energies. The three local minima with the lowest total energy are marked with black dots. The PES contour plot is interpolated using total energies at 32 grid points, and the surface unit cell is rotated by 180° around the [210] axis with respect to Fig. 3.1.

energy shown in Fig. 3.5. By doing so, the dissociation energy and the bonding length of the free H_2 molecule were determined to be 4.55 eV and 0.75 Å respectively It has to be noted that there exists a rather large error of 0.2 eV in the DFT binding energy of the hydrogen molecule, whereas bonding length and vibrational frequency are rather accurate. For this reason, we will report adsorption of atomic H with respect to both the numerical and experimental binding energy of H_2. Zero-point energies are neglected throughout this work.

In all adsorption calculations of Sections 3.2 to 3.5, the relaxed geometry as given in the first column of Table 3.2 was used in order to start from a fully self-consistent setup. Although the energy decrease due to the layer relaxations for the pure surface is just 0.06 eV, it was found that adsorbate-induced surface relaxations cannot be neglected in contrast to close-packed Pd surfaces [95]. Due to the openness of the surface, a full relaxation led to a decrease in total energy between 0.1 and 0.2 eV. All final adsorption energies are thus reported for a force-free, fully relaxed geometry.

Scanning the surface unit cell for possible adsorption sites by keeping the substrate fixed, but allowing the hydrogen atom at position $(x_{\mathrm{H}}, y_{\mathrm{H}}, z_{\mathrm{H}})$ to relax freely with respect to its z_{H} coordinate perpendicular to the surface results in the potential energy surface shown in Fig. 3.6. The calculations were done using a $p(1 \times 1)$ primitive unit cell corresponding to a coverage of $\theta = 1$. Due to the large size of the unit cell (3.96×4.42 Å), the interaction between hydrogen adsorbed in adjacent cells is negligible for such low coverages. The three energetically most favorable local minima are marked by black dots and correspond to the positions A, B, and C' of Fig. 3.1. Forced on-top adsorption at site D, $(x_\mathrm{H}, y_\mathrm{H}) = (0, 0)$, even yields a negative (endothermic) adsorption energy with respect to the H_2 gas phase ground state energy. The energetical ordering of the adsorption sites is found to be B < C' < A ≪ D. Clearly visible in Fig. 3.6 is also the rather large corrugation of the Pd(210) surface: The maximum difference of total energies, i.e., the total energies at sites B and D, amounts to 0.7 eV.

To verify the energetical ordering of the three most favorable adsorption sites, the DFT adsorption energies were computed with a fully relaxed slab where the hydrogen atoms were adsorbed asymmetrically on just one side of the slab and the bottom layers were again kept fixed. The final results are reported in Table 3.4, with respect to both the numerical and experimental binding energy of H_2. Relaxation of the substrate layers does not change the energetical ordering, although relative energy difference are slightly reduced due to the energy gained by the layer relaxation.

On close-packed palladium surfaces, hydrogen usually adsorbs at high coordination sites seeking as many bonding partners as possible. On the (210) surface, however, it is found that this intuitive assignment based on local coordination is not valid. Instead, the step site B is found to be the most attractive one. We note that site A, locally equivalent to a (100) hollow site, exhibits a very similar adsorption energy as reported for the (100) surfaces previously [95, 97]. Subsurface hydrogen either in the octahedral (O_d) or tetrahedral position (T_d) has been found to be exothermic by 0.21 eV and 0.15 eV respectively.

If a monolayer of hydrogen is already adsorbed at site B, the next most favorable

Table 3.4: Adsorption energies per atom for the different adsorption sites as a function of hydrogen coverage on Pd(210). The adsorption energies calculated with respect to the experimental binding energy of H_2 are given in parentheses. For $\theta > 1$, the atomic adsorption energies are defined as the energies for additional adsorption of one H atom per surface unit cell with respect to the H_2 molecule in the gas phase. The notation of the sites refers to Fig. 3.1.

		E_ad [eV]		
Coverage	Site	Theory	Exp.[13]	State
$\theta = 1$	B	0.52 (0.42)	0.41	β_3
	C'	0.51 (0.41)		
	A	0.45 (0.35)		
	O_d	0.21 (0.11)	0.19	α
	T_d	0.15 (0.05)		
$\theta = 2$	B,A	0.40 (0.30)	0.33	β_2
$\theta = 3$	B,A,C	0.26 (0.16)	0.23	β_1

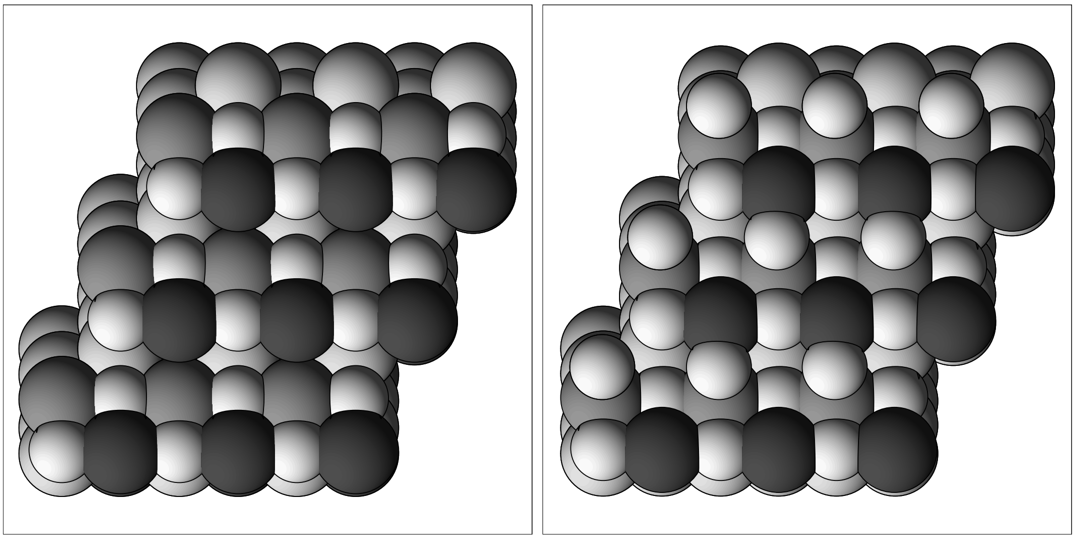

Figure 3.7: Hydrogen adsorption on Pd(210) for $\theta = 2$ and $\theta = 3$. For $\theta = 3$, the third hydrogen atom is repelled and forced to occupy the bridge site C.

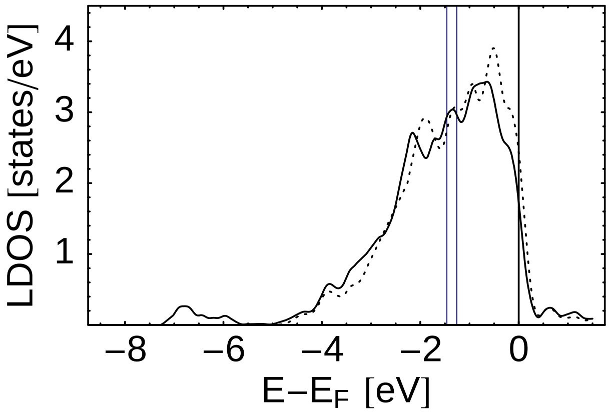

Figure 3.8: Induced change of the local density of states of the top Pd atom by adsorbing hydrogen at site B. The LDOS of the top Pd atom before (dashed) and after (solid line) adsorption are shown. Upon H adsorption, a resonance of the d-band with the H 1s state at $E - E_F \approx -6.5$ eV appears. The centers of the d-band, ε_d, are indicated by vertical lines. Due to the presence of H, the d-band center shifts from -1.26 eV to -1.45 eV.

adsorption site at a $\theta = 2$ coverage is site A with a slightly decreased adsorption energy of $E_{\text{ad}} = 0.40$ eV compared to the pure surface. At an even higher coverage of $\theta = 3$, repulsive forces between the hydrogen atoms become dominant and the distance between the preadsorbed hydrogen atoms at site B as well as site A and the third hydrogen atom is maximized so that the third hydrogen atoms actually moves away from site C' to the bridge site C with a significantly reduced adsorption energy of $E_{\text{ad}} = 0.26$ eV. Resulting adsorption geometries for $\theta \geq 2$ are shown in Fig. 3.7, and the results are summarized in Table 3.4.

The energetical ordering of the adsorption sites can be analyzed and understood in terms of their local reactivity. By projecting the Kohn-Sham wavefunctions to atomic orbitals (truncated to a sphere with the self-consistent Wigner-Seitz radius, $r_s = 1.55$ Å), the layer-resolved local density of states (LDOS) as shown in Fig. 3.3 can be obtained. As proposed by Hammer and Nørskov [80, 83, 85] and discussed in Sec. 2.2.5, the local reactivity can be related directly to the distance of the d-band center to the Fermi level.

For bulk Pd, the d-band center is located 1.86 eV below the Fermi level. Going from bulk to the surface, the d-band center moves gradually higher in energy towards the Fermi level, i.e., the d-band center of the third-layer atom is still close to the bulk value at $\varepsilon_d = -1.80$ eV whereas for the second-layer atom we obtain $\varepsilon_d = -1.56$ eV and for the top atom $\varepsilon_d = -1.26$ eV. According to the Hammer-Nørskov model, it is thus the top Pd atom that is by far the most reactive one. At all adsorption sites, hydrogen bonds to more than one palladium atom, however. To estimate the total chemisorption potential energies at the actual adsorption sites A, B and C', the geometrical average of the nearest neighbor d-band centers [87] can be used yielding $\bar{\varepsilon}_{d,B} = -1.47$ eV, $\bar{\varepsilon}_{d,C} = -1.54$ eV, and $\bar{\varepsilon}_{d,A} = -1.61$ eV, respectively. This indeed predicts the right ordering of the adsorption sites. The major origin of the variations in the bonding strength on Pd(210) can thus be attributed to the local variations of the electronic structure at the surface.

Recent experiments have identified three different hydrogen adsorption sites on Pd(210) using thermal desorption spectroscopy (TDS) [13, 14, 101]. A typical thermal desorption spectrum is shown in Fig. 3.9(a). The adsorption peaks attributed to atomic hydrogen are labeled β_1, β_2, and β_3. Derived desorption energies are listed in Table 3.4. Muschiol et al. [13] tentatively assigned the species with the highest adsorption energy (β_3) to the site with the highest coordination, i.e., the site labeled A in Fig. 3.1 with a four-fold coordination. The weaker bound H species (β_2 and β_1) were assigned to B and C' respectively (with C' being actually twofold-degenerate due to the mirror symmetry along $[1\bar{2}0]$). Given the results of our theoretical analysis, the microscopic assignment of the TDS states has to be changed: First, the energetical ordering of the adsorption sites is not fully determined by a simple coordination argument. Instead, the local reactivity of the involved atoms has to be considered, too. The assignment of the experimental TDS peaks in Table 3.4 has been done accordingly. Secondly, even though the (210) unit cell is rather large, repulsive effects between adsorbed hydrogen atoms become significant for $\theta = 3$ and the adsorption of a third hydrogen atom is only possible at the bridge site C.

3.3 Molecular hydrogen adsorption

H_2 usually adsorbs dissociatively at metal surfaces [88]. While at noble metals the dissociation is hindered by a sizable energy barrier, it occurs spontaneously on most transition metals, as, e.g., on palladium. Only at very low temperatures below 20 K, very weakly bound molecular adsorption states can be trapped in shallow physisorption wells [117, 118]. On the other hand, reports of molecular chemisorption of H_2 are rare and restricted to stepped surfaces: On Ni(510), a molecular adsorption state at surface

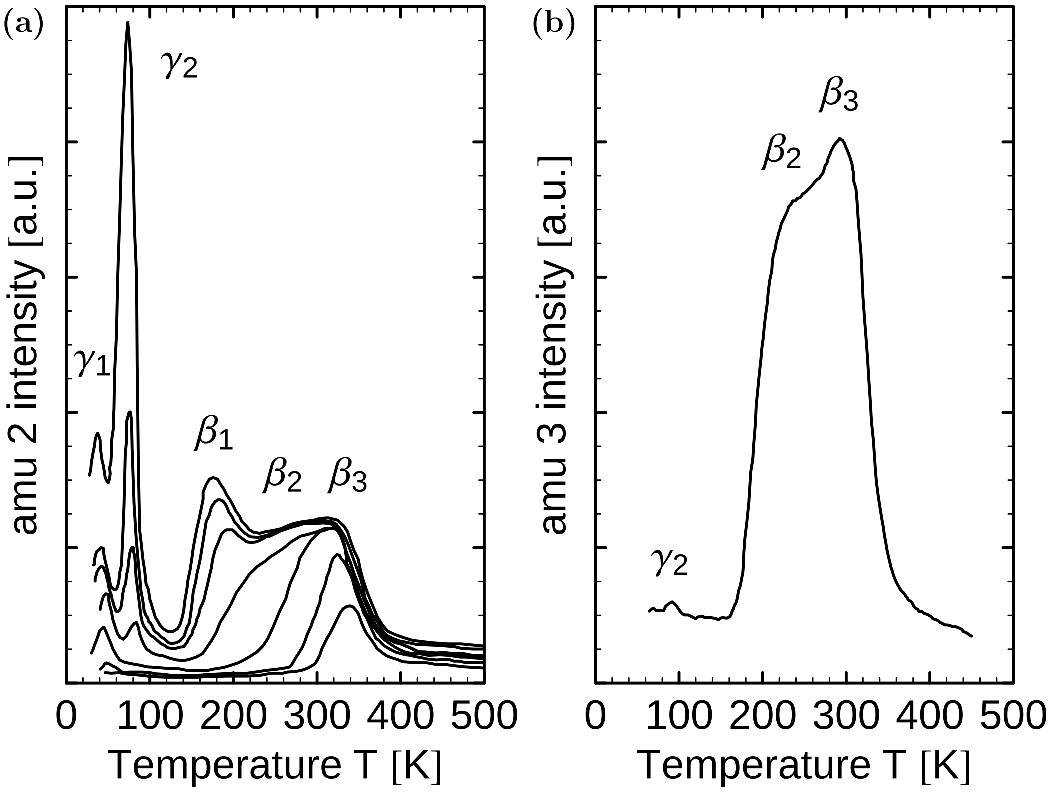

Figure 3.9: Thermal desorption spectra [14]. (a) Series of H_2 TPD spectra for different exposures between 0.02 L and 0.2 L at a temperature of 50 K. (b) Mass 3 (HD) TPD spectrum after a mixed H_2/D_2 exposure at 50 K.

temperatures up to 125 K has been observed at the step sites, but only after the surface was passivated with a dense atomic hydrogen layer [119]. On Cu(510), a weakly bound species has been observed at low temperatures on the pure surface [120, 121]. It is thus worthwhile to check whether molecular hydrogen adsorbs dissociatively on a Pd(210) surface or can be trapped in a molecular adsorption state: Results on close-packed surfaces such as H_2/Pd(100) [68, 95] suggest that hydrogen should dissociate spontaneously and without any activation barrier. Experimental results [14] for hydrogen adsorption at temperatures below 100 K, however, hint at the existence of two molecular adsorption states.

In Fig. 3.10(a)-(c), three two-dimensional sections ("elbow plots") of the potential energy surface (PES) for the H_2 adsorption on Pd(210) are shown. These sections were computed using a $p(1 \times 1)$ or a $p(2 \times 1)$ surface unit cell where necessary and plotted by cubic interpolation of the total energies and Hellman-Feynman forces at more than 56 calculated points scanning different bond lengths of H_2, d, and the height of the center of mass above the surface, z. The slab Pd atoms were kept fixed at the positions of the relaxed pure slab. Only for the determination of the final adsorption geometry and energy, a full relaxation including the top five slab layers was again performed. These two-dimensional cuts are characterized as, e.g., B-A indicating that the section

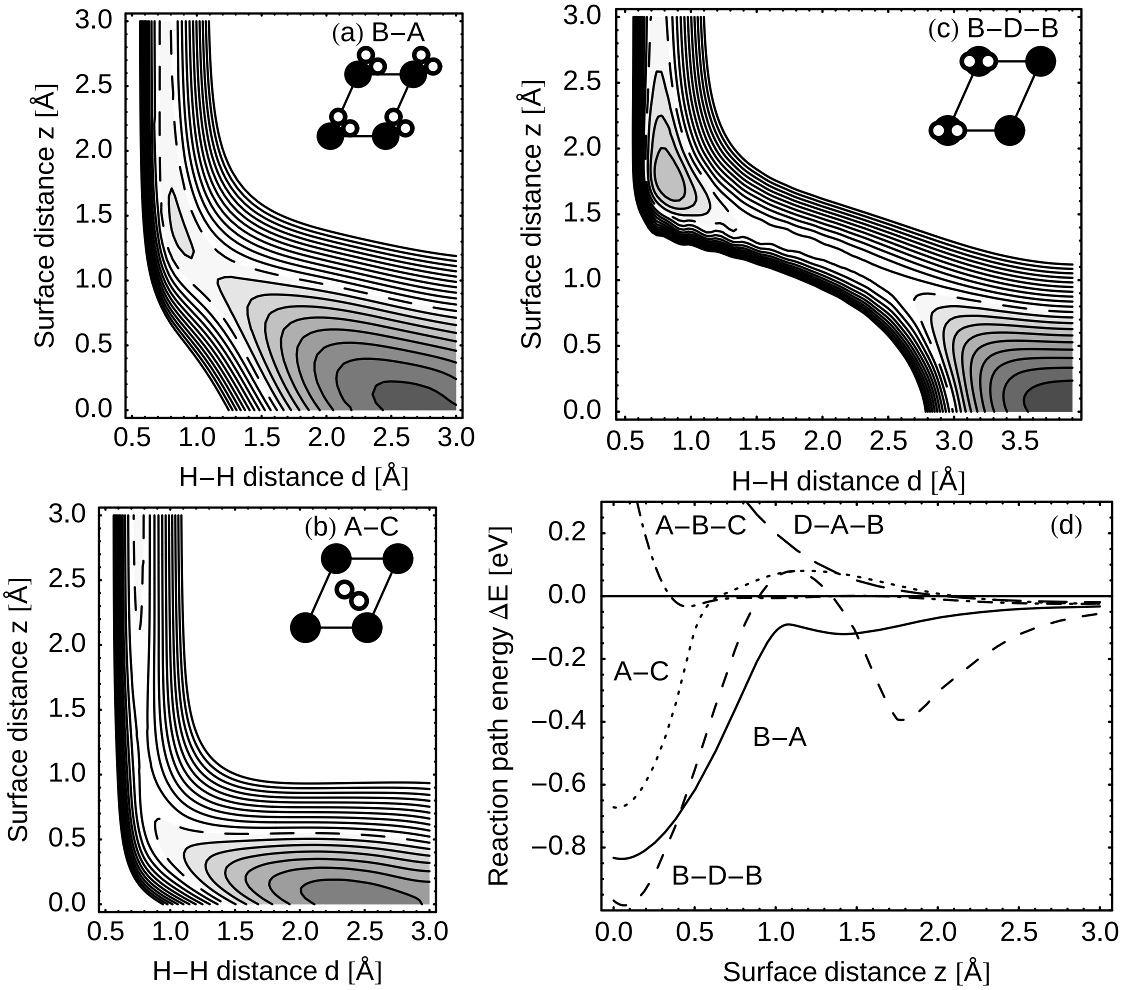

Figure 3.10: (a)-(c) Two-dimensional sections through the PES for the dissociative adsorption of H_2 on Pd(210). The coordinates in the figure are the H_2 center-of-mass distance from the surface z and the H-H interatomic distance d. The molecular orientation is indicated in the insets. The contour spacing is 0.1 eV, and the vacuum energy level is marked by the dashed contour line. (d) Potential energy along the reaction paths for H_2 on Pd(210). The orientation of the H_2 molecule is fixed to the one of the corresponding two-dimensional PES.

is given by the final atomic adsorption sites B and A (and the surface normal), or B-D-B indicating that the section is determined by two neighboring B sites with the molecule's center-of-mass fixed over the D site. The geometry of the hydrogen atoms is also shown by the insets in Fig. 3.10(a)-(c). The fixed orientation of the molecule is chosen according to the final adsorption geometry, i.e., for the B-A and A-C path the molecule is slightly tilted out of the plane parallel to the surface. The corresponding reaction path energies as a function of the surface distance z are depicted in Fig. 3.10(d). As can be seen clearly from Fig. 3.10(d), or the adiabatic reaction path shown and discussed later in Fig. 3.15, the H_2 molecule is first attracted towards the top Pd atom. Nevertheless, the DFT results suggest that at closer distances the H_2 molecule is able to dissociate spontaneously into the A and B sites as illustrated in Fig. 3.10(a). That the top site is most favorable at larger distances has also been found for other systems [68, 95, 122]. It is evident from Fig. 3.10 that no stable molecular adsorption state should exist at the clean Pd(210) surface due to the fact that hydrogen can always dissociate spontaneously. This exactly duplicates the scenario found in the system H_2/Pd(100) as can be seen by comparing the elbow plots to the ones of Fig. 2.3 [68].

This scenario is changed considerably by the presence of atomic hydrogen on the surface: In Fig. 3.11, the elbow plots and reaction path energies are shown for a surface pre-covered with a monolayer of hydrogen at site B. Dissociation along the B-A path is now obviously prohibited by the presence of atomic hydrogen at site B, but more important, the path to dissociation into the A and C sites is now blocked by a much more pronounced barrier of 220 meV. On the other hand, the attraction of the H_2 molecule to the top-layer Pd atom (site D in Fig. 3.1) is hardly influenced by the presence of the pre-adsorbed H atoms. The presence of hydrogen atoms thus leads to a metastable molecular adsorption state with a well depth of 270 meV. The adsorption well depth of Fig. 3.11(b) is almost invariant under rotation of the H_2 molecule around the surface normal. The final adsorption geometry of the fully-relaxed slab is illustrated in Fig. 3.12: The H_2 molecule, interspersed between the hydrogen atoms at the B sites, is bonded via the top Pd atom, sitting perpendicular to the step edge, and is slightly tilted out of the (210) plane.

That the top site's reactivity is hardly influenced by the pre-adsorbed hydrogen atom can be traced back to the induced change in the local density of states (cf. Figs. 3.8 and 3.13): Although there is a resonance of the d-band formed with the H $1s$ state at approximately -6.5 eV below the Fermi level, the center of the d-band just shifts from $\varepsilon_d = -1.26$ eV to $\varepsilon_d = -1.45$ eV. The top Pd atom is thus still more reactive than all other surface atoms.

It is important to note that this is not just a site-blocking effect due to the hydrogen atom at site B. If the hydrogen atom is placed at the octahedral subsurface position instead, the same stabilization effect can be observed. This is illustrated in Fig. 3.14 for the B-A reaction path. In this case, both B-A and A-C paths are activated and the local minimum in the B-D-B section of the PES (Figs. 3.10(c) and 3.11(b)) corresponds to a true metastable molecular adsorption state.

This stabilization can also be interpreted in terms of a bonding competition [123] between the pre-adsorbed hydrogen and the H_2 molecule: The adsorption is lowered due to the larger number of bonding partners, and the dissociation barrier is in turn

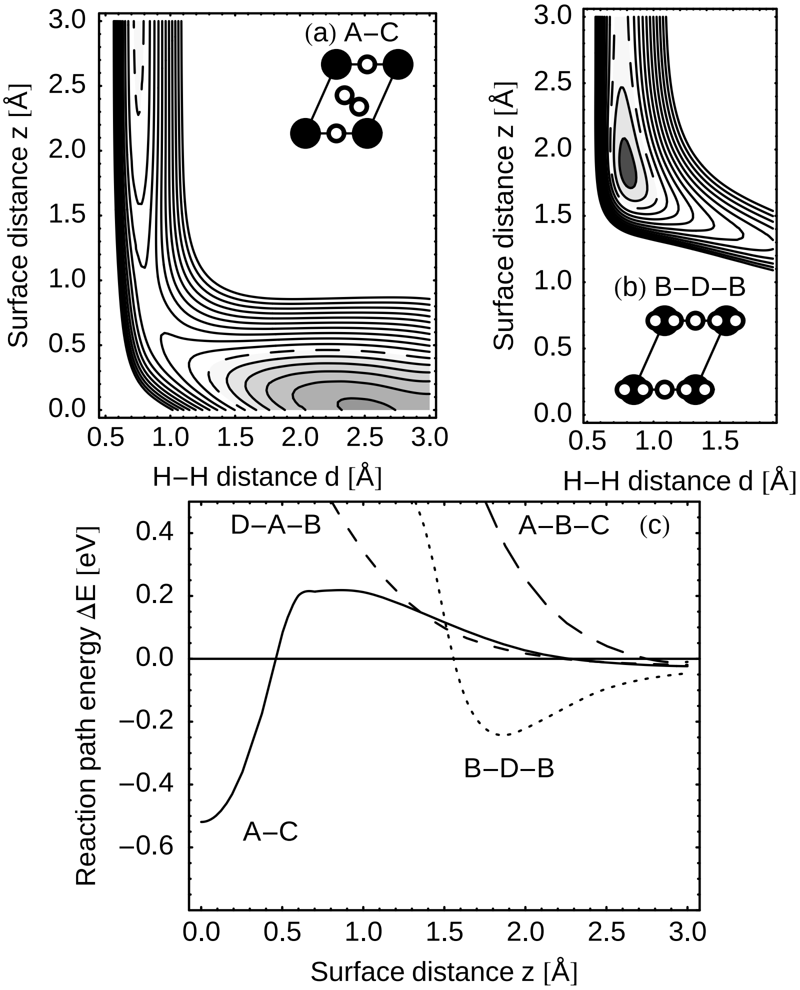

Figure 3.11: (a),(b) Two-dimensional sections through the PES for the dissociative adsorption of H_2 on Pd(210) pre-covered with a monolayer of hydrogen ($\theta = 1$). The coordinates in the figure are the H_2 center-of-mass distance from the surface z and the H-H interatomic distance d. The lateral H coordinates are indicated in the inset. The contour spacing is 0.1 eV, and the vacuum energy level is marked by the dashed contour line. (c) Potential energy along the reaction paths for H_2 on Pd(210) pre-covered with a monolayer of hydrogen ($\theta = 1$). Cf. Fig. 3.10.

increased, due to the strong correlation of transition state energies and adsorption energies [12, 124]. This relationship is also known as the Brønsted-Evans-Polanyi relation in heterogeneous catalysis [125].

To verify that the presence of atomic hydrogen indeed changes the dissociation channels from non-activated to activated, an “adiabatic” reaction path[95, 126] was computed: Starting from an arbitrary, but flat orientation far away from the surface over the most attractive site D, the H_2 molecule was fully relaxed within the four-dimensional subspace of a plane parallel to the surface, then pulled a little bit further towards the surface and relaxed again. By choosing different initial orientations we checked that the adiabatic reaction path does not depend on the initial conditions.

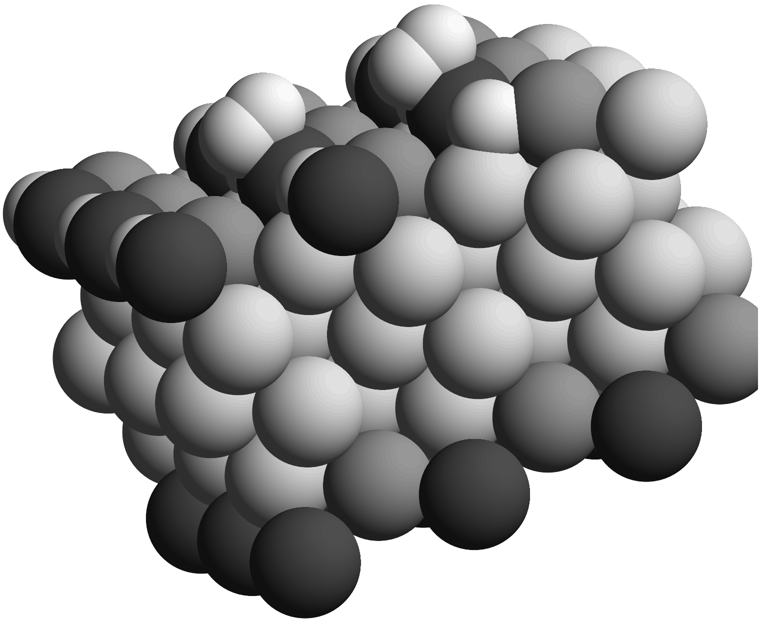

Figure 3.12: Side view of the Pd(210) surface with a monolayer of H precoverage and the fully relaxed molecular precursor.

This procedure mimics the discretized motion of a molecule with infinite mass and thus yields approximately the energetically most favorable reaction pathways. The reaction path energies for the pure (lower solid curve) and the H pre-covered surface (upper solid curve) are shown in Fig. 3.15. At large distances, the molecule is always steered towards the top Pd atom again, but then moves away to dissociate into the B and C' sites on the pure surface. On the pre-covered surface, the H_2 molecule ends up in a local minimum in two adjacent C' sites. The increase in the barrier height towards dissociation again demonstrates the stabilization of the molecular adsorption site above the top Pd atom. It has to be noted, however, that at close distances to the surface, $z < 1.0$ Å, canting forces on the molecule become noticeable. The shown adiabatic reaction path is thus only approximately correct, and for very small distances the true minimal reaction path might be even below the computed reaction path energies. This true minimal reaction path and the real transition state would be only accessible by a nudged elastic band method calculation [127] or one of its enhancements [128, 129].

This molecular adsorption well at site D prevails even at higher atomic hydrogen coverages of $\theta = 2$ and 3. The adsorption energies for the fully relaxed geometries are 220 and 90 meV respectively. Even for $\theta = 3$, the top Pd atom remains reactive enough to attract the H_2 molecule although it already binds to four hydrogen atoms on the surface (see Fig. 3.7). The adsorption energies for all three pre-coverages are summarized in Table 3.5.

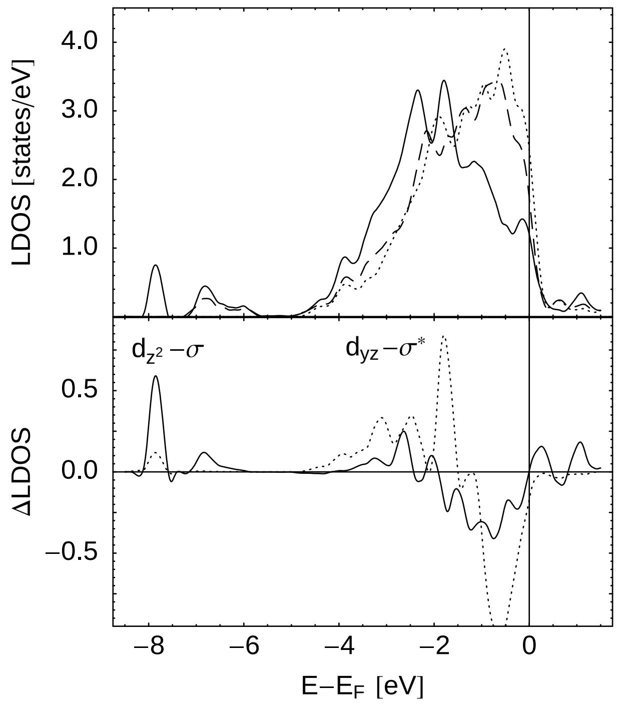

Figure 3.13: Top panel: Local density of states of the top-most Pd atom before atomic hydrogen adsorption (dotted), after atomic hydrogen adsorption (dashed) and after additional adsorption of H_2 (solid line). Lower panel: Differences in orbital-resolved LDOS induced by H_2 adsorption on H/Pd(210) of the d_{z^2} (solid line) and the d_{yz} orbitals (dotted line).

Table 3.5: Adsorption energies per molecule for the different adsorption configurations as a function of hydrogen coverage on Pd(210). It has to be emphasized that the adsorption energies, E_{ad}, correspond to the molecular adsorption at a single adsorption site, but with different pre-coverages of atomic H.

		E_{ad} [eV]		
Coverage	Site	Theory	Exp. [14]	State
$\theta = 1$	D	0.27	0.25	γ_2
$\theta = 2$	D	0.22	0.16	γ_1
$\theta = 3$	D	0.09	–	δ

In TDS experiments for hydrogen adsorption at temperatures below 100 K, two additional adsorption states were identified [14, 102]. These states were attributed to two molecular H_2 species as no mixing was found in H/D isotope exchange experiments as shown in Fig. 3.9(b). Based on the DFT results, we thus suggest that the two molecular adsorption species found in the TDS experiments correspond to the molecular wells for two different local pre-coverages, $\theta = 1$ and $\theta = 2$. Therefore, the two observed species do not populate different molecular adsorption sites, but just correspond to two different underlying atomic hydrogen coverages. Our findings are summarized in Table 3.5, and the assignment is further substantiated by the facts described in the

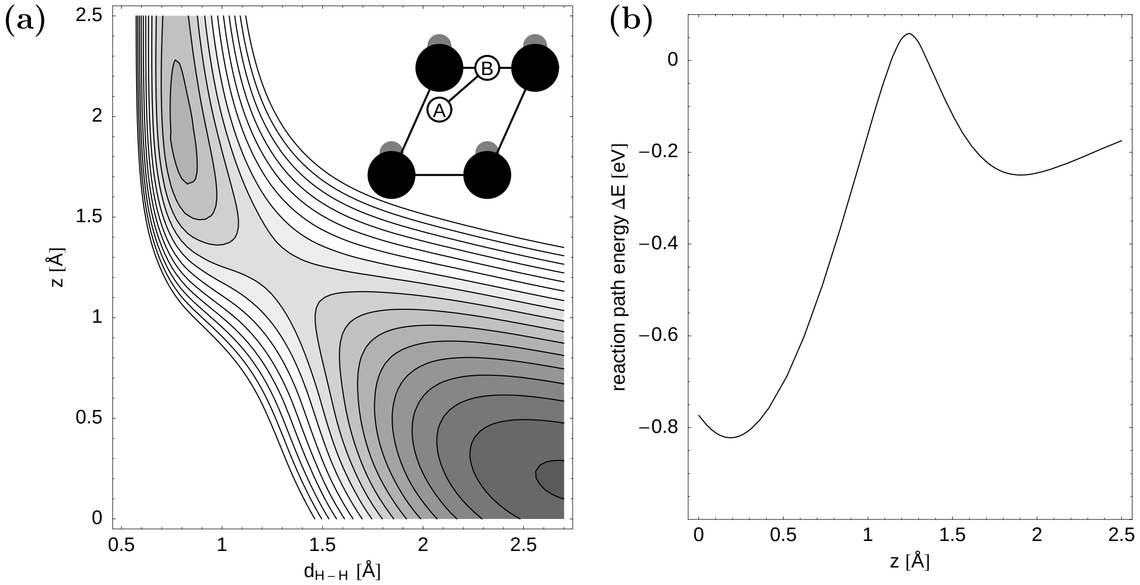

Figure 3.14: (a) Two-dimensional section through the PES for the dissociative adsorption of H_2 on Pd(210) with hydrogen absorbed in the octahedral sub-surface position ($\theta = 1$). (b) Potential energy along the corresponding reaction path. Cf. Fig. 3.10.

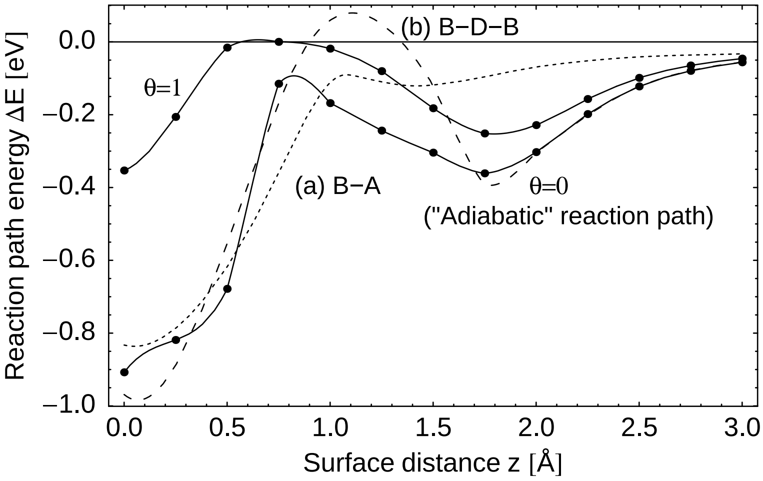

Figure 3.15: Adiabatic reaction path energies for H_2 on the pure (lower solid curve) and the H pre-covered surface (upper solid curve). For comparison, the B-A (dotted) and B-D-B (dashed) reaction path energies are also shown.

following.

That the given interpretation is correct is further confirmed by monitoring the work function change upon hydrogen adsorption: It was found in the experiment [13, 14] that one monolayer of atomic hydrogen increases the work function by 120 meV whereas the work function decreases by 375 meV relative to the pure surface upon molecular hydrogen adsorption. To compute the work function change within the

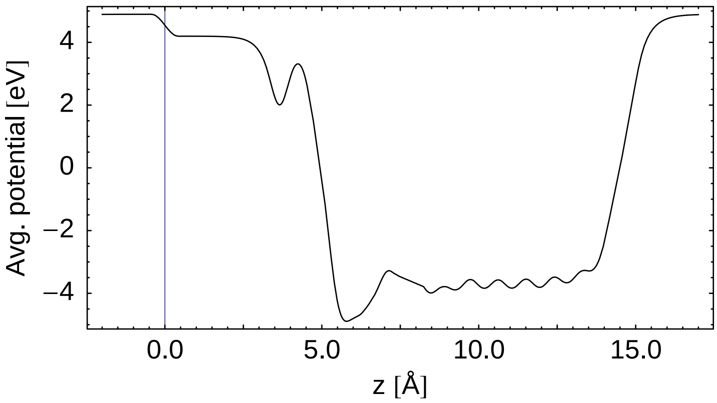

Figure 3.16: Average electrostatic potential of H_2/H/Pd(210): The correcting dipole layer is located at $z = 0.0$ Å, the center-of-mass of the H_2 molecule is at $z = 3.66$ Å. The total difference between the left and right vacuum level is 0.7 eV.

periodic plane-wave setup, an artificial dipole layer was introduced in the vacuum region as described in Sec. 2.2.3. The resulting electrostatic potential of the H_2/H/Pd(210) slab system is shown in Fig. 3.16. The difference in the vacuum levels, $V(z \to 0^-) - V(z \to 0^+)$, exactly represents the induced work function change. As shown, molecular hydrogen leads to a decrease of approximately 0.7 meV. This decrease was found to be almost independent of the hydrogen pre-coverage ($\theta = 0, 1, 2$). For just a monolayer of atomic hydrogen with no molecular H_2 present, we find an increase of approximately 0.2 eV. Although the DFT-computed work function changes are somewhat larger than the experimentally observed work function changes, the qualitative behavior is clearly reproduced.

The pronounced effect of the adsorbed molecule on the work function can also be inferred from the charge rearrangement as shown in Fig. 3.17. The strong hybridization between the H_2 molecule sitting 1.7 Å above the surface and the top Pd atom is visible in the electron density contour plot of Fig. 3.17a and more clearly in the electron density difference plot of Fig. 3.17b. The electron density difference is computed as the difference of the electron densities of the interacting system and the isolated H_2 molecule as well as the H-covered Pd(210) surface. It is evident that the H_2 molecule becomes strongly polarized upon adsorption and thus causes a decrease of the work function.

Furthermore, the proposed scenario is corroborated by the experimentally observed vibrational frequency of the adsorbed H_2 molecule, $\hbar\omega_{vib} = 420$ meV. The theoretical vibrational frequency of the molecule at site D is computed to be 422 meV in the harmonic approximation (free H_2: 546 meV, cf. Table 3.3). The H-H molecular bond is thus slightly weakened indicating a population of the anti-bonding σ^* orbital. This picture is confirmed by analyzing the induced change of the local density of states as shown in Fig. 3.13. In the upper panel, the local density of states before (dashed) and after H_2 adsorption (solid) is depicted. A pronounced resonance peak at -8 eV is clearly visible. This resonance peak can be traced back to the interaction of the H_2 σ orbital with the Pd d_{z^2} band as illustrated by the induced change in the d_{z^2}-

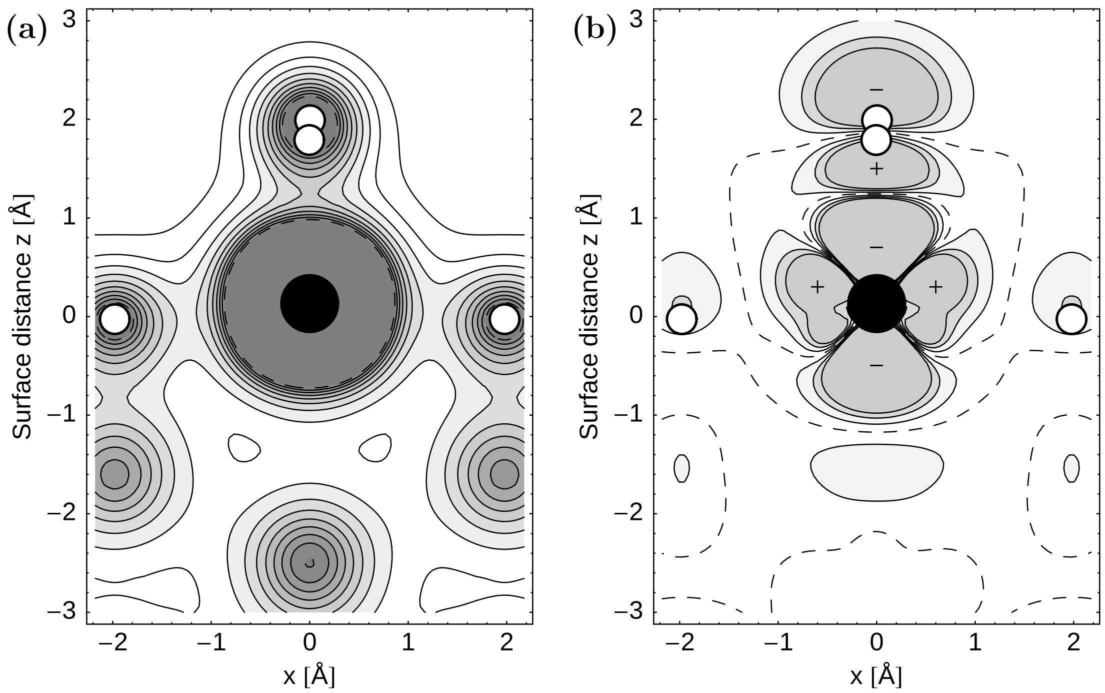

Figure 3.17: (a) Electron density contour plot of the molecular adsorption state in the $x - z$ plane ($x \parallel [001]$). The positions of the H atoms and the top Pd atom are marked by open and filled circles respectively. The top Pd atom and the H atoms at site B are exactly located within the plane, whereas the H atoms of the molecule are actually residing above and below the drawn plan. (b) Corresponding electron density difference plot. Regions of reduced electron density (i.e., positively charged) compared to the isolated systems H_2 and H/Pd(210) are marked with a minus sign, regions of enhanced electron density with a plus sign.

resolved LDOS (solid curve in the lower panel). Furthermore, the H_2 σ^* orbital shows a resonance peak with the d_{yz} band at -2 eV below the Fermi level and thus gets populated. Due to the symmetry of the minimum energy configuration, there is no interaction with the d_{xz} band. The following interaction picture can thus be derived: When approaching over the top site, the H_2 molecule interacts with the d_{z^2}, d_{yz} and d_{xz} orbitals of the top Pd atoms. By symmetry arguments, the H_2 σ orbital can only interact with the d_{z^2} orbital leading to a very small charge loss in the d_{z^2} band. On the other hand, the interaction of the antisymmetric H_2 σ^* orbital with the d_{yz} (d_{xz}) orbital gives rise to a filled $d_{yz} - \sigma^*$ resonance level yielding a net energy gain. Overall, the H-H bond is weakened and the H-Pd bond strengthened. A very similar scenario was also found for H_2 on Ni [122].

Based on these facts, the following scenario for H_2 adsorption on Pd(210) is thus proposed: On clean Pd(210), hydrogen adsorbs dissociatively. Once atomic hydrogen is present on the Pd(210) surface, further hydrogen dissociation becomes kinetically hindered close to the adsorbed hydrogen atoms although atomic adsorption sites are still available. This can be regarded as a local self-poisoning of hydrogen dissociation. In contrast to experimental results for H_2 adsorption on Ni(510) [119], where all adsorption sites for dissociative adsorption are occupied, or H_2 on Cu(510) [120, 121], where step sites are occupied by the H_2 molecules on the pure surface, this local self-poisoning is essential to stabilize the molecular adsorption state on Pd(210) according to our DFT results. Nevertheless, this molecular adsorption state shows similar characteristics as the H_2/Cu(510) system discussed by Bengtsson et al. [121] with respect to the azimuthal anisotropy of the molecular state. Even with H pre-adsorbed at site B ($\theta = 1$) and at a full monolayer coverage of H_2, i.e., with every top site populated, the H_2 molecule is still able to rotate almost freely around its azimuthal angle. The maximum variation of the potential energy for an azimuthal rotation of the molecule by $\pi/2$ is just 4 meV. It should thus exhibit the same two-dimensional rotor states as found for the system H_2/Cu(510).

It is interesting to analyze why the Pd(210) surface has such unique features with respect to hydrogen adsorption. Since the steps at the (210) surface represent (110)-like microfacets, a Pd(110) surface might show similar properties. The site B at the Pd(210) surface (see Fig. 3.1) corresponds to the so-called long-bridge position at the (110) surface. However, on the Pd(110) surface the most favorable site for atomic adsorption of hydrogen is the pseudo threefold site on the micro (111)-like facets [97] and not the long-bridge site. Furthermore, the top layer atoms are not protruding as much as on the Pd(210) surface which also modifies the local reactivity. Consequently, it seems to be the combination of specific structural elements that enables the coexistence of atomic and molecular adsorption states on Pd(210) although the surface is not fully passivated.

3.4 CO adsorption

In the previous sections, we have discussed the adsorption process for a diatomic molecule, H_2, and the corresponding potential energy surfaces on Pd(210). It was found that the Pd(210) surface exhibits rather unique features due to its specific structure.

Another “prototype” system for the study of adsorption on metal surfaces is the adsorption of carbon monoxide, CO. Technologically, CO is known as a rather unwanted catalytic poison - it binds rather strongly ($\approx 1 - 2$ eV) to the surface and is able to passivate an otherwise reactive surface. On the other hand, compared to the CO dissociation energy of 11.23 eV, the binding to the surface is rather weak. This leads to the plausible assumption that the electronic structure of the free CO molecule is only slightly modified upon adsorption. The simple interaction picture proposed by Blyholder [130] is capable of explaining the CO adsorption qualitatively [130–132]: Charge donation from the 5σ orbital to the metal and back donation to the 2π orbital establishes a metal-CO bond, but at the same time weakens the carbon-oxygen bond. Variations in the stretching frequencies of CO can thus be explained.

Molecular CO is known for its ability to populate different adsorption sites with a very local binding, and quite a few theoretical and experimental studies on CO adsorption on different palladium surfaces exist [131, 133–144]. On Pd(100), CO is known to adsorb upright in bridge positions at every coverage [134, 137]. As the

Pd(210) can be thought of as being built up of small (100) terraces, it is thus interesting to analyze CO adsorption on this stepped surface.

The properties for the CO molecule as obtained by *ab initio* DFT calculations are summarized in Table 3.6 and compared to their experimental values. All molecular properties were computed using a large, asymmetric supercell of dimensions $10.00 \times 10.25 \times 10.50$ Å. In the case of H_2 (Table 3.3), the asymmetricity of the supercell and thus the breaking of any inherent symmetry in the atom or molecule is not important, but for molecules involving atoms with degenerate orbitals such as oxygen, the effect of the supercell symmetry on the computed binding energy can become quite significant [145]. For an accurate representation of the oxygen core region, PAW pseudopotentials [57, 58] together with an energy cutoff of 400 eV were used. All other theoretical parameters were chosen identical to the ones described in Sec. 3.1, including the use of the PW91 generalized gradient approximation.

No evidence for any reconstruction upon CO adsorption exists experimentally [134], so that the relaxed (210) layer geometry as given in Table 3.2 was used. As CO induced layer relaxations might be quite substantial, adsorption energies for both a slab fixed at the positions of the clean (210) surface and a fully relaxed slab are reported.

Possible CO adsorption sites are shown in Fig. 3.18. As CO is known to occupy bridge sites on Pd(100) or near-bridge sites on Pd(110), it is expected that sites C and E are going to be preferred adsorption sites: Site E corresponds to a bridge position on the (100) terrace, site C to a bridge position on a (110) facet. The DFT results are summarized in Table 3.7. The obtained adsorption energies confirm this assumption: The bridge site E is the most favorable adsorption with an adsorption energy of 1.88 eV. Relative energetical ordering does not change upon a full relaxation of the substrate layer. The energy difference between an adsorption at sites E and C, however, is almost diminished.

Adsorption at site E might be interpreted as an adsorption on a (100) terrace with an angle of 26.6° against the (210) surface, adsorption at site C as an adsorption on a (110) facet with an angle of 18.4° against the surface. Both sites are however identical as far as the direct bonding partners of the CO molecule are concerned, only next-nearest neighbors are different. Relaxed adsorption geometries for both sites are detailed in Table 3.8, and the computed atom distances at both sites are identical within our numerical accuracy. Furthermore, the CO molecule is bonding almost perpendicular on the line connecting its two respective palladium partners. We thus only note one Pd-C distance in Table 3.8 as differences are below 0.005 Å. However, the induced

Table 3.6: Binding energy, bond length, and stretching frequency for the CO molecule. Experimental data is taken from Herzberg and Huber [115].

	CO		
	E_b [eV]	d [Å]	ω [cm^{-1}]
GGA-PAW	11.78	1.14	2135
Exp.	11.24	1.13	2170

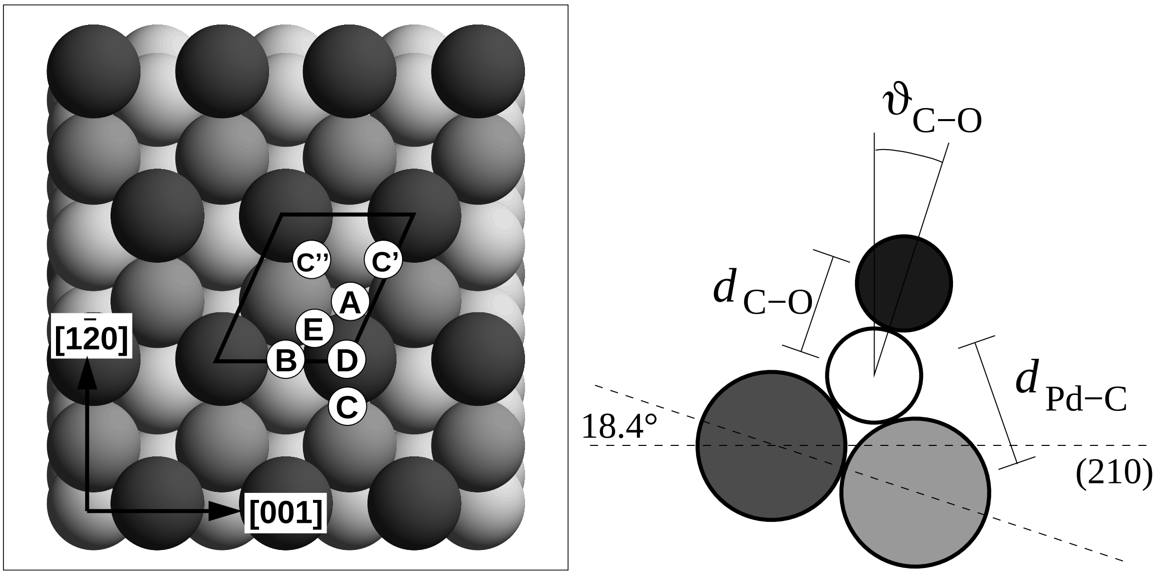

Figure 3.18: Possible CO adsorption sites and bonding parameters on Pd(210): O is drawn in black, C in white. The Pd atoms are shaded in gray, and the color coding is identical to the one used in Figs. 3.19 and 3.20. The site notation is the same as used for hydrogen adsorption (cf. Fig. 3.1).

layer relaxations at site C are much stronger than at site E, allowing the molecule to position itself in a more upright fashion while still perfectly preserving its bridge-bonding position. This also explains the relatively large energy gain at this position when relaxing the substrate.

Experimentally, electron stimulated desorption ion angular distribution (ESDIAD) measurements [135] at low coverages up to $\theta = 1$ suggest adsorption of CO in a bridge-bonded position at site E, inclined away from the surface normal, in agreement with our DFT results. Thermal desorption results yield an initial adsorption energy of 1.52 eV

Table 3.7: Adsorption energies per molecule for different adsorption sites of CO on Pd(210). The notation of the sites refers to Fig. 3.18. For adsorption at the on-top site, the molecule was laterally constrained to position D.

		E_{ad} [eV]			
Coverage	Site	Fixed slab	Relaxed slab	Exp.[102]	State
$\theta = 1$	E	1.83	1.88	1.45	β_2
	C	1.76	1.86		
	B	1.73	1.77		
	A	1.50	1.58		
	D	1.48	1.50		
$\theta = 1.5$		0.91	—	1.14	β_1

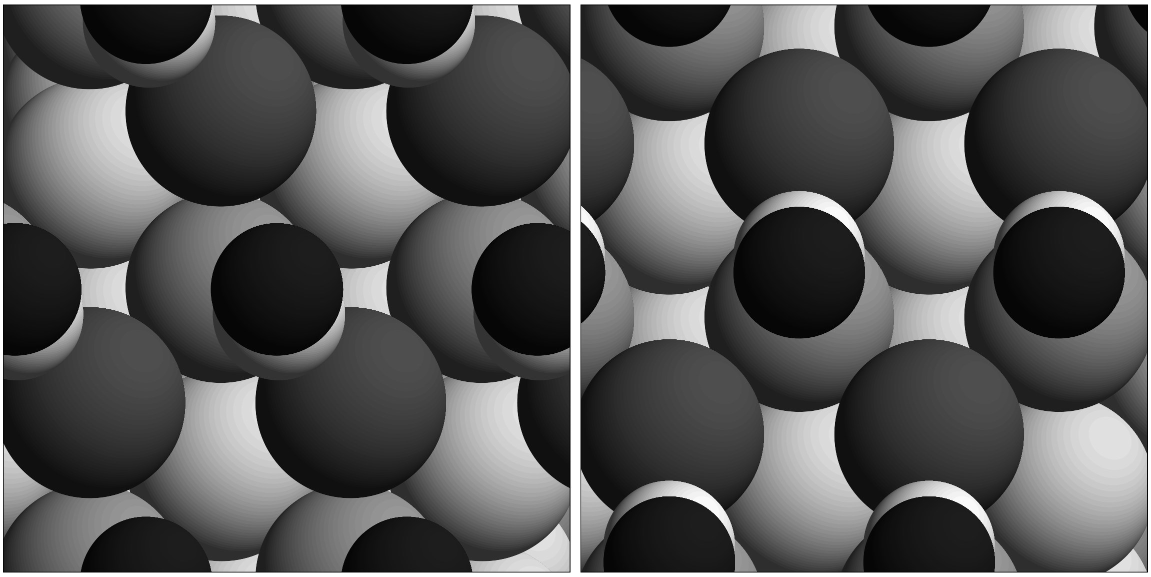

Figure 3.19: Adsorption geometries for CO on Pd(210): The left panel illustrates the final adsorption geometry of CO at site E, the right panel at site C. In both cases, the bridge-bonded, inclined CO geometry is clearly visible.

[133] or 1.45 eV per molecule [102]. The binding energy for the bridge site E is thus considerably overestimated. GGA calculations using the PW91 exchange-correlation functional, however, tend to overestimate the CO adsorption on a wide range of metal surfaces [146].

For the CO adsorption on Pd(100), DFT computations give an adsorption energy of 1.97 eV for the $c(2\sqrt{2} \times \sqrt{2})$ CO superstructure [137], being rather similar to our results. Nevertheless, it is surprising that the adsorption energy of CO in fact turns out be slightly lower on Pd(210) than on Pd(100). Given the low coordination of the top Pd atom and thus its high reactivity, it might be anticipated that CO is actually strongly bound to Pd(210). For on-top adsorption, this is indeed true: Adsorption at site D gives a binding energy of 1.50 eV, whereas on-top adsorption on Pd(100) gives 1.44 eV [137]. As in both cases the nearest-neighbor distance of the CO molecules is identical, i.e., the Pd lattice constant, a_0, any dipole-dipole repulsion effects should be comparable and thus not change any relative differences. Besides, dipole-dipole interactions at a similar coverage on Pd(110) were estimated to be on the order of

Table 3.8: Adsorption geometries for CO on Pd(210) at a coverage of $\theta = 1$. The used notation for the bonding lengths and angle is illustrated in the right panel of Fig. 3.18.

Site	$d_{\mathrm{Pd-C}}$ [Å]	$d_{\mathrm{C-O}}$ [Å]	$\vartheta_{\mathrm{C-O}}$ [°]	d_{12} [Å]	d_{23} [Å]
E	1.99	1.18	18.0	0.760 (−14)	0.950 (+7)
C	1.99	1.18	12.0	0.723 (−18)	1.023 (+15)

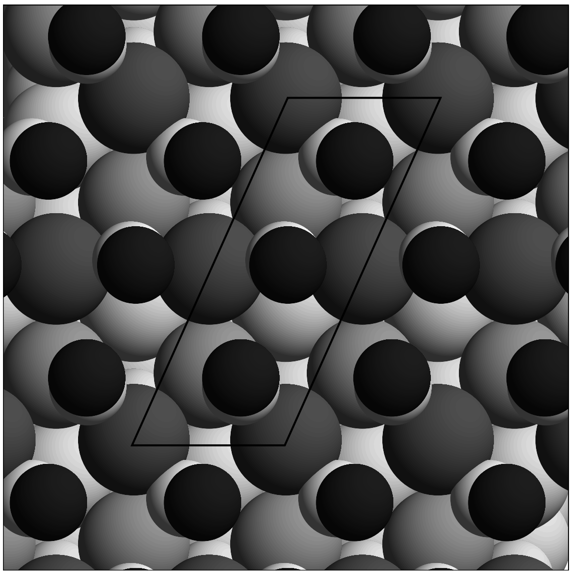

Figure 3.20: Adsorption geometry of CO/Pd(210) at a coverage of $\theta = 1.5$. The CO molecules are (approximately) located at sites E, B, and C' (from bottom to top). The (1×2) surface unit cell is also shown.

30 meV [142]. Experimental TDS results, too, suggest a slightly higher adsorption energy on Pd(100) than on Pd(210) [133]. As seen in Table 3.8, adsorption in both bridge-bonded sites results in rather strong relaxations, and a tendency to minimize the CO inclination is always found. This suggests that the CO molecule is just repelled by the protruding Pd atom at the next "step", and adsorption is thus not as favorable as on a flat (100) surface. Furthermore, variations in the CO adsorption energy from site to site are comparably small and a rather small energy gain due to a more reactive bonding partner might just be overcompensated by the enforced, but unfavorable inclination of the molecule.

On Pd(110), CO adsorbs in a near-bridge site at monolayer coverage. The molecules are alternately tilted along the [100] direction (perpendicular to the top layer rows), resulting in a (2×1) periodicity [140] forming a "zig-zag" chain of CO molecules. In contrast to the situation on the (210) surface, each Pd atom binds two alternately titled CO molecules. Computations in a (1×2) unit cell of the (210) surface revealed no evidence for such an alternating structure on the (210) surface.

Experimental saturation coverage of CO on Pd(210) is reported to be $\theta = 1.5$ [133]. LEED experiments show that this coverage is achieved by maintaining rows of CO molecules along the [001] direction, but reducing the CO distances along the $[1\bar{2}0]$ direction. A possible microscopic structure is shown in Fig. 3.20. The energy gain of additional adsorption of one CO molecule per (1×2) unit cell going from $\theta = 1.0$ to $\theta = 1.5$ is 0.91 eV. In comparison, TDS results yield a weaker bound β_1 species with an adsorption energy of 1.14 eV [102]. The CO molecules rearrange in such a way that one of them stays in the most favorable E site, whereas the other two rows of CO molecules are pushed to approximately the B and C' sites. However, no comprehensive

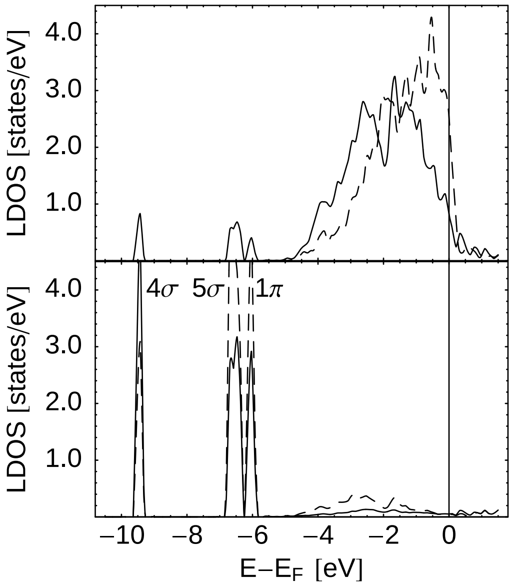

Figure 3.21: LDOS analysis of CO adsorbed at the bridge site E on Pd(210). Upper panel: Local d-band density of states of the top-most Pd atom before (dashed) and after (solid) CO adsorption. The d-band center is shifted from −1.26 eV to −1.82 eV upon CO adsorption. Lower panel: Local DOS (summed over all orbitals) at the carbon (solid) and oxygen atom (dashed) with a projection radius of $r = 1.058$ Å (2 bohr). The resonant levels are labeled according to the orbitals they originate from in the free gas-phase CO molecule.

scan of possible structures in the (1×2) unit cell was performed so that the existence of other structures lower in energy cannot be ruled out.

Corresponding to the large intrinsic dipole moment of the CO molecule, a CO coverage of $\theta = 1.5$ results in a significant work function increase of $\Delta\Phi = 1.45$ eV ($\Phi = 6.37$ eV). At a coverage of $\theta = 1.0$, a still considerable increase of 1.26 eV is found ($\Phi = 6.18$ eV). In CO adsorption experiments on Pd(210), a maximum increase of the work function by 1.06 eV is reported [133]. As for hydrogen-induced work function changes, the computed effect of the adsorbate on the work function is thus overestimated.

CO bonding to a metal surface is usually discussed in terms of the Blyholder model [130]. A more thorough discussion can be based on the analysis of the resulting mixed orbitals as they are manifested in the respective local density of states [147, 148]. In Fig. 3.21, the local density of states for both the top Pd atom and the carbon and oxygen atoms are depicted. The CO 1π, $2\pi^*$ and the Pd d orbitals with π symmetry hybridize to give an all-bonding $1\tilde{\pi}$, a non-bonding $\tilde{d}_\pi$, and an anti-bonding $2\tilde{\pi}^*$ orbital [147]. On the other hand, the CO 4σ, 5σ and the Pd d_σ interact to form bonding $4\tilde{\sigma}$ and $5\tilde{\sigma}$ orbitals as well as a broad anti-bonding $\tilde{d}_\sigma$ band. In Fig. 3.21, the broad resonance of the CO orbitals with the respective metal d-band orbitals in the energy range of −5 to 0 eV are clearly visible. The much lower density of states in this region at the carbon atom can be traced back to the non-bonding character of the $\tilde{d}_\pi$ orbital, with its reduced charge density at the carbon atom due to its nodal plane there. As expected, the distance between the modified 4σ ($E = -9.5$ eV) and 5σ

orbitals ($E = -6.5$ eV) is significantly reduced, and the 5σ orbital is even located below the 1π orbital ($E = -6.0$ eV) in contrast to the free CO molecule. The derived bonding scenario is very similar to the one found for bridge site adsorption of CO on Pd(100) [137].

This interaction picture is also capable of accounting for the fact that CO always adsorbs with the carbon atom towards the surface [147]. On Pd(210), DFT calculations with the oxygen pointing towards the surface gives a roughly non-bonding scenario yielding no net energy gain in contrast to the large adsorption energy of 1.88 eV for carbon-terminated bonding. In the described final electronic structure after the metal *d*-band interaction is taken into account, both the interactions of the σ and the π orbitals result in a net charge transfer to the atom not bonding to the surface. As the oxygen atom is more electronegative, adsorption with the carbon atom towards the surface yields a much larger adsorption energy.

3.5 Coadsorption of H and CO

As we have seen, adsorption energies for CO on Pd(210) are rather large, especially compared to the hydrogen adsorption energies reported in Secs. 3.2 and 3.3. It is thus expected that any coadsorption of carbon monoxide and hydrogen will be dominated by the CO molecule. Nevertheless, due to the rather open structure of the (210) surface, atomic or even molecular hydrogen adsorption might still be possible. On a specially prepared Ni(100) surface covered with hydrogen and carbon monoxide, for instance, a structural transformation upon heating and the formation of chemisorbed H_2 is found [149].

We have discussed in the previous section that, both experimentally and theoretically, adsorption at the bridge site E is energetically favorable. We will thus investigate the influence of this most stable CO adsorbate on the adsorption sites identified for atomic and molecular hydrogen. DFT computed adsorption energies for both atomic and molecular hydrogen are reported in Table 3.9. The atomic adsorption energies were computed with reference to the theoretical binding energy of H_2 in the PAW

Table 3.9: Adsorption energies per hydrogen atom or H_2 molecule on a precovered CO/Pd(210) surface ($\theta_{\mathrm{CO}} = 1$, CO at site E). For reference, the smallest C-H distance at each atomic adsorption site is also given. The notation of the sites refers to Fig. 3.18.

		E_{ad} [eV]		
Coverage	Site	Fixed slab	Relaxed slab	$d_{\mathrm{C-H}}$ [Å]
$\theta_{\mathrm{H}} = 1$	C’	0.22	0.31	2.83
	C”	0.19	0.27	2.56
	A	0.09	0.13	2.79
	B	—	—	2.25
$\theta_{\mathrm{H_2}} = 1$	D	−0.04	−0.01	

pseudopotential approximation as given in Table 3.3.

The overall trend is a significant reduction of adsorption energies at all sites. Most significantly, the molecular adsorption energy at the top Pd atom is now even slightly negative with respect to the gas phase H_2 energy, although it is still a metastable site separated by a barrier from the vacuum. Among the atomic adsorption sites, the threefold coordinated site C' is the only one to remain somewhat reactive with respect to hydrogen adsorption. Due to the adsorbed CO molecule, the mirror symmetry along $[1\bar{2}0]$ and thus the degeneracy of sites C' and C" is removed: The adsorption energy at site C" is slightly reduced in comparison to site C' as the distance of the hydrogen molecule to the neighboring CO molecules is shorter. At the step site B, the most reactive one on the clean (210) surface, atomic hydrogen is no longer stable as the hydrogen is pushed to the neighboring C' site instead. This can be understood by looking at the dissociation of formyl, HCO, on a metal surface [150]. Once the carbon-bonded hydrogen (starting from a gas-phase bond length of approximately 1.1 Å) is slightly separated from the carbon atom, both being in contact with the metal surface, the hydrogen is strongly repelled and separates itself from the remaining CO. In this context, it is clear that the hydrogen molecule tries to maximize its distance to all neighboring CO molecules.

The large decrease in hydrogen adsorption energies can also be understood in terms of the *d*-band model. Analogously to the situation of a Pd(210) surface pre-covered with hydrogen, the *d*-band center is reduced with respect to its value on the clean surface. Upon CO adsorption, the *d*-band center of the top Pd atom shifts from $\varepsilon_d = -1.26$ eV to $\varepsilon_d = -1.82$ eV. Due to the large interaction of the CO molecule with its neighboring Pd atoms, this shift is much larger than in the case of a monolayer of atomic hydrogen. Besides any possible direct repulsion of the CO and H_2 molecules, this large down-shift thus explains the rather large decrease in reactivity of the CO-covered surface.

In agreement with our theoretical results, coadsorption experiments of CO and H_2 showed a strong inhibition of hydrogen adsorption [102]. A CO pre-coverage of $\theta = 1$ essentially prevented any dissociative adsorption of H_2 to the H-β states and also molecular chemisorption of the H_2-γ_2 state. At dilute CO coverages, atomic hydrogen adsorption is still partially possible, that is mainly adsorption of the H-β_2 state. Based on the DFT results at coverage $\theta = 1$, and especially the strong influence of the CO adsorbate on the Pd substrate, no site assignment can be done. At low adsorption temperatures, experimental evidence hints at the stabilization of the H_2-γ_2 state on a CO-pre-covered surface. Our DFT results, however, do not support this hypothesis. Instead, molecular H_2 adsorption should be completely inhibited.

In the past two sections, we have analyzed CO adsorption on the (210) surface of palladium. It was found that the variation of the CO binding energy is comparably small across different adsorption sites and that bonding of CO is a very local process. At the most favorable bridge site on the (100) terrace, CO adsorbs inclined with respect to the surface normal, and analysis of the LDOS yielded a very similar picture to the one found on a flat (100) surface. Due to the strong modification of the Pd *d*-band upon CO adsorption, coadsorption of hydrogen is largely inhibited. A confirmation of the site assignment for atomic and molecular hydrogen by doing a coadsorption experiment and using a simple site-blocking argument is thus not possible.

Chapter 4

Adsorption on metal overlayers: nPt/Ru(0001)

In the previous chapter, we have studied the adsorption properties on a stepped surface. Due to their different coordination, the surface atoms exhibited different reactivity, with the atom right at the step being the most reactive one. As shown, the reactivity of each atom can be characterized by the center of its respective, locally projected d states. However, these properties are intrinsic to the specific surface structure and cannot be changed.

Modifying the reactivity of a surface by systematically altering its electronic structure is an intriguing and fascinating idea. One way to achieve this goal is the application of external strain on the substrate. Compressing or expanding any metal substrate changes the overlap of the atomic orbitals and thus consequently increases or decreases the width of the electronic bands. The effect of a lattice expansion on the d-band density of states of a transition metal such as ruthenium with a more than half-filled band is illustrated in Fig. 4.1: Expanding the lattice to a larger lattice constant leads to less overlap and thus a narrowing of the d-band. This in turn causes an up-shift of the center of the d states in order to preserve the degree of d-band filling. The energetic position of the d-band center shifts closer to the Fermi level resulting in a larger reactivity according to the d-band model (cf. Sec. 2.2.5, [86, 151]). The reverse is true for compressed lattices: Compression causes a down-shift and thus a lower reactivity.

Experimentally, however, the application of external strain on a large scale is difficult. Metals easily form dislocations, and significant deformations are thus not possible. Nevertheless, it was shown experimentally [152] that oxygen adsorption on Ru(0001) preferentially occurs on local areas with expanded lattices, whereas compressed lattice areas are depleted. In these experiments, the Ru surface layers were strained locally by argon implementation into subsurface cavities: At their rim, the lattice was compressed, whereas it was expanded at their top. Although these experiments proved the concept to be right, it does not allow for a quantitative assessment of the effect as the

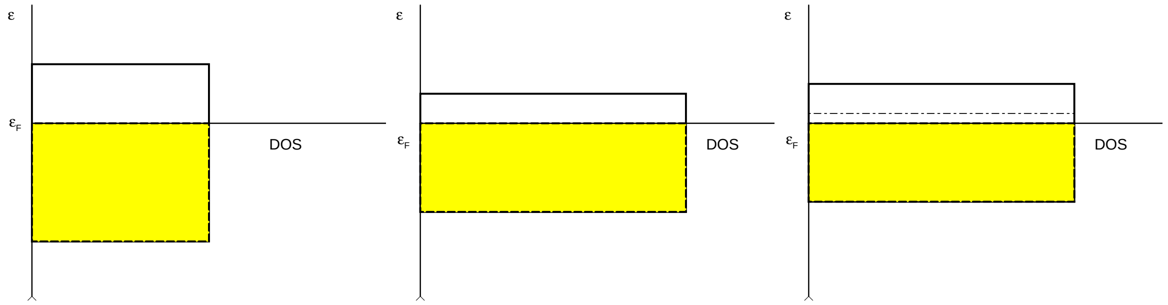

Figure 4.1: Rigid band model: The left panel shows the original d-band density of states. Expanding the surface leads to less overlap of the atomic orbitals and thus to a narrowing of the d-band (middle panel). Due to charge conservation, narrowing causes a shift of the d-band. As displayed in the right panel, the center of the d-band is shifted up for a more than half-filled bands [60, 86].

strain is only applied locally in a non-uniform way.

To achieve a macroscopic, uniformly strained surface, another approach has to be used: Growing a metal film pseudomorphically on top of a different metal substrate, it is possible to obtain overlayers compressed or expanded to the lattice constant of the underlying substrate. At some point, however, the strained layers will relax and continue to grow at their own lattice constant. If this interaction of the first or second overlayer with its metal substrate reduces the reactivity, it is desirable to be able to grow the overlayer film thick enough so that all substrate interactions are negligible.

As shown experimentally [16, 153], platinum overlayers deposited on a Ru(0001) grow pseudomorphically up to a film thickness of 10 layers. Compared to its own lattice constant, the platinum overlayers are compressed by 2.5% to adapt to the ruthenium lattice constant. This heteroepitaxial metal layer system thus allows for a discrimination of pure strain effects and effects due to a residual interaction with the underlying substrate. Denoting the number of grown Pt layers by n, we indicate the film thickness by nPt/Ru(0001) in our notation.

In the following sections, we will examine the properties of the nPt/Ru(0001) overlayer system theoretically. We will first determine the pseudomorphic structure of up to five deposited layers of Pt in Sec. 4.1. How atomic and molecular oxygen adsorption is affected and modified by different film thicknesses will be discussed in the next two sections, Sec. 4.2 and 4.3. Finally, the effects on CO adsorption are presented in Sec. 4.4 and compared to recent experiments.

4.1 Layer structure of nPt/Ru(0001)

All calculations presented in this chapter were again performed using the Vienna *ab initio* simulation package (VASP) [43, 45, 46, 55] with the PW91 generalized gradient approximation [33], and, where appropriate, including spin polarization. Ionic cores are described by projector augmented wave (PAW) pseudopotentials [57, 58], with projections done in real space. The surface itself was modeled using supercells of

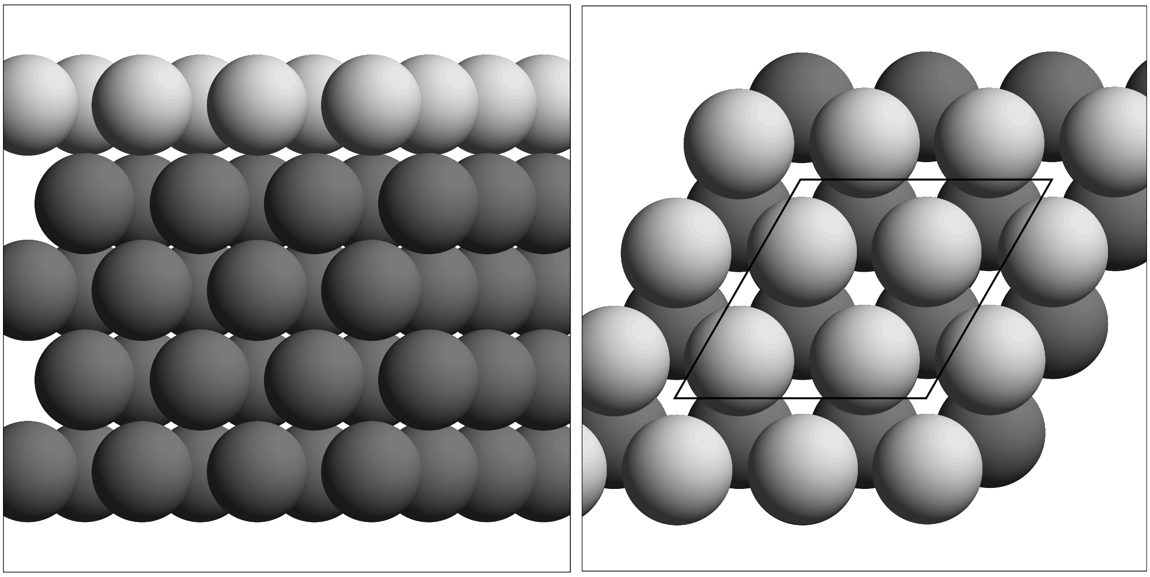

Figure 4.2: Side and top view of the Ru(0001) surface covered with a pseudomorphic overlayer of platinum. Ruthenium atoms are shown in dark grey, platinum atoms in light grey. In the right panel, the $p(2 \times 2)$ surface unit cell is included.

different size: The Ru(0001) substrate was always represented by a four layer thick slab. On top of this substrate, one to five overlayers of laterally compressed Pt were considered (see Fig. 4.2). For comparison, all adsorption calculations were also done on two four-layer slabs of platinum, one of which was unstrained with its computed nearest neighbor distance of bulk Pt, whereas the other was compressed horizontally to match the computed nearest neighbor distance of bulk Ru. The latter slab thus served as a model for an infinitely thick stack of laterally compressed Pt overlayers. Calculations using this compressed slab will be denoted as “Pt(111)@Ru”. The separating vacuum region was chosen to be 12 Å and kept constant. The supercell size in the z direction perpendicular to the surface thus varied between 18.5 and 30.4 Å.

The Brillouin zone of the $p(1 \times 1)$ slab was sampled using a Γ-centered Monkhorst-Pack mesh of $12 \times 12 \times 1$ $\mathbf{k}$ points [39], together with a first-order Methfessel-Paxton smearing [40] of width $\sigma = 0.2$ eV. Reported total energies are extrapolated to $\sigma \rightarrow 0$ eV. The valence states were expanded in a basis of plane waves with kinetic energies below 290 eV. For adsorption calculations using a $p(2 \times 2)$ surface unit cell, a Monkhorst-Pack mesh of $4 \times 4 \times 1$ $\mathbf{k}$ points and, due to the harder oxygen core, a higher energy cut-off of 400 eV were necessary to obtain converged total energies. Geometrical relaxations were carried out using the Hellman-Feynman forces and a conjugate-gradient minimization scheme. In all calculations, the two bottom Ru or Pt layers were kept fixed at their truncated bulk positions whereas all other layers were relaxed such that the forces on each atom were below 0.02 eV/Å.

Lattice constants for both bulk platinum and ruthenium were obtained by fitting the Murnaghan equation of state to the computed total energies at several different lattice parameters. For the hexagonal lattice of ruthenium, both lattice parameters a

and c would need to be optimized. However, as a previous VASP study [154] showed that the c/a ratio obtained by a full optimization using the GGA functional is $c/a = 1.58$, we kept the c/a ratio fixed to the experimental value of $c/a = 1.582$. The theoretical Ru nearest neighbor distance was then determined to be 2.73 Å, a bit larger (1.1%) than the experimental value. For Pt, a lattice constant of 3.99 Å was calculated in comparison to a slightly smaller (1.8%) experimental value of 3.92 Å. The in-plane Pt-Pt nearest neighbor distance of an unstrained Pt(111) slab is thus 2.82 Å. Both determined lattice constants are within the expected accuracy of the GGA exchange-correlation functional. Due to the different absolute deviations, the lattice mismatch of the theoretically computed lattice constants amounts to 3.2%, whereas the experimental lattice mismatch is only 2.6%. The effect of compressing the platinum layer to match the ruthenium lattice might thus be slightly overestimated within the GGA approximation.

When pseudomorphically growing a platinum overlayer on Ru(0001), the platinum atoms of the first overlayer can be either adsorbed in fcc hollow or hcp hollow positions. To determine the correct layer stacking with the lowest energy, all possible permutations for adsorption of each additional platinum overlayer were computed. Referring to the two top Ru layers as AB as denoted in Fig. 4.3, with the top layer being B, epitaxial growth of Pt can continue the stacking as either ABA (hcp hollow adsorption) or ABC (fcc hollow position). For the first overlayer, continuation of the hexagonally closed packed structure of Ru, sequence ABA, is favorable by 18 meV per $p(1 \times 1)$ surface unit cell compared to the sequence ABC. Starting with the second layer of platinum, however, growth switches to the face-centered cubic structure of bulk Pt. Adsorption of the second overlayer resulting in a stacking of ABAC is energetically favored by 31 meV in comparison to the next best structure of ABAB. Starting with the third overlayer, the platinum layers, although compressed by 3.2%, grow according to the fcc stacking found for bulk Pt. The lowest energy structure found for 5Pt/Ru(0001) is illustrated in Fig. 4.3. All further adsorption calculations will be performed using the discussed Pt film structure.

At all film thicknesses, a full relaxation of the Pt overlayers and the two topmost Ru layers was allowed. The computed interlayer distances are summarized in Table 4.2. The topmost Ru-Ru interlayer spacing, d_{3-4}, is found to be contracted by 3.7% to 2.08 Å, which is somewhat larger than the LEED-determined value of 2.3% [155]. Upon adsorption of Pt overlayers, this contraction is slightly reduced to 2.11 Å.

Table 4.1: Bulk properties of Pt and Ru as determined self-consistently by GGA-PAW calculations. Experimental data is taken from Kittel [103]. The c/a ratio of ruthenium was fixed to the experimental value.

	Ru		Pt	
	a [Å]	c/a	a [Å]	B_0 [GPa]
GGA-PAW	2.73	1.582	3.99	231
Exp.	2.70		3.92	230

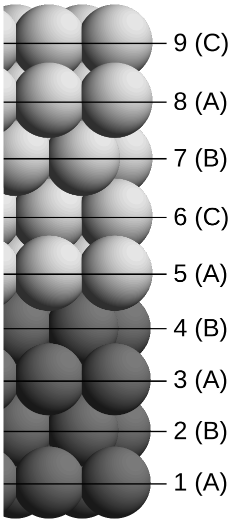

Figure 4.3: Stacking sequence of pseudomorphic platinum overlayers on Ru(0001). The first platinum layer (layer 5) continues the hexagonally close-packed structure of ruthenium (sequence AB). Beginning with the sixth layer, platinum starts to grow in its face-centered cubic structure (BAC sequence). Reported layer spacings refer to the layer numbers shown in the illustration.

The interlayer distance of the first Pt overlayer to the Ru substrate is initially found to be 2.31 Å and is further reduced to 2.28 Å as more Pt layers are grown on top. This Pt-Ru interlayer distance is almost identical to the interlayer distance of bulk Pt(111), $d_{\mathrm{Pt}(111)} = 2.30$ Å, although the layer is compressed significantly in-plane. Starting with the second Pt layer, the Pt-Pt interlayer distance is found to be approximately 2.41 Å, almost identical up to a film thickness of 5 layers within the accuracy of our numerical calculations. The lateral compression is thus compensated for by an increase of the layer distance from 2.30 Å to 2.41 Å.

Also given in Table 4.2 is the separation energy of each Pt overlayer. The separation energy is defined as the energy needed to completely separate the top-most layer from its remaining substrate while keeping the in-plane nearest-neighbor distances fixed. It is thus an indication of the strength of the chemical interaction between the surface layer and the substrate. For the first Pt overlayer, a rather large separation energy of 1.57 eV/atom is found, whereas adsorption of additional overlayers yields an almost constant energy gain of roughly 0.93 eV/atom. It has to be noted that the separation energy does not take into account any energy released due to the "assembly" of the free Pt monolayer: Compared to bulk Pt(111), a free monolayer of Pt actually tries to contract itself to compensate for the lack of bonding partners above and below. Compressing a free Pt(111) monolayer from its bulk lattice constant to the Ru lattice constant of 2.73 Å gives an energetical gain of $\Delta E = 0.24$ eV, with the energetic minimum being located at an even smaller Pt-Pt distance of approximately 2.62 Å [156]. In this sense, the surface termination of 1Pt/Ru(0001) is much more "ideal" for the top Pt layer than in uncompressed Pt(111). This is also true for *n*Pt/Ru(0001) and Pt(111)@Ru.

From the given structural data, it can thus be inferred that, starting with the third layer, growth of additional platinum overlayers is not influenced by electronic interactions with the Ru substrate any more. Growth is then only affected by the strain due to the pseudomorphic growth.

As discussed in the introduction of this chapter, the reactivity of a system, especially under strain, is mostly influenced by the *d*-band valence states, the key parameter being their energetic center, ε_d. The local *d*-band densities of states of the surface layers of Pt(111), Pt(111)@Ru, 1Pt/Ru(0001), and Ru(0001) are displayed in Fig. 4.4. The top panel shows both the *d*-LDOS of unstrained (solid line) and compressed (dashed line) Pt(111). Due to the compression and increased overlap, the *d*-band gets significantly broadened. Adsorption of a monolayer of Pt on Ru(0001) even further modifies the *d*-band distribution (middle panel of Fig. 4.4): Interaction with the Ru substrate reduces the density of states at the Fermi level and causes a further overall down-shift of the valence states.

This downshift can be quantified by determining the *d*-band center according to Eq. (2.27). For an accurate determination of the *d*-band center, a larger **k** point mesh of 16 × 16 × 1 was used and the number of bands was increased to make sure that all relevant states above the Fermi level are included. To avoid picking up any irrelevant noise above the actual *d* band due to the projection scheme, the integrals of Eq. (2.27) were truncated at the upper edge of the *d*-band. The *d*-band centers computed in the described way are summarized in Table 4.3. As expected from Fig. 4.4, the compression of Pt(111) to the Ru nearest neighbor distance causes a noticeable downshift of the *d*-band center from −2.23 eV to −2.37 eV. However, the influence of the Ru substrate on the first Pt overlayer is even stronger: Hybridization with the Ru orbitals lowers

Table 4.2: Layer relaxations of the system *n*Pt/Ru(0001). Reported layer distances d_{n-m} refer to the layer numbers given in Fig. 4.3. Printed in italics is the layer distance between the Ru substrate and the first Pt overlayer, d_{4-5}. For comparison, the interlayer distance of Ru(0001) at its bulk-truncated positions is $d_{\mathrm{Ru(0001)}} = 2.16$ Å(Exp. 2.14 Å[155]), that of Pt(111) $d_{\mathrm{Pt(111)}} = 2.30$ Å (Exp. 2.26 Å [103]). Also given is the energy to completely separate the top-most overlayer from the rest of the slab, ΔE_{sep}.

*n*Pt/Ru(0001)	0	1	2	3	4	5
d_{8-9} [Å]						2.41
d_{7-8} [Å]					2.41	2.40
d_{6-7} [Å]				2.42	2.41	2.41
d_{5-6} [Å]			2.41	2.40	2.40	2.41
d_{4-5} [Å]		*2.31*	*2.25*	*2.28*	*2.27*	*2.28*
d_{3-4} [Å]	2.08	2.08	2.11	2.11	2.10	2.11
d_{2-3} [Å]	2.14	2.14	2.13	2.13	2.13	2.13
ΔE_{sep} [eV/atom]		1.57	0.92	0.92	0.93	0.94

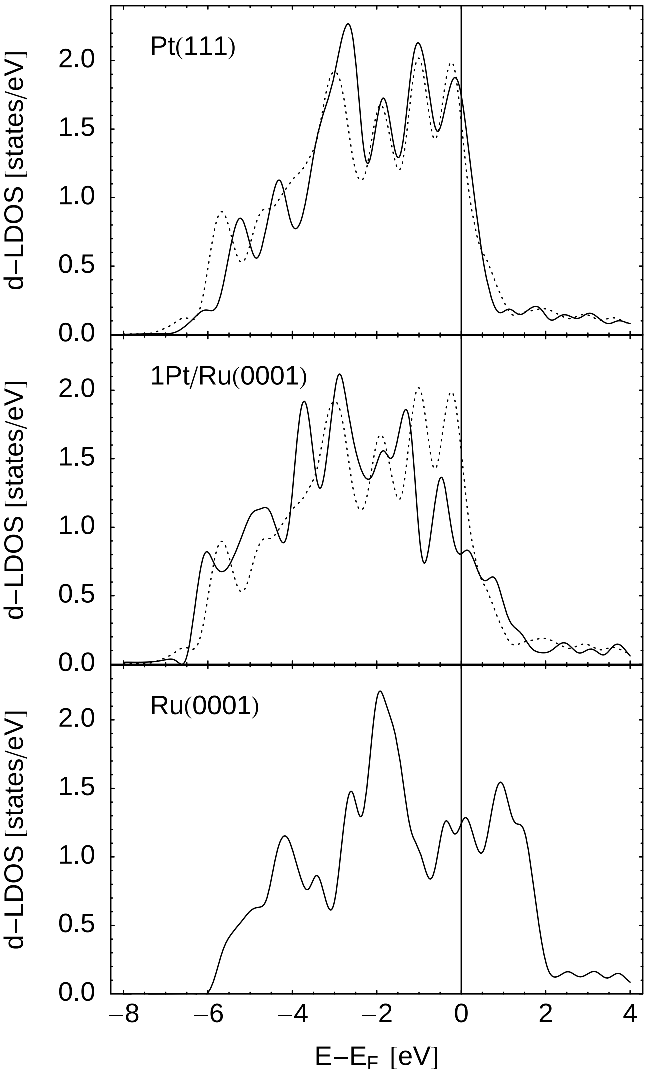

Figure 4.4: Local d-band density of states of nPt/Ru(0001). From top to bottom, the d-band LDOS of the surface layer of Pt(111), 1Pt/Ru(0001), and Ru(0001) are shown. For comparison, the LDOS of the compressed surface layer of the Pt(111)@Ru slab is also plotted as a dashed line.

the d-band center to -2.61 eV. Within the numerical accuracy, the d-band centers of the top layer of the systems Pt(111)@Ru and nPt/Ru(0001) with $n = 2 \ldots 5$ do not exhibit significant differences. Considering thus only the top layer, chemical reactivity of these systems should roughly be the same.

Finally, this trend is also confirmed by looking at the work function change with growing film thickness. The work function is computed as described in Sec. 2.2.3 by introducing a dipole layer in the vacuum region. As given in Table 4.3, the work function continually increases going from pure Ru(0001) over 1Pt/Ru(0001) and 2Pt/Ru(0001) to 3Pt/Ru(0001). From then on, the work function remains roughly constant with a value slightly larger than the one of unstrained Pt(111). That any influence of the substrate decays within three overlayers can also be seen in Fig. 4.5. Shown are the charge

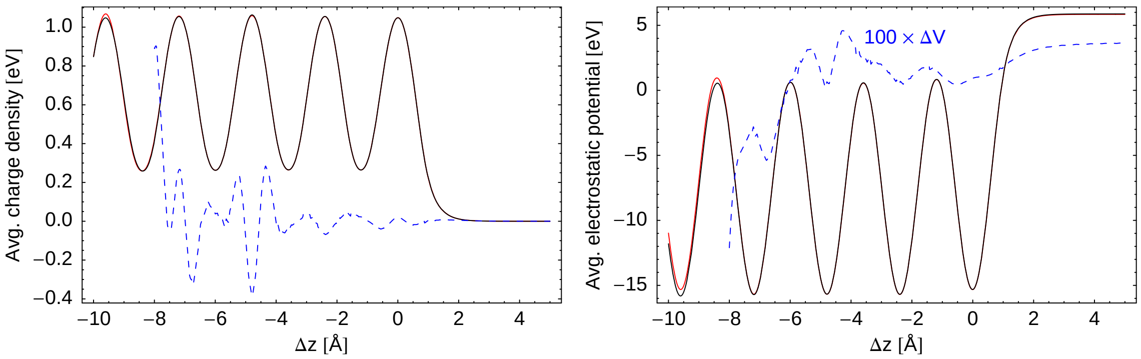

Figure 4.5: Charge density (left) and electrostatic potential (right) of the 5Pt/Ru(0001) surface (solid lines) in comparison to a 5-layer Pt slab at the same coordinates with the underlying Ru substrate removed (shaded). The difference between the two curves is magnified by a factor of 100 and displayed as a dashed line. The constant offset in the electrostatic potential for $\Delta z > 2$ Å is due to numerical inaccuracy.

densities and electrostatic potentials of the system 5Pt/Ru(0001). The solid lines represent the data of the full system, whereas the shaded lines represent were computed using only a 5-layer Pt slab at exactly the same coordinates, but with the ruthenium substrate removed. The difference is barely visible at the first Pt layer ($\Delta z \approx -9.6$ Å) which, for the 5-layer slab, is in direct contact with the vacuum region. Magnifying the difference by a factor of 100 (dashed line) reveals that both charge density and electrostatic potential are distinguishable only within the first three layers. This is in agreement with the conventional wisdom that a slab size of three to four layers for a close-packed surface is sufficient for an accurate representation of the surface.

Based on the properties of the clean nPt/Ru(0001), we can thus conclude that the influence of the Ru substrate should be vanished starting with the third Pt layer. For

Table 4.3: Computed d-band centers and work functions of nPt/Ru(0001). Experimental data is taken from Chiarotti [108] and represents orientation-specific measurements. For Pt(111), two different experimental values are quoted.

		Φ [eV]	
	ε_d [eV]	Theory	Exp.
Ru(0001)	−1.54	5.12	5.37
1Pt/Ru(0001)	−2.61	5.46	
2Pt/Ru(0001)	−2.38	5.71	
3Pt/Ru(0001)	−2.32	5.88	
4Pt/Ru(0001)	−2.35	5.82	
5Pt/Ru(0001)	−2.36	5.85	
Pt(111)@Ru	−2.37	5.84	
Pt(111)	−2.23	5.80	5.93 / 5.82

$n = 1$, we expect a large modification of adsorption properties due to the observed strong interaction of the Pt monolayer with the Ru substrate. Starting with $n = 3$, however, residual interactions should have vanished and the remaining modifications should solely be due to the strain on the Pt layers.

4.2 Atomic adsorption of oxygen

Oxygen adsorption on Pt(111) is a well-studied system, both experimentally [157–162] and theoretically [163–167]. It is well-established that, at a coverage of $\theta = 0.25$, oxygen forms a $p(2 \times 2)$ superstructure with the oxygen atoms being adsorbed in fcc hollow positions (no atom in the layer beneath the site). On the other hand, on Ru(0001), again a $p(2 \times 2)$ superstructure is found, but with the oxygen atoms occupying hcp hollow positions [168–170]. In the following, we will thus check how the application of strain and the residual interaction of the ruthenium substrate influences the adsorption of a $p(2 \times 2)$ layer of atomic oxygen.

Adsorption energies of oxygen will be reported with respect to the free O_2 molecule in the gas phase. Oxygen is known to be problematic within the DFT pseudopotential approach due to its hard core. It is the main reason for the large energy cut-off of 400 eV in our calculations. The O_2 ground state properties were obtained from a Morse potential fit and are compared to the experimental data in Table 4.4. Although the binding energy obtained using ultrasoft pseudopotentials is significantly closer the experimental value, the PAW result is indeed very close to all-electron calculations for O_2 [35]. It is thus only by chance that the induced error due to a softer, inaccurate core region counterbalances the DFT error due to the exchange-correlation functional. We will use PAW potentials throughout this chapter and refer adsorption energies to the PAW binding energy of $E_b = 6.27$ eV.

Final adsorption energies for oxygen in the fcc hollow, hcp hollow, and bridge sites are displayed in Fig. 4.6. All atoms except the two bottom slab layers were allowed to relax completely. In the case of bridge adsorption, the oxygen atom was fixed horizontally, however. Adsorption energies for the fcc hollow position are also listed in Table 4.5 together with the computed oxygen-metal distances. All relaxations yielded a small buckling of the surface layers on the order of 0.1 Å, in good agreement with the observed small buckling on both the Ru(0001) [168] and Pt(111) [158, 159] surfaces.

Table 4.4: Binding energy, bond length, and stretching frequency for the O_2 molecule. Experimental data is taken from Herzberg and Huber [115].

	O_2		
	E_b [eV]	d [Å]	ω [cm^{-1}]
GGA-USPP	5.86	1.24	1572
GGA-PAW	6.27	1.24	1567
Exp.	5.21	1.21	1580

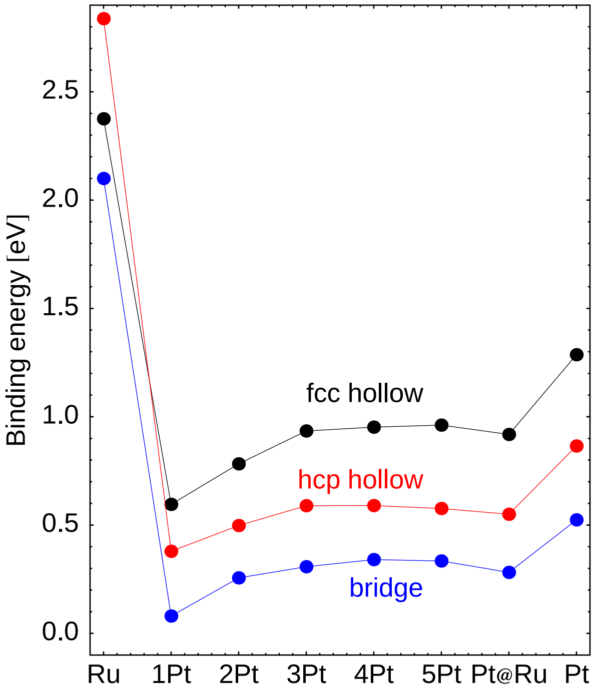

Figure 4.6: Adsorption energies of $p(2 \times 2)$-O/nPt/Ru(0001). Shown are the energies per atom for adsorption in the fcc hollow, hcp hollow and bridge sites with respect to free O_2 molecule. Energies on the strained Pt slab are denoted as "Pt@Ru", on the uncompressed Pt slab as "Pt". Except on Ru(0001), adsorption in the fcc hollow site is energetically favorable. Binding energies with respect to free atomic O may be obtained by adding half the binding energy of O_2, 3.13 eV, to the given binding energy.

The height of the oxygen atom, $\Delta z_{\mathrm{O-Me}}$, given in Table 4.5, is calculated using the relaxed nearest neighbor distances, i.e., the height of the oxygen atom with respect to the clean surface is slightly larger due to the outward relaxation of the nearest neighbors.

Ignoring the binding energies on clean Ru(0001), all three energy curves in Fig. 4.6 show the same trend: Compressing the platinum slab to the Ru lattice constant, decreases the adsorption energy by roughly 0.3 eV. A monolayer of Pt on top of Ru(0001) exhibits another drastic reduction in binding energy by 0.3 eV compared to the compressed Pt(111) slab. The systems with 3 to 5 layers of platinum yield roughly the same adsorption energy as the strained Pt slab, whereas adsorption energies on the 2Pt/Ru(0001) system are still significantly reduced. This clearly shows that the electronic properties of the second layer atoms still prove to be relevant for the adsorption process as also found on other systems [171, 172].

The compression of the Pt(111) surface also alters the vibrational properties of the adsorbed oxygen atom. On the unstrained Pt(111), by using a cubic fit to the total energies at elongated positions of $\Delta z = 0.00, \pm 0.05$, and ± 0.10 Å, we obtain a vibrational frequency for the symmetric mode perpendicular to the surface of 448 cm^{-1}.

This is somewhat lower than the value of 475 cm^{-1} obtained using the LDA approximation [165] or the value of 477 cm^{-1} found experimentally [157, 161]. Nevertheless, all theoretically reported frequencies do not take into account the finite mass of the substrate atoms. By using a simple spring model for the threefold hollow adsorption scenario, the first-order correction due to the finite mass of the substrate atoms can be found to be [173]

$$\omega = \omega(M_s \to \infty)\sqrt{1 + \frac{M_a}{3M_s \cos^2 \alpha}}, \tag{4.1}$$

where $\omega(M_s \to \infty)$ is the frequency obtained in the limit of infinite substrate mass, M_a and M_s are the mass of the adsorbate and substrate atoms, respectively, and $\cos\alpha = \frac{\Delta z_{\mathrm{O-Me}}}{d_{\mathrm{O-Me}}}$. Applying this correction formula to our computed frequency gives $\omega = 467$ cm^{-1}, in much better agreement with the experimentally observed frequency. On the compressed Pt(111) surface, the frequency is increased to 485 cm^{-1} (503 cm^{-1} after finite mass correction). Experimentally, a similar trend towards a higher frequency is observed, but only with a very small shift to $\omega = 483.7$ cm^{-1} [16].

So far, we did not discuss oxygen adsorption on Ru(0001): As can be seen in Fig. 4.6, adsorption of oxygen in the hcp hollow positions is favored by 0.46 eV ($E_b = 2.84$ eV) in contrast to the opposite ordering on Pt(111) where the fcc hollow position is preferred by 0.42 eV. For 1Pt/Ru(0001) and 2Pt/Ru(0001) the preferential occupation of the fcc hollow site is already weakened by the influence of the underlying Ru substrate as can be inferred from the decreasing energy difference between fcc hollow and hcp hollow adsorption energies.

Feibelman [164] suggested that the large fcc hollow versus hcp hollow binding preference of oxygen on Pt(111) was due to "*d*-electron frustration" in the bonding between first and second layers. The adsorption scenario in both fcc hollow and hcp hollow sites is illustrated in Fig. 4.7, together with labels for the first and second layer metal atoms

Table 4.5: Adsorption energies and geometries for $p(2\times2)$-O/nPt/Ru(0001) for adsorption in the fcc hollow position. Listed are the binding energy per oxygen atom with respect to the free O_2 molecule, E_b, the oxygen-metal distance, $d_{\mathrm{O-Me}}$, the height of the oxygen atom above the top-most metal atom, $\Delta z_{\mathrm{O-Me}}$, and the characteristic frequency for vibrations along the surface normal, ω. Frequencies in parentheses are corrected for the finite mass of the substrate atoms.

	E_b [eV]	$d_{\mathrm{O-Me}}$ [Å]	$\Delta z_{\mathrm{O-Me}}$ [Å]	ω [cm^{-1}]
Ru(0001)	2.38	2.03	1.14	
1Pt/Ru(0001)	0.60	2.10	1.36	
2Pt/Ru(0001)	0.78	2.05	1.26	
3Pt/Ru(0001)	0.93	2.05	1.25	487 (504)
4Pt/Ru(0001)	0.95	2.05	1.25	
5Pt/Ru(0001)	0.96	2.05	1.25	
Pt(111)@Ru	0.92	2.04	1.25	485 (503)
Pt(111)	1.29	2.04	1.14	448 (467)

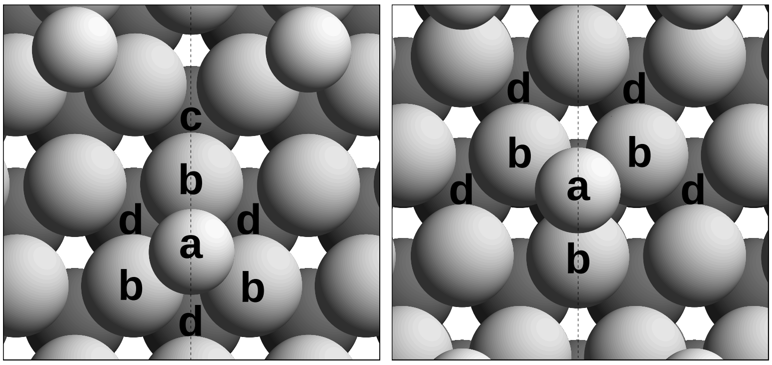

Figure 4.7: Top view of the fcc hollow (left panel) and hcp hollow (right panel) adsorption geometry. The notation of the nearest neighbor atoms refers to the one used by Feibelman [164]. In the right panel, the second-layer atom c is hidden and located directly below the oxygen atom a. In both views, the dashed line indicates the section of the contour plots of Fig. 4.8.

participating in the bonding. The key idea in Feibelman's concept is that the electronegative oxygen adatom a drives the d electrons on each neighboring Pt atom b away from the O-Pt bond direction. The effect is the depletion of d electrons along the O-Pt bond effectively creating a partially emptied d_σ orbital along this direction. Each first-layer Pt atom b now has three nearest neighbors in the second layer (labeled c and d), two of them being symmetrically identical (d). In the fcc hollow geometry, the orientation of the partially emptied d_σ orbital is directed towards the sub-surface atom c. As the Pt d band is almost completely filled, charge is thus effectively removed locally from antibonding orbitals. The charge deformation is also strongest close to the Pt atom and weaker in the nodal region between the neighboring Pt atoms as one would expect if charge is removed from an antibonding orbital with a node between the two atoms. The charge depletion of the d_σ orbital thus effectively strengthens the bond between atoms b and c. In contrast, no second-layer bonding partner is available in the hcp hollow geometry and antibonding charge is instead added into the bonds to sub-surface atoms c and d. The d_σ hole can thus not be oriented in an energetically optimal way and is "frustrated".

That this scenario is also valid for compressed Pt(111) can be seen in the charge density contour plots of Fig. 4.8 and the calculated bond lengths in Table 4.6. In the two contour plots at the bottom of Fig. 4.8, the deformation of the charge density at atom b is clearly visible, most pronounced for the O-like bulged contour at a charge density of 2.0 electrons/Å^3. For oxygen in an fcc hollow position, the charge depletion directly strengthens the b-c interaction. However, in the case of hcp hollow adsorption, the charge is instead added to the b-c bond and the bond is weakened. This is also manifested in the calculated bond lengths shown in Table 4.6 for Pt(111)@Ru: Compared to the nearest neighbor distance of 2.88 Å of the clean, but fully relaxed surface, only the b-c distance is shortened to 2.77 Å upon oxygen adsorption, whereas all other distances are expanded. The net result is that the fcc hollow position is preferred by 0.37 eV on compressed Pt(111).

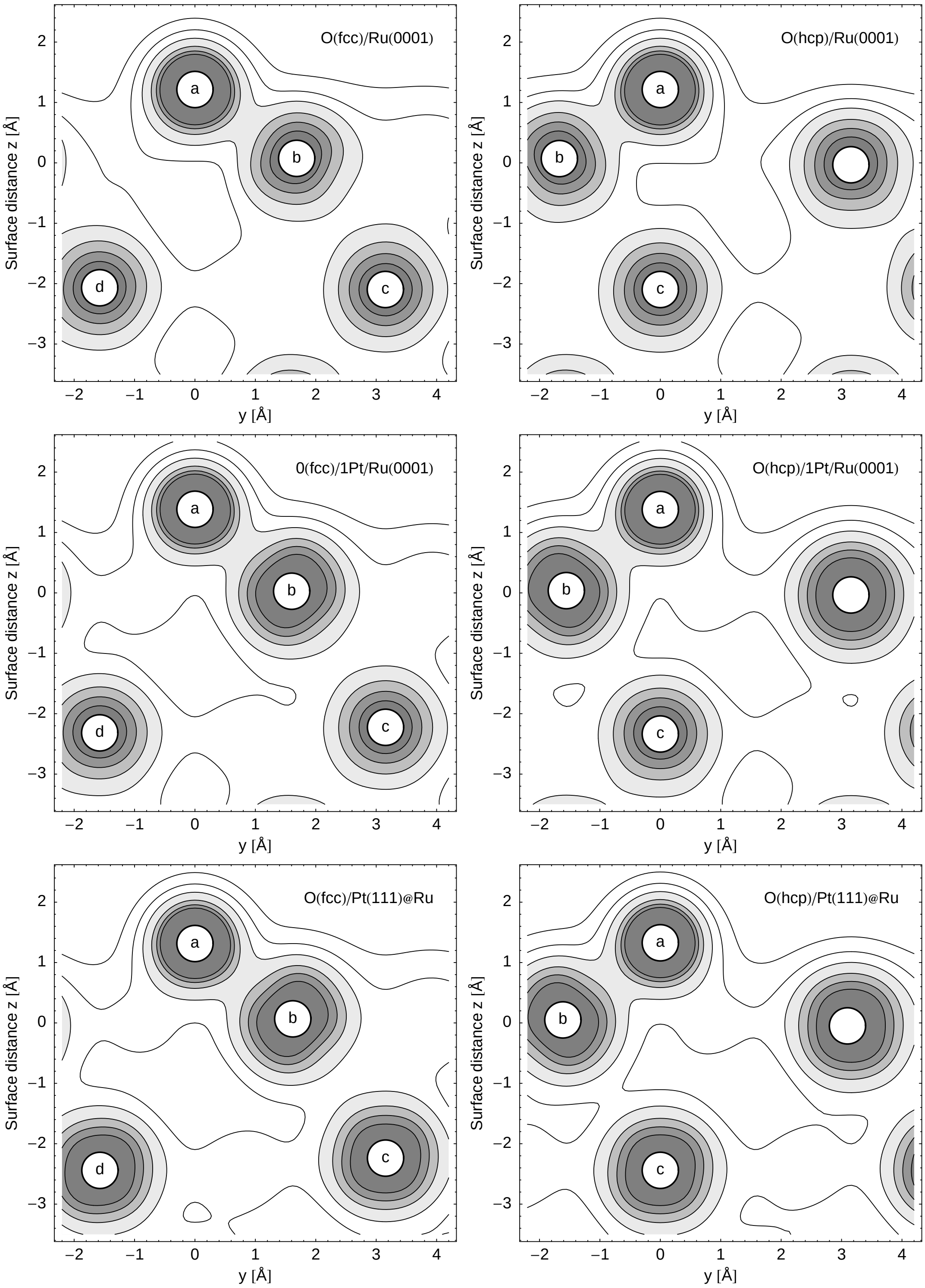

Figure 4.8: Contours of constant charge density for $p(2\times2)$ adsorption of oxygen in the fcc hollow (left column) and hcp hollow positions (right column) on Ru(0001), 1Pt/Ru(0001), and compressed Pt(111). Contour lines are drawn at charge densities of 0.1, 0.25, 0.5, 1.0, 1.5, and 2.0 electrons/Å^3. The labels refer to those defined in Fig. 4.7.

Table 4.6: Calculated bond lengths for $p(2 \times 2)$-O/nPt/Ru(0001) adsorption in fcc and hcp hollows. The labels refer to those used in Table 4.7. For comparison, the nearest neighbor distances of the clean surface are also given ($d_{bc} = d_{bd}$).

	Distance	O(fcc)	O(hcp)	no O
Ru(0001)	d_{ab} [Å]	2.03	2.02	2.60
	d_{bc} [Å]	2.62	2.74	
	d_{bd} [Å]	2.70	2.60	
1Pt/Ru(0001)	d_{ab} [Å]	2.10	2.09	2.80
	d_{bc} [Å]	2.74	2.86	
	d_{bd} [Å]	2.83	2.81	
Pt(111)@Ru	d_{ab} [Å]	2.04	2.06	2.88
	d_{bc} [Å]	2.77	2.97	
	d_{bd} [Å]	2.97	2.90	

The scenario is still rather similar for oxygen adsorption on 1Pt/Ru(0001): The charge density deformation is almost identical and again clearly favors fcc hollow adsorption. The change in bond lengths, however, is less pronounced than on Pt(111)@Ru, but still follows the same pattern, i.e., strengthening of the *b*-*c* bond for fcc adsorption and weakening all other bonds.

In contrast, the charge density contour plot for adsorption on Ru(0001) is less instructive: The charge density is still considerably deformed in an O-like manner, though significantly less than for Pt(111), and the d_σ hole is no longer oriented towards the sub-surface layer atom c as directly as for Pt(111). The net effect is a weakening of all bonds upon oxygen adsorption. However, although this might be held responsible for less attractive adsorption in the fcc hollow site, it does not explain why there is such a large energetical preference for the hcp hollow site on Ru(0001).

Nevertheless, the model of d-electron frustration is still applicable to compressed Pt films even down to a single monolayer and clearly reveals the importance of the sub-surface layer to the bonding of oxygen.

4.3 Molecular adsorption of O_2

Atomic oxygen adsorption on Pt(111) is known to be mediated by molecular precursors [157, 174–176], although the precise adsorption process is still debated [177]. In molecular beam experiments, two distinct molecular precursors were identified: A superoxo-like (O_2^-) species formed at bridge sites with an intramolecular bond order of 1.5 and a vibrational frequency of 870 cm^{-1}, and a peroxo-like (O_2^{2-}), slightly stronger bound species adsorbed at threefold hollow sites exhibiting an intramolecular bond order of 1 and a vibrational frequency of 690 cm^{-1}.

Theoretical GGA-DFT studies corroborated this hypothesis [178, 179]: The su-

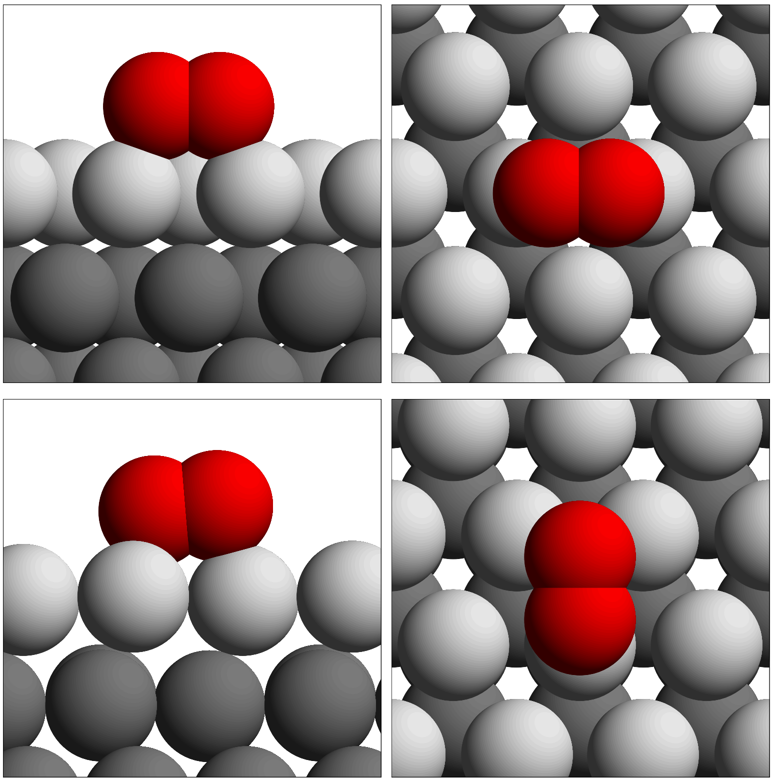

Figure 4.9: Top panels: Side and top view of the O_2^- molecular precursor state (superoxo state) on the 1Pt/Ru(0001) surface. The orientation of the O_2 molecule is t-b-t. Bottom panels: Side and top view of the O_2^{2-} molecular precursor state (peroxo state). The orientation is b-fcc-t, and the molecule is tilted by 7° off the (111) plane.

peroxo precursor state was found to be adsorbed in a top-bridge-top (t-b-t) orientation on the Pt(111) surface with a remaining magnetic moment of $m_{O_2} = 0.4\mu_B$ (cf. Fig. 4.9). The peroxo molecular precursor, on the other hand, is identified as being adsorbed non-magnetically in a top-fcc hollow-bridge (t-fcc-b) orientation. The peroxo species is tilted by 10.8° off the (111) plane. The PW91-GGA calculations [178] yielded adsorption energies of $E_b = 0.72$ eV and $E_b = 0.68$ eV for the superoxo and peroxo species, respectively. Experimentally, the adsorption energies were estimated to be approximately 0.5 eV [157], and it has to be noted that the uncertainty due to the approximative exchange-correlation functional is rather large for systems involving oxygen. This can already be seen from the substantial error in the binding energy of O_2 (see Table 4.4), and resulting binding energies computed with different exchange-correlation functionals vary widely. Computations using the RPBE functional, e.g., yield much lower binding energies of $E_b \approx 0.1$ eV only [180, 181].

As measurements of initial sticking probabilities of O_2 on nPt/Ru(0001) exist [16], we will use these molecular precursors as another probe of the specific properties of the nPt/Ru(0001) system.

The molecular adsorption calculations were done in a $p(2 \times 2)$ geometry. This effectively doubles the oxygen coverage per cell in comparison to the previous section, but

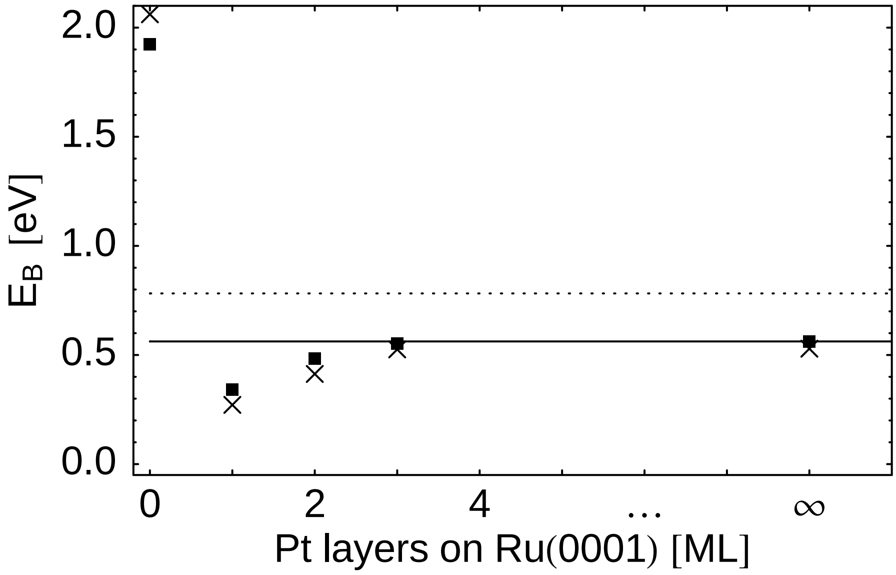

Figure 4.10: O_2 molecular adsorption energies on nPt/Ru(0001) using a $p(2 \times 2)$ surface unit cell. Both adsorption energies of the O_2^- superoxo precursor (solid box) and the O_2^{2-} peroxo precursor (×) are shown. The solid line marks the final adsorption energy of O_2^- for compressed Pt(111). The adsorption energy of the O_2^- superoxo precursor on unstrained Pt(111) is indicated by the dashed line.

interaction of neighboring O_2 molecules are still considered to be small. In contrast to the original study of O_2 on Pt(111) by Eichler and Hafner [178], we do not use a $\sqrt{3} \times 2$ unit cell. Using this rectangular cell does not represent the C_{3v} symmetry of the hexagonal Ru lattice accurately. With no adsorbate present, the **k** point mesh is symmetrized accordingly. But as soon as an oxygen molecule is present, the C_{3v} symmetry is broken and **k** along the two surface unit cell vectors are no longer equivalent. For larger slabs of nPt/Ru(0001) with $n > 2$, this turned out to be a significant disadvantage as rather large numerical drifts in the computed Hellman-Feynman forces rendered relaxations for such slabs useless. In a $p(2 \times 2)$ geometry, both unit cell directions and thus **k** points along them are related by the intrinsic symmetry of the slab. Therefore, any symmetry violations of the computed forces are avoided.

On the unstrained Pt(111) slab, the binding energies of O_2 are determined to be almost degenerate, i.e., $E_b = 0.80$ eV and $E_b = 0.78$ eV for the O_2^{2-} peroxo and the O_2^- superoxo precursor, respectively. The energetical ordering of the two molecular precursor states is thus reverted in comparison to the original $\sqrt{3} \times 2$ results cited above [178]. Due to the different geometry, this might be simply attributed to O-O repulsion effects, as the O-O distance of neighboring peroxo precursors is changed from roughly 3.5 Å in a $\sqrt{3} \times 2$ unit cell to 4.5 Å in a $p(2 \times 2)$ unit cell.

All results for nPt/Ru(0001) are summarized in Fig. 4.10 and Table 4.7. The expected trend of decreasing reactivity and lower binding energies going from Pt(111) over compressed Pt(111) to 1Pt/Ru(0001) is again observed. For all nPt/Ru(0001) surfaces, the superoxo precursor is slightly stronger bound than the peroxo precursor

Table 4.7: Adsorption energies and geometries for molecular oxygen adsorption on nPt/Ru(0001). Binding energies and bond lengths for both the O_2^{2-} peroxo and the O_2^- superoxo precursor are given. For the spin-polarized O_2^- state, total magnetic moments and stretching frequencies as well as the experimentally determined initial sticking coefficient [16] are also reported.

	O_2^{2-}		O_2^-				
	E_b [eV]	d_{O-O} [Å]	E_b [eV]	d_{O-O} [Å]	μ [μ_B]	ω [cm^{-1}]	S_0 [16]
Ru(0001)	2.06	1.48	1.92	1.42	0.00	749	
1Pt/Ru(0001)	0.27	1.38	0.34	1.34	0.82	1007	0.00
2Pt/Ru(0001)	0.41	1.38	0.48	1.34	0.75	961	0.0012
3Pt/Ru(0001)	0.53	1.39	0.55	1.36	0.70	913	0.006
Pt(111)@Ru	0.53	1.38	0.56	1.35	0.79	940	0.06
Pt(111)	0.80	1.40	0.78	1.36	0.61	908	0.20

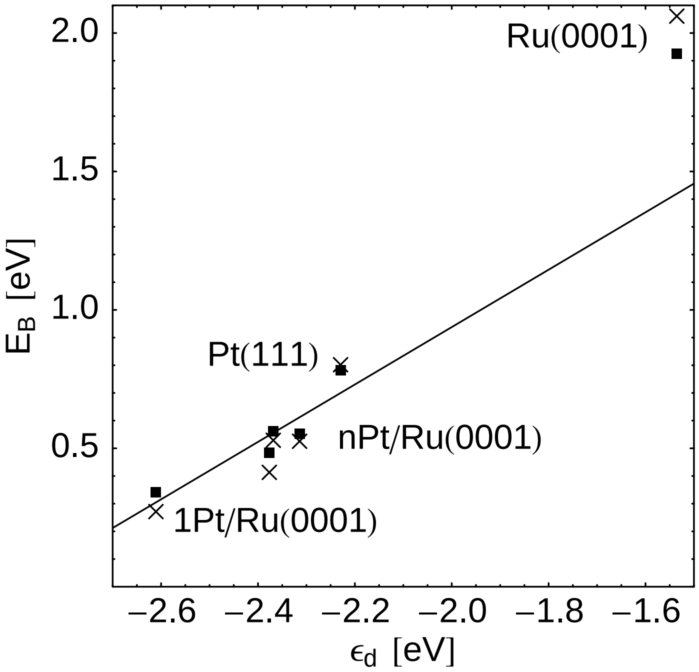

Figure 4.11: Molecular O_2 adsorption energy versus *d*-band center (with respect to the Fermi energy) of the surface Pt atom for a $p(2 \times 2)$ ordered overlayer. Both adsorption energies of the O_2^- superoxo precursor (solid box) and the O_2^{2-} peroxo precursor (×) are shown. The solid line represents the best least-squares linear fit to the O_2^- energies [excluding the one on Ru(0001)].

contrary to unstrained Pt(111). For the t-b-t orientation of the superoxo precursor, compressing the lattice constant seems to be more favorable as it allows the molecule to adsorb with a slightly smaller O-O bond length.

For the O_2^- superoxo precursor, we have also determined magnetic moments and vibrational frequencies. The magnetic moments given are total magnetic moments of the whole slab, with most of the polarized charge located at the oxygen atoms. The spin polarization of the adsorbed O_2 molecule is clearly correlated with its binding energy: The weaker the binding to the metal substrate, the more of the gas phase polarization of $\mu = 2\mu_B$ is preserved. Vibrational frequencies were obtained using a cubic fit to the total energies at elongated positions $\Delta d_{\mathrm{O-O}} = 0.0, \pm 0.05, \pm 0.10$ Å and reveal a similar correlation to the binding energy: With increasing spin compensation of the O_2 molecule, i.e., with increasing occupation of the π^* antibonding O_2 orbitals, the O-O bond gets weakened and the vibrational frequency gets more and more reduced from the gas phase value of $\omega = 1567$ cm^{-1}.

Similar to the results of atomic oxygen adsorption, both effects of compressing the Pt(111) surface by 3.2% and interactions with the Ru substrate are clearly separable. In both cases, the compression by 3.2% and the influence of the Ru(0001) on the first Pt monolayer yields roughly the same change in adsorption energies. As shown in Sec. 4.1, both the compression of Pt(111) monolayers and the strong inter-layer bonding between the two metals drastically modifies the distribution of the *d*-band valence states as shown in Fig. 4.4. According to the Hammer-Nørskov model [80, 84, 85], the CO adsorption energy should be directly proportional to the center of the locally projected *d*-band of the surface atom as expressed in Eq. (2.29). In Fig. 4.11, the *d*-band center of the top-layer atom, ε_d, is plotted against the computed binding energies for the O_2^{2-} peroxo and the O_2^- superoxo precursors (see also Table 4.3 and 4.7). Also drawn is the best least-squares linear fit to the O_2^- binding energies on all systems with a Pt top-layer atom. The binding energy of O_2^- on Ru(0001) is somewhat offset from this trend, as might be expected since the coupling matrix element, V_{ad}, is different for pure Ru(0001) and the simple linear relationship of Eq. (2.28) no longer holds quantitatively. Nevertheless, the correct trend for the adsorption of O_2 on the different nPt/Ru(0001) systems is clearly reproduced.

Experimental adsorption energies for O_2 on nPt/Ru(0001) are not available. Initial sticking coefficients were, however, determined recently [16] and are listed in the last column of Table 4.7. Although sticking probabilities are, in principal, determined by properties of the whole potential energy surface (and not just the adsorption well) and thus should be computed using truly dynamical simulations, they can be somewhat crudely related by use of the hard-cube model [60]. A lower adsorption well depth, i.e., lower binding energy then translates to a smaller sticking coefficient, given the same kinetic energy of the incident particle. This trend is obviously reproduced by the experimentally determined sticking coefficients. Nevertheless, for one monolayer of Pt on Ru(0001), no molecular O_2 adsorption could be detected at all ($S_0 = 0.00$). This discrepancy might be due to an activation barrier kinetically hindering a population of the molecular precursor state. On the other hand, DFT calculations using the PW91 exchange-correlation functional are likely overestimating the O_2 binding energies considerably and it might very well be that the determined binding energies for 1Pt/Ru(0001) are actually close to zero.

4.4 CO adsorption

As a final probe molecule for testing the adsorption properties of nPt/Ru(0001), we will examine adsorption of carbon monoxide. CO is known to adsorb in an on-top position on Pt(111) [182, 183]. Due to the fact that only one metal atom is directly involved in the bonding at usually rather large separations and interactions with next-nearest neighbors and subsurface atoms are negligible, on-top adsorption represents one of the most ideal test cases for the *d*-band model. Its validity for CO on-top adsorption is clearly proven [84, 85]. Furthermore, previous work on Pt-Ru surface alloys [146, 184–186] explicitly shows the strong influence of neighboring Ru atoms on the reactivity of Pt.

However, despite its widespread use for CO/Pt calculations [123, 124, 187–189], DFT is known to fail to predict the correct on-top adsorption site for CO on Pt(111) [183] and instead favors the higher coordinated hollow positions by as much as 0.25 eV within the GGA approximation. Whether this error is caused by neglecting relativistic effects [190] or instead induced by the GGA due to the fact that it treats different

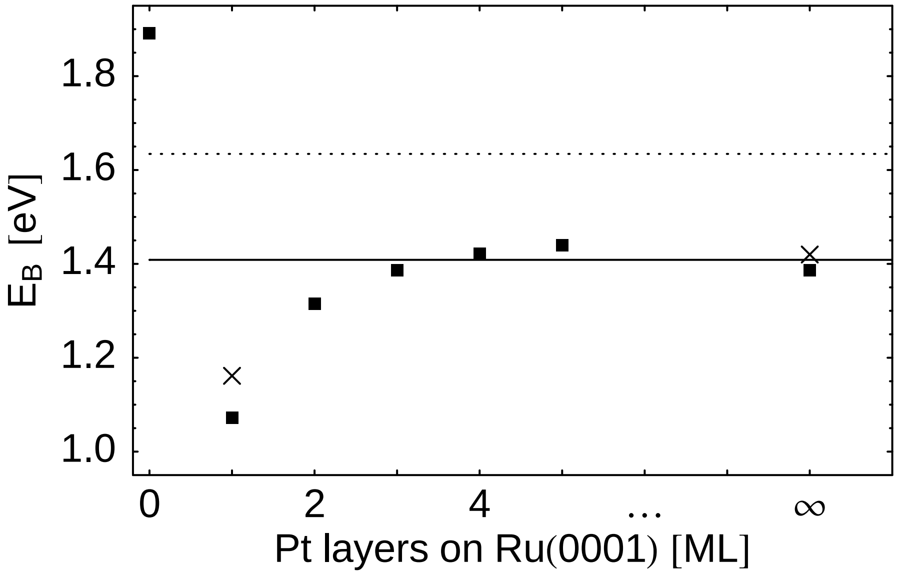

Figure 4.12: On-top CO adsorption energies on nPt/Ru(001), for strained Pt (Ru lattice constant) for a $p(2 \times 2)$-CO (solid box) and a $(\sqrt{3} \times \sqrt{3})$R30° CO overlayer (×). The solid line marks the average adsorption energy for $n \geq 3$. For comparison, the adsorption energy of CO on unstrained Pt(111) is indicated by the dashed line.

bond orders with varying accuracy [191], is not settled yet. To avoid these problems, we fixed the CO molecule to the on-top position in all calculations. By doing so, relative differences between adsorption energies should yield reliable results.

The properties of the CO molecule in the gas phase were already given in Table 3.6 and we refer to Sec. 3.4 for the computational details. The obtained on-top adsorption energies of CO on nPt/Ru(0001) for a $p(2 \times 2)$ overlayer (coverage $\theta_{\mathrm{CO}} = 0.25$) are shown in Fig. 4.12 and summarized in Table 4.8.

For the uncompressed Pt(111) slab, an adsorption energy of 1.63 eV is obtained, in excellent agreement with an adsorption energy of 1.66 eV determined by single crystal adsorption calorimetry for a coverage range of $\theta = 0.17 \ldots 0.33$ [192]. The determined bonding lengths are also in good agreement with LEED measurements ($d_{\mathrm{C-O}} = 1.15$ Å, $d_{\mathrm{C-Pt}} = 1.85$ Å) [182]. Despite the mentioned shortcomings of the GGA approximation, the results for the similar nPt/Ru(0001) should thus be also reliable.

As we have already seen in the previous sections, the effects of the Ru(0001) substrate and the compression of the Pt layers are clearly separable: Within the accuracy of our DFT calculations, adsorption energies have converged to the value obtained on a compressed Pt(111) slab starting with the third Pt layer. Adsorption energies of CO on 1Pt/Ru(0001) and, to a somewhat lower extent, 2Pt/Ru(0001) are found to be clearly lower compared to compressed Pt(111), due to the presence of the underlying Ru(0001) substrate.

According to our calculations the isolated effect on CO adsorption energies of just compressing the Pt(111) surface by 3.2% amounts to 0.24 eV; this value is significantly larger than the energy change reported for CO on a compressed Ru(0001) surface [151] where a 1.5% compression results in a rather small change of about 0.02 eV. An effect of similar size was, however, reported for Pt-Ru [185] or Pt-Co surface alloys [193]. Nevertheless, the influence of the substrate is of equal importance and, for a single Pt layer, clearly exceeds the strain effect in the case of CO adsorption. As seen before, the electronic influence of the underlying substrate decays rapidly with layer thickness and is barely noticeable for $n > 3$.

Comparing the relative changes in binding energies obtained for CO adsorption on 1Pt/Ru(0001) and Pt(111)@Ru in Table 4.8 and for O_2 adsorption in Table 4.7, we note that the relative difference of binding energies is considerably larger for CO adsorption (approximately 0.32 eV) than for O_2 adsorption (0.26 and 0.22 eV). This is in agreement with our expectations that on-top adsorption should be mostly influenced by the top atom only and that any shift of its d-band center should predict a similar change in binding energies: As shown in Fig. 4.13, there is indeed a strong correlation between the d-band center, ε_d, and the adsorption energies, E_b, for Pt layers of variable thickness on Ru(0001). In the case of CO on-top adsorption, subsurface layer interactions are negligible and the predictive quality of the d-band model is even better than for O_2 adsorption.

Experimental results for the Pt/Ru metal layer system are shown in Fig. 4.14: The desorption temperature of CO versus the number of Pt layers is plotted. In contrast to conventional TDS peak temperatures, the desorption temperatures were obtained by monitoring the internal CO stretch mode by infrared absorption spectroscopy (IRAS) and correspond to the temperature where the IR signal vanished. They thus represent the desorption temperature of CO in the dilute limit, excluding any lateral CO-CO

Table 4.8: Adsorption energies and geometries for CO adsorption on nPt/Ru(0001) using both a $p(2 \times 2)$ ($\theta = 0.25$) and a $(\sqrt{3} \times \sqrt{3})$R30° surface unit cell ($\theta = 0.33$). In addition to the binding energies, the bond lengths between carbon and oxygen as well as carbon and the respective metal atom are shown. The last column lists the induced buckling of the top layer, Δz, as the adsorbed CO causes an outward relaxation of its direct bonding partner.

Coverage	Substrate	E_b [eV]	$d_{\mathrm{C-O}}$ [Å]	$d_{\mathrm{C-Me}}$ [Å]	Δz [Å]
$\theta = 0.25$	Ru(0001)	1.89	1.17	1.90	0.13
	1Pt/Ru(0001)	1.07	1.16	1.89	0.21
	2Pt/Ru(0001)	1.31	1.16	1.86	0.19
	3Pt/Ru(0001)	1.39	1.16	1.85	0.19
	4Pt/Ru(0001)	1.42	1.16	1.85	0.18
	5Pt/Ru(0001)	1.44	1.16	1.85	0.20
	Pt(111)@Ru	1.39	1.16	1.85	0.23
	Pt(111)	1.63	1.16	1.85	0.24
$\theta = 0.33$	1Pt/Ru(0001)	1.16	1.16	1.89	0.21
	Pt(111)@Ru	1.42	1.16	1.85	0.24
	Pt(111)	1.62	1.16	1.85	0.23

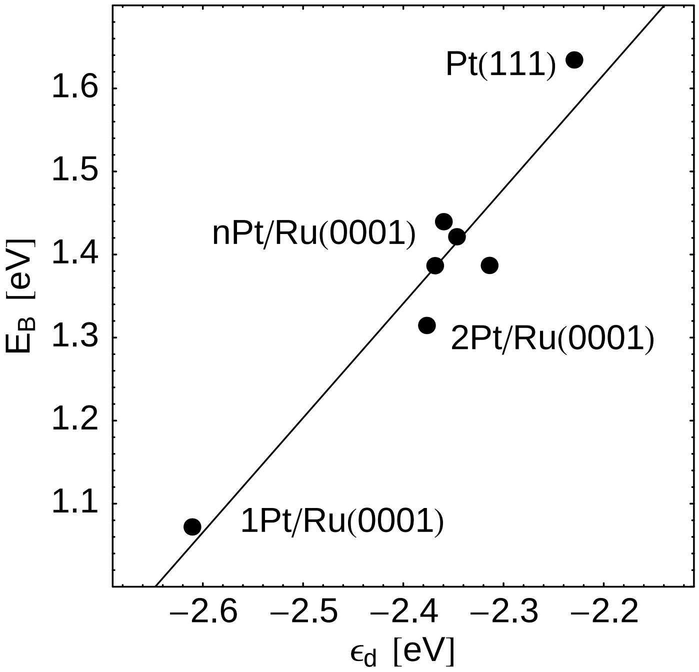

Figure 4.13: CO adsorption energy versus d-band center (with respect to the Fermi energy) of the surface Pt atom for a $p(2 \times 2)$ ordered overlayer. The solid line represents the best least-squares linear fit.

interactions [16, 153]. Assuming a pre-factor for desorption of $k_0 = 10^{15}$ s^{-1}, binding energies of 0.99 eV, 1.21 eV, and about 1.30 – 1.35 eV for the first, second and higher layers can be derived, respectively.

The trend in binding energies is thus clearly reproduced. Nevertheless, the pure strain effect on E_b seems to be slightly less for the experimental data in comparison to the theoretical results. This could be attributed to dissimilar coverages in the experiment (dilute layer) and in our theoretical calculation [$p(2 \times 2)$ supercell]. At least for a coverage of $\theta = 0.5$, the formation of the $c(4 \times 2)$ CO adlayer is substantially influenced by dipole-dipole and indirect interactions [194]. We thus checked CO binding energies for selected slabs at a coverage of $\theta = 0.33$ in a $(\sqrt{3} \times \sqrt{3})$R30° geometry (using $4 \times 4 \times 1$ **k** points). The results are included in Table 4.8 and Fig. 4.12. As can be seen, there are indeed subtle coverage effects, but they are too small to account for the discrepancy to the experimental data.

The observed deviation might also be explained by the fact that the equilibrium lattice constants of Pt and Ru computed within DFT overestimate the experimentally observed lattice mismatch by 25%. This might also slightly distort the reported DFT results. Nevertheless, considering these facts, the agreement between theory and experiment is very good.

Summarizing the results of this chapter, we have clearly demonstrated that two major effects can be identified for the adsorption on nPt/Ru(0001): First, due to the lattice mismatch between Ru and Pt, the Pt layers are compressed and this already

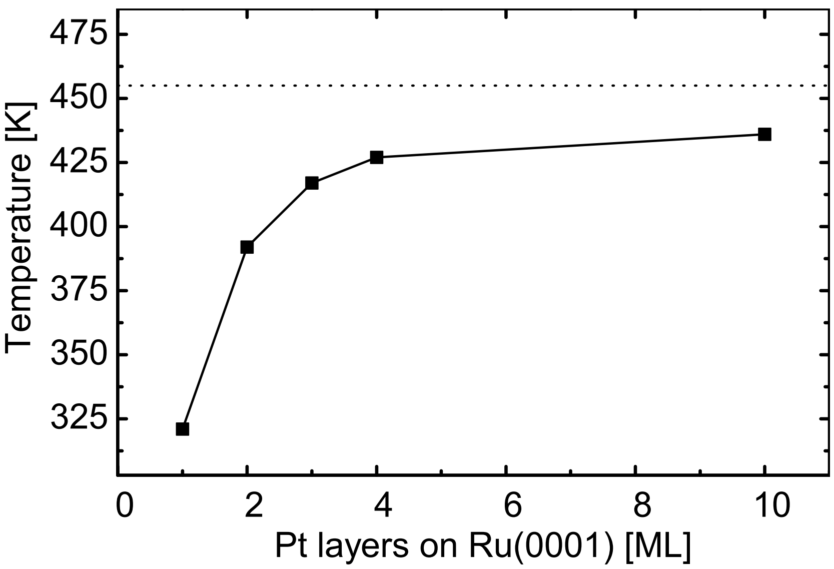

Figure 4.14: Desorption temperatures of CO (small coverage) on Pt layers on Ru(0001) from IR spectroscopy and TPD. The dashed line indicates the desorption temperature of small amounts of CO from the unstrained Pt(111) surface [16, 153].

significantly reduces the reactivity of the surface. And second, the underlying Ru substrate rather strongly binds the first Pt overlayer grown on top of it and thus modifies the chemical properties of the overlayer. The effect of the Ru substrate is still very noticeable on the second overlayer, but starting with the third layer vanishes. Adsorption of atomic oxygen, molecular oxygen and carbon monoxide all followed this trend, and the relative changes of the binding energy are clearly correlated with the respective *d*-band centers as explained by the *d*-band model.

Chapter 5

Conclusions

We have studied adsorption of simple molecules on structured surfaces. Our focus was on two different systems, namely adsorption on Pd(210) and on nPt/Ru(0001).

In Chapter 3, we have presented DFT calculations for adsorption of hydrogen and carbon monoxide on Pd(210). Layer relaxations of this open surface have been found to be significant, but are considerably reduced by the presence of hydrogen either on the surface or in subsurface positions. This suggests that the surprisingly small layer relaxations of Pd(210) found in the experiment [110] might be caused by subsurface hydrogen which is hard to detect in the experiment.

We have examined and identified the hydrogen atomic adsorption sites for coverages of up to $\theta = 3$ per surface unit cell. It was found that the energetic ordering of the adsorption sites does not follow the simple coordination argument that the most favorable sites are those with the highest coordination of the adsorbate. Instead, the atom-surface bonds were analyzed within the Hammer-Nørskov d-band model. The lower coordination of the surface atoms at the kinked steps of the Pd(210) surface leads to a local d-band shift that correlates well with the hydrogen adsorption energies and thus accounts correctly for the high reactivity of the step-like top-layer Pd atom.

Furthermore, we have identified a molecular chemisorption state of H_2 on Pd(210) with a binding energy of 0.27 eV. Such states do not exist on flat metal surfaces. At Pd(210) steps, the molecular state is stabilized by the presence of atomic hydrogen at the surface. A hydrogen pre-coverage is necessary as otherwise non-activated pathways for dissociative hydrogen adsorption exists. Pre-adsorbed atomic hydrogen does not significantly disturb the interaction of the H_2 molecules with the Pd atoms as long as the H_2 molecules are further away from the surface, but it locally hinders the H_2 dissociation on Pd(210) although atomic adsorption sites are still available.

Variations in the adsorption energy of carbon monoxide were found to be rather small. At the most favorable bridge site, CO adsorbs inclined with respect to the surface normal and the bonding process is dominated by its local bonding partners. Coadsorption of hydrogen is largely inhibited with CO present on the surface, due to the strong interaction of CO with the Pd surface atoms.

Pd(210) represents a rather open, stepped surface, and variations of each surface atom's reactivity are due to the surface's specific geometry. On the other hand, the system nPt/Ru(0001) studied in Chapter 4 represents a rather uniform, close-packed surface. In this case, the interesting variations of the local reactivity are due to a compression of the Pt overlayers and residual interactions with the ruthenium substrate.

We first determined the layer structure of pseudomorphically grown platinum overlayers on a Ru(0001) substrate. The film thickness was varied from one to five layers, and it was found that there is a very strong interaction of a single Pt monolayer with the Ru substrate. For films with three or more layers, residual interactions with the Ru substrate were no longer discernible and any changes in the surface reactivity compared to a pure Pt(111) surface are thus only caused by the strain on the Pt overlayers.

We then determined adsorption properties of atomic and molecular oxygen as well as carbon monoxide on nPt/Ru(0001) and compared them to experimental data [15, 16]. The respective binding energies all follow the same trend, and allow for a disentanglement of the two intrinsic effects modifying the reactivity of heteroepitaxial metal layers, namely the lattice strain within the grown film and the electronic interaction of the film with the underlying substrate. In the case of nPt/Ru(0001), the compression of the Pt overlayers to match the smaller lattice constant of ruthenium significantly reduces the reactivity of the surface with respect to adsorption of O, O_2, and CO. The strong binding of a single Pt monolayer to the Ru substrate leads to an even further reduced reactivity, and this effect is still noticeable for two Pt overlayers. Starting with the third overlayer, the effect of the Ru substrate on the surface reactivity vanishes.

Finally, the adsorption of oxygen and carbon monoxide were analyzed in terms of the d-band model. The shifts in the d-band centers of the surface layer atoms were found to be clearly correlated with the computed binding energies as predicted by the model. The shift in the d-band center towards lower energies is both due to the layer compression and the substrate interaction.

In both cases of adsorption on Pd(210) and nPt/Ru(0001), we have seen that variations of the chemical reactivity are significant and correlated to the center of the local d-band states. The change in chemical reactivity is caused by defects, steps, lateral strain, or substrate interactions. This interplay of geometrical and electronic effects exhibits unique features, such as the stabilization of the H_2 molecular state on Pd(210), that might be useful for catalyzing certain reactions. By studying structured surfaces in more detail one might thus discover specific sites with special chemical properties and adjust the chemical reactivity as needed for catalyzing a given reaction.

Nevertheless, both surfaces we looked at are still far away from any realistic description of or direct application to the processes in a real world catalytic reaction. But as Walter Kohn phrased it in a review about condensed matter physics in the twentieth century:

> *A final remark about surface science and surface technology. The former, both in the laboratory and in the theorist's thinking, deals mostly with as perfect systems as possible. On the other hand, in technological applications surfaces are generally very imperfect, both structurally and chemically.*

> *Nevertheless, concepts developed by idealized surface science have been very important guides for practical applications.* [195]

It is in this sense that we hope to have contributed a small piece of the big question of what principles are governing chemical reactions at surfaces, and how they might be applied to develop better catalysts one day.

Appendix A

Numerical accuracy of DFT calculations

When performing density-functional theory calculations, a couple of approximations are invoked to actually make the problem tractable. The most important approximation in this context is the use of a suitable exchange-correlation functional as outlined in Sec. 2.1.2. However, the use of a specific exchange-correlation functional is in some sense also the approximation with the most unvavorable property: It cannot be controlled in a systematic way, as we do neither know the exact functional, nor a small-paramater Taylor expansion of it. On the other hand, all other approximations necessary for a numerical treatment of the Kohn-Sham equations and described in Sec. 2.1, can be checked against their convergence and transferability. In the following, we will shortly summarize how the numerical accuracy of the calculations presented in Chapters 3 and 4 depend on the chosen set of parameters.

Energy cut-off convergence

Numerically, the most important parameter for the accuracy, but also for the computational speed and memory requirements of the calculation is the chosen energy cut-off. In a straightforward implementation, the Hamiltonian matrix of Eq. 2.17 is of size $O(N^2)$, and solving it would require $O(N^3)$ time steps, where N is the number of plane waves used. By using iterative algorithms, both size and computation time can be reduced dramatically.

The number of plane waves used to represent the all-electron wave function is determined by Eq. 2.15,

$$E_{\mathrm{cutoff}} = \frac{\hbar^2}{2m} \left|\mathbf{k} + \mathbf{G}\right|^2 , \tag{A.1}$$

for each $\mathbf{k}$ point. When using ultrasoft pseudopotentials, an energy cut-off of 200 eV is usually sufficient to achieve convergence. For PAW pseudopotentials, the cut-off typically has to be chosen slightly larger.

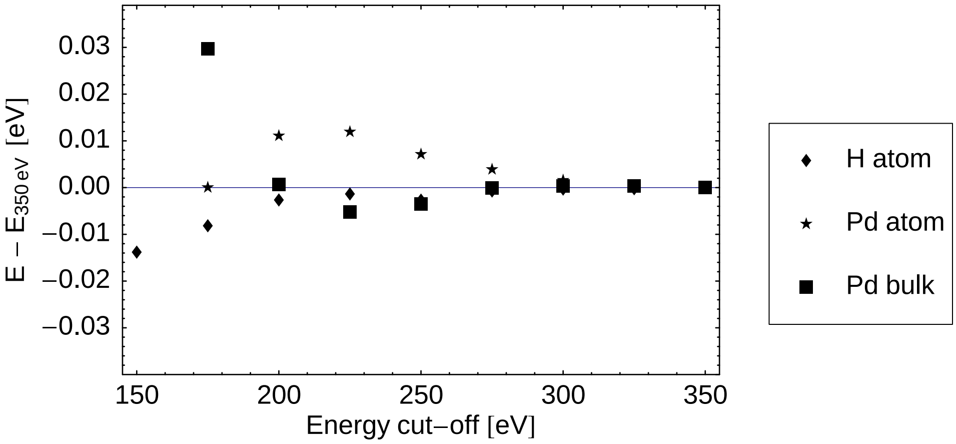

Figure A.1: Convergence of total energy with respect to plane wave energy cut-off for isolated hydrogen and atomic as well as bulk palladium. Ultrasoft pseudopotentials as supplied with VASP were employed [55, 56].

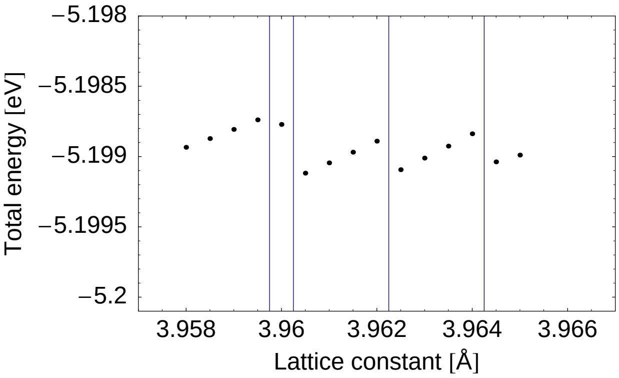

Figure A.2: Numerical errors due to basic set incompleteness: Volume changes induce small errors in the total energy. The shown variations of the DFT total energy are for a Pd bulk crystal computed with its primitive unit cell.

The dependence of the total energy on the plane wave energy cut-off is shown in Fig. A.1 for atomic palladium, bulk palladium and atomic hydrogen. In all three cases, the total energy is drawn with reference to the respective total energy at a very large energy cut-off of 350 eV. It can be seen that, starting at $E_{\text{cutoff}} = 200$ eV, the numerical error of the total energy is less than 0.01 eV. Furthermore, convergence of relative energy differences, e.g., of different bulk phases or a molecule in the gas phase and adsorbed on the surface, is much faster. The energy differences of different bulk palladium structures are, for instance, already converged to less than 15 meV for a rather low cut-off energy of 150 eV.

It was thus found to be sufficient to use an energy cut-off of 200 eV for all calculations of the H/Pd system in Chapter 3. In all other calculations where oxygen was present, the energy cut-off had to be increased to 400 eV to accurately represent the rather hard oxygen core.

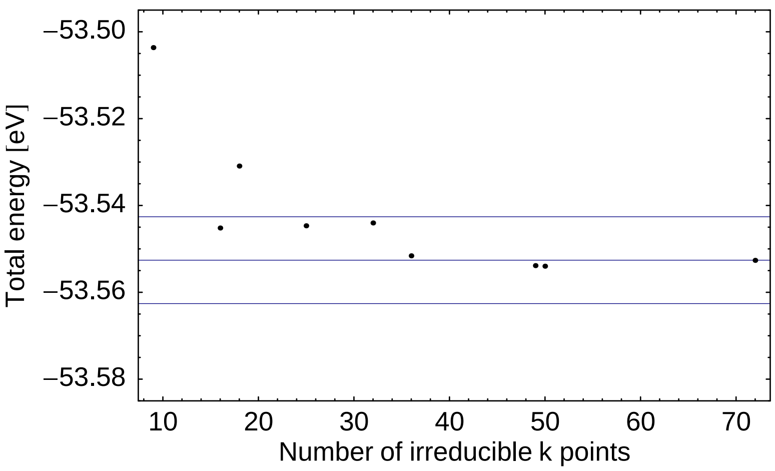

Figure A.3: Convergence of total energy with respect to the number of **k** points in the irreducible Brillouin zone for a $p(1 \times 1)$ Pd(210) slab.

When choosing a certain energy cut-off, the size of the finite plane wave basis set is given by Eq. 2.15. The discrete number of plane waves, however, fitting in the sphere determined by this equation changes with the volume of the unit cell. The number of plane waves thus changes discontinuously when changing the volume. This effect has to be taken into account for calculation involving supercells of various volume, such as the determination of the bulk lattice constant. For bulk palladium, the variations of the total energy with respect to the lattice constant, i.e., the volume of the primitive unit cell, are shown in Fig. A.2. Discrete jumps in the number of plane waves are indicated by vertical lines. As can be seen in Fig. A.2, the error in the total energy is smaller than 1 meV and thus can be safely ignored when using a fitting procedure to determine the bulk lattice constant as described in Sec. 2.2.1.

k-point mesh

When computing any expectation value and using a plane wave basis set, the necessary integration of the Brillouin zone has to be replaced by a finite sum over special **k** points. For a molecule in a large supercell, only one **k** point (at the Γ point of the reciprocal cell) is necessary. For a bulk or slab calculation, however, any direction with a significant band dispersion has to be computed using a finite mesh of **k** points. For a slab setup with interspersing vacuum in the z direction, there is no significant band dispersion in this direction and it is sufficient to use one 1 **k** point. For the x and y directions in the surface plane, a finite **k** point mesh has to be determined which accurately reflects the bulk band structure of the respective metal. In this work, only Monkhorst-Pack **k** point sets were used.

The number of **k** points at which the wave function has to be computed can be significantly reduced by exploiting any symmetry of the supercell. For example, in the case of a $p(1 \times 1)$ Pd(210) slab with its inherent C_{2h} symmetry, a $7 \times 7 \times 1$ Monkhorst-Pack mesh is reduced to 16 **k** points in the irreducible Brillouin zone, a $11 \times 11 \times 1$

mesh to 36 **k** points. The convergence of the total energy with respect to the number of **k** points in the irreducible Brillouin zone is illustrated in Fig. A.3 for an 11-layer Pd(210) slab. It can be seen that the total energy of the whole slab (including 11 atoms) is converged to its final value with an accuracy of 10 meV for a $7 \times 7 \times 1$ **k** point mesh.

Smearing

To speed up the convergence of the total energy with respect to the number of **k** points, it is customary to artificially "smear" out the occupancy of each **k** point and thus get a smooth transition from occupation 1 to occupation 0 at the Fermi level. This can also be regarded as computing the total energy for an electronic distribution at some finite temperature. Avoiding the sharp transition greatly reduces the number of necessary **k** points. Broadening of the electronic states can be obtained by applying a Fermi-Dirac function, a Gaussian function or an improved functional as proposed by Methfessel and Paxton [40]. In this work, only Methfessel-Paxton smearing of order $N = 1$ and a smearing parameter of $\sigma = 0.1$ eV (Pd) or $\sigma = 0.2$ eV (Pt/Ru) is employed.

The use of a broadening approach, however, leads to the situation that the computed DFT total energy is no longer the true ground state energy, but some free energy at a finite "temperature". It is thus necessary to correct the computed total energy and perform an extrapolation for $\sigma \to 0$. For a smearing width of 0.1 eV, the correction per atom is usually on the order of 1 meV. All reported total energies in this work have been extrapolated to $\sigma = 0$ eV.

Although σ should be chosen as large as possible to speed up **k** point convergence and the induced error can be corrected, it has to be noted that this is not true for any computed forces: Forces within VASP are computed as derivatives of the free energy at finite σ and are thus sensitive to increasing σ [43]. Furthermore, for large σ, the energy minimum of $E(\sigma \to 0)$ might deviate from the ground state obtained by a geometry relaxation according to the computed forces. In this respect, it is thus desirable to use a small enough smearing parameter σ. For the smearing parameters chosen in this work, the resulting error is however negligible.

Wave function projectors

For both ultrasoft and PAW pseudopotentials [45, 46, 58], the non-local part of the pseudopotential requires the evaluation of a projection operator on the pseudized wave function. This projection can be either evaluated in reciprocal or real space. In reciprocal space, the projection can be easily done involving all Fourier components of the wave function and thus accurately, and no further approximation is applied. The drawback is that this approach scales with the total number of plane waves. For large-scale simulations involving more than a dozen atoms, this projection can thus become rather expensive. All calculations using ultrasoft pseudopotentials in this work were done using reciprocal space projections.

On the other hand, the projection in real space can be confined locally to spheres around each atom. Therefore, the number of necessary operations to compute one

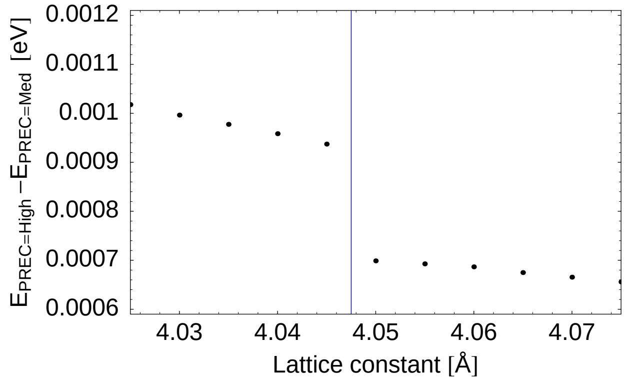

Figure A.4: Numerical errors due to coarser finite FFT grids: The difference in total energy between an exact FFT mesh and an FFT mesh reduced by 25% is plotted. The shown variations of the DFT total energy are for a Pd bulk crystal computed with its primitive unit cell. Volume changes are again causing sudden jumps in the relative energy difference.

projection does not increase with the system size. By computing the projection only within a cut-off sphere around each ion, additional errors in the total energy are introduced based on the size of the sphere. Furthermore, special care has to be taken to avoid any spurious high frequency components in the projection operators that would be aliased to low frequency components. For all large-scale PAW calculations, we have used the real space projection scheme: The projection operators were configured to be optimized automatically (by VASP) such that the absolute error per atom was smaller than 0.5 meV in comparison with the exact reciprocal space projectors.

Errors due to FFT mesh

For a computation of the local potential when evaluating Eq. 2.17, a Fourier transform of the wave function is needed. For an exact calculation, the discrete FFT mesh must contain all wave vectors up to $2G_{\text{cutoff}}$ with $E_{\text{cutoff}} = \frac{\hbar^2}{2m} G_{\text{cutoff}}^2$ [43]. Usually, the size of the FFT mesh can safely be reduced to $\frac{3}{4}$ of the required values. As shown in Fig. A.4, the numerical error is below 1 meV for bulk palladium.

However, the computation of forces is much more sensitive with regard to any wrap-around errors caused by too small an FFT mesh. To avoid any numerical errors, we have always used accurate FFT meshes to compute the final adsorption geometries and total energies. Only for pre-relaxations and potential energy surfaces, FFT meshes reduced to $\frac{3}{4}$ of the exact values were employed.

Potential energy surface

Potential energy surfaces of an approaching molecule as shown in Figs. 3.10 and 3.11 were computed using a finite set of grid points in the respective section of the potential energy. Usually, around 60 to 100 grid points were used: Bond distances were scanned in steps of 0.2 Å, and center-of-mass distances to the surface in steps of 0.5 Å.

These rather coarse grid was possible by interpolating the potential energy surface

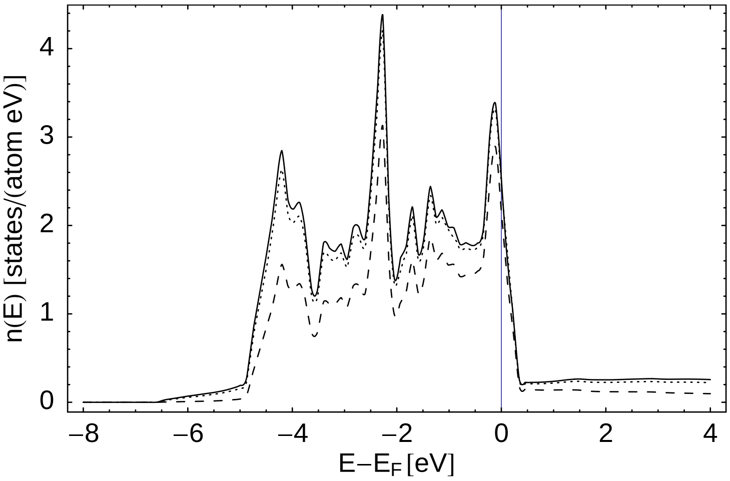

Figure A.5: Influence of the projection radius on the local density of states: Shown is the total density of states of bulk Pd. The solid curve represents the true total density of states obtained with the GGA approximation in the full primitive unit cell. The dotted and dashed curves are the total density of states obtained by truncating the wave function to a sphere of radius $r = 1.54788$ Å (Wigner-Seitz radius) and $r = 1.0$ Å, respectively.

using both the total energy and the computed forces on the atoms at each grid point. Any evaluation of the potential energy surface on this finite grid was then done using a cubic polynomial interpolation between adjacent grid points constructed using the total energies and the respective derivatives. It has to be noted that no fitting procedure was used, but the output of the DFT computations including the forces was instead used as an exact input for the interpolation.

Local density of states

The local density of states (LDOS) as discussed in Sec. 2.2.5 is not directly accesible in any DFT calculations using plane waves: Due to the use of delocalized plane waves for the representation of the wave function, there is neither an orbital nor a site-specific, local decomposition available.

To work around this, the local density of states is obtained using an additional projection scheme. First, the wave function is truncated at a sphere of a given radius, e.g., the Wigner-Seitz radius, around the atom of interest. Outside this sphere, the wave function is set to zero. Within the sphere, the wave function is then decomposed by projecting it onto spherical harmonics to obtain the angular momentum resolved wave function expansion. Using these coefficients, it is straighforward to construct the orbital-resolved, local density of states at each ion [196]. For consistency, the DOS spectrum was computed using the same smearing parameters as employed in the Brillouin zone integration and described above throughout this work.

The drawback of this approach is its ambiguity with respect to the projection radius: The choice of the projection radius is somewhat arbitrary, and no “ideal” radius exists. Choosing too large a radius implies that regions of overlapping spheres are double-counted for two neighboring atoms when adding up the LDOS; choosing too small a radius, on the other hand, means loosing any relevant components in the interstitial, bonding regions. A reasonable choice for bulk materials is the Wigner-Seitz radius, at least preserving the total volume of the original and the projected space. For atoms or molecules, an easy choice does not exist and we use 1.058 Å = 2 bohr by convention.

The influence of the projection radius on the obtained local density of states is depicted in Fig. A.5 for bulk palladium. The solid line shows the total density of states of bulk Pd directly obtained from the GGA ground state wave function and its energy spectrum. The dotted line represents the total density of states of the same calculation, but obtained via the projection scheme described above using the Wigner-Seitz radius of $r = 1.547888$ Å and summing up the s, p, d-projected LDOS. Although the two curves are rather similar, the differences are noticeable and an integration of the DOS obtained by the inaccurate projection scheme, for example, would yield a higher Fermi level. Reducing the projection radius to 1.0 Å gives the dashed curve: The number of states accounted for in the LDOS is of course reduced by shrinking the projection sphere, but unfortunately, it is not just an overall uniform scaling of the DOS. When comparing LDOS spectra of different calculations, it is thus essential to use the same projection radius for all calculations.

Within the d-band model (cf. Sec. 2.2.5), the center of the d-band comprises all the effects of the d-band orbitals on the interaction with an atom or molecule. However, the determination of this d-band center is numerically not unique: As can be seen from Fig. A.5, a change in the projection radius can also cause a significant skew in the DOS distribution and thus change its center. For the d-band center of bulk palladium, switching from the Wigner-Seitz radius to a radius about $\frac{2}{3}$ smaller, $r = 1.0$ Å, shifts the d-band center by approximately 0.15 eV closer to the Fermi level. Furthermore, the integrals of Eq. 2.27 should be carried out from $-\infty$ to ∞. In practice, however, the unoccupied DFT eigenstates above the Fermi level are not well-defined and often pick up rather significant numerical “noise” when projected. In the case of Pd, the integrations were indeed performed over the whole energy range available. For the Pt/Ru systems in Ch. 4, however, the integration is truncated approximately at the upper d-band edge as numerical errors for energies high above the Fermi level would distort the reported results. Considering these effects, comparison of LDOS results of different computations have to be done with care.

Appendix B

Computer resources

The computations of this work have been performed on a few different computers. Most of the basic work was done on the Linux workstations of the T30g group, i.e., either AMD Athlon XP or Compaq Alpha machines. Large-scale simulations with excessive memory requirements were computed on either the Fujitsu VPP700/52 or the MPI-Linux cluster (Intel Pentium III/4 machines) of the Leibniz-Rechenzentrum (LRZ) within the t2101 project.

All DFT calculations were carried out using the Vienna *ab initio* simulation package (VASP), mainly developed by J. Furthmüller and G. Kresse [43]. Versions "4.4.4 10Jun99" through "4.4.5 26Nov01" of VASP, in both serial and parallel mode, were employed together with the officially released database of ultrasoft or PAW pseudopotentials. Depending on the machine type, the platform-specific BLAS libraries (Compaq BLAS 3.6 or ATLAS 3.2.1 libraries) were used for linear algebra support. Analysis and evaluation of the computational results were performed using Perl or *Mathematica* [197] support tools.

Bibliography

[1] Roald Hoffmann. A chemical and theoretical way to look at bonding on surfaces. *Rev. Mod. Phys.*, 60(3):601–628, 1988.

[2] Axel Groß. The virtual chemistry lab for reactions at surfaces: Is it possible? Will it be useful? *Surf. Sci.*, 500:347–367, 2002.

[3] Francisco Zaera. Probing catalytic reactions at surfaces. *Prog. Surf. Sci.*, 69: 1–98, 2001.

[4] Charles E. Mortimer. *Chemie: Das Basiswissen der Chemie.* Thieme, 1987.

[5] Andrew Zangwill. *Physics at Surfaces.* Cambridge University Press, 1988.

[6] M. Bauer, C. Lei, J. Read, R. Tobey, J. Gland, M. M. Murnane, and H. C. Kapteyn. Direct observation of surface chemistry using ultrafast soft-x-ray pulses. *Phys. Rev. Lett.*, 87(2):025501, 2001.

[7] J. R. Hahn and W. Ho. Oxidation of a single carbon monoxide molecule manipulated and induced with a scanning tunneling microscope. *Phys. Rev. Lett.*, 87 (16):166102, 2001.

[8] Stefan Goedecker. Linear scaling electronic structure methods. *Rev. Mod. Phys.*, 71(4):1085–1123, 1999.

[9] D. M. Ceperley. Microscopic simulations in physics. *Rev. Mod. Phys.*, 71(2): S438–S443, 1999.

[10] G. H. Jóhannesson, T. Bligaard, A. V. Ruban, H. L. Skriver, K. W. Jacobsen, and J. K. Nørskov. Combined electronic structure and evolutionary search approach to materials design. *Phys. Rev. Lett.*, 88(25):255506, 2002.

[11] Thomas H. Rod and Jens K. Nørskov. Modeling the nitrogenase FeMo cofactor. *J. Am. Chem. Soc.*, 122(51):12751–12763, 2000.

[12] B. Hammer. Bond activation at monatomic steps: NO dissociation at corrugated Ru(0001). *Phys. Rev. Lett.*, 83(18):3681–3684, 1999.

[13] Uwe Muschiol, Pia K. Schmidt, and Klaus Christmann. Adsorption and absorption of hydrogen on a palladium (210) surface: a combined LEED, TDS, $\Delta\Phi$ and HREELS study. *Surf. Sci.*, 395:182–204, 1998.

[14] Pia K. Schmidt, Klaus Christmann, Georg Kresse, Jürgen Hafner, Markus Lis-

chka, and Axel Groß. Coexistence of atomic and molecular chemisorption states: H_2/Pd(210). *Phys. Rev. Lett.*, 87:096103, 2001.

[15] A. Schlapka, U. Käsberger, D. Menzel, and P. Jakob. Vibrational spectroscopy of CO used as a local probe to study the surface morphology of Pt on Ru(001) in the submonolayer regime. *Surf. Sci.*, 502–503:129–135, 2002.

[16] Andreas Schlapka. *Adsorption von CO und O_2 auf Pt/Ru(001) Bimetalloberflächen.* PhD thesis, Technische Universität München, 2002.

[17] W. Kohn. Nobel lecture: Electronic structure of matter—wave functions and density functionals. *Rev. Mod. Phys.*, 71(5):1253–1266, 1999.

[18] John A. Pople. Nobel lecture: Quantum chemical models. *Rev. Mod. Phys.*, 71 (5):1267–1274, 1999.

[19] P. Hohenberg and W. Kohn. Inhomogeneous electron gas. *Phys. Rev.*, 136(3B): B864–B871, 1964.

[20] G. P. Brivio and M. I. Trioni. The adiabatic molecule-metal surface interaction: theoretical approaches. *Rev. Mod. Phys.*, 71(1):231–265, 1999.

[21] Stefano Baroni, Stefano de Gironcoli, Andrea Dal Corso, and Paolo Giannozzi. Phonons and related crystal properties from density-functional perturbation theory. *Rev. Mod. Phys.*, 73:515–562, 2001.

[22] D. Alfé, G. Kresse, and M. J. Gillan. Structure and dynamics of liquid iron under Earth's core conditions. *Phys. Rev. B*, 61(1):132–142, 2000.

[23] W. M. C. Foulkes, L. Mitas, R. J. Needs, and G. Rajagopal. Quantum Monte Carlo simulations of solids. *Rev. Mod. Phys.*, 73(1):33–83, 2001.

[24] Reiner M. Dreizler and Eberhard K. U. Gross. *Density Functional Theory: An Approach to the Quantum Many-Body Problem.* Springer, 1990.

[25] M. Born and J. R. Oppenheimer. Über die Theorie der Molekeln. *Ann. Phys.*, 84:457, 1927.

[26] W. Kohn and L. J. Sham. Self-consistent equations including exchange and correlation effects. *Phys. Rev.*, 140(4A):A1133–A1138, 1965.

[27] D. D. Johnson. Modified Broyden's method for accelerating convergence in self-consistent calculations. *Phys. Rev. B*, 38(18):12807–12813, 1988.

[28] R. O. Jones and O. Gunnarsson. The density functional formalism, its applications and prospects. *Rev. Mod. Phys.*, 61(3):689–746, 1989.

[29] D. M. Ceperley and B. J. Alder. Ground state of the electron gas by a stochastic method. *Phys. Rev. Lett.*, 45:566–569, 1980.

[30] Aron J. Cohen and Nicholas C. Handy. Assessment of exchange correlation functionals. *Chem. Phys. Lett.*, 316:160–166, 2000.

[31] B. Hammer, M. Scheffler, K. W. Jacobsen, and J. K. Nørskov. Multidimensional potential energy surface for H_2 dissociation over Cu(111). *Phys. Rev. Lett.*, 73: 1400–1403, 1994.

[32] Stefan Kurth, John P. Perdew, and Peter Blaha. Molecular and solid-state tests of density functional approximations: LSD, GGAs, and meta-GGAs. *Int. J. Quant. Chem.*, 75:889–909, 1999.

[33] John P. Perdew, J. A. Chevary, S. H. Vosko, Koblar A. Jackson, Mark R. Pederson, D. J. Singh, and Carlos Fiolhais. Atoms, molecules, solids, and surfaces: Applications of the generalized gradient approximation for exchange and correlation. *Phys. Rev. B*, 46(11):6671–6687, 1992.

[34] John P. Perdew, Kieron Burke, and Matthias Ernzerhof. Generalized gradient approximation made simple. *Phys. Rev. Lett.*, 77(18):3865–3868, 1996.

[35] B. Hammer, L. B. Hansen, and J. K. Nørskov. Improved adsorption energetics within density-functional theory using revised Perdew-Burke-Ernzerhof functionals. *Phys. Rev. B*, 59(11):7413–7421, 1999.

[36] John P. Perdew, Stefan Kurth, Aleš Zupan, and Peter Blaha. Accurate density functional with correct formal properties: A step beyond the generalized gradient approximation. *Phys. Rev. Lett.*, 82(12):2544–2547, 1999.

[37] John P. Perdew, Stefan Kurth, Aleš Zupan, and Peter Blaha. Erratum: Accurate density functional with correct formal properties: A step beyond the generalized gradient approximation. *Phys. Rev. Lett.*, 82(25):5179(E), 1999.

[38] Thomas L. Beck. Real-space mesh technique in density-functional theory. *Rev. Mod. Phys.*, 72(4):1041–1080, 2000.

[39] Hendrik J. Monkhorst and James D. Pack. Special points for Brillouin-zone integrations. *Phys. Rev. B*, 13(12):5188–5192, 1976.

[40] M. Methfessel and A. T. Paxton. High-precision sampling for Brillouin-zone integration in metals. *Phys. Rev. B*, 40(6):3616–3621, 1989.

[41] Peter E. Blöchl, O. Jepsen, and O. K. Andersen. Improved tetrahedron method for Brillouin-zone integration. *Phys. Rev. B*, 49(23):16223–16233, 1994.

[42] M. C. Payne, M. P. Teter, D. C. Allan, T. A. Arias, and J. D. Joannopoulos. Iterative minimization techniques for ab initio total-energy calculations: molecular dynamics and conjugate gradients. *Rev. Mod. Phys.*, 64(4):1045–1097, 1992.

[43] Georg Kresse and Jürgen Furthmüller. *Vienna Ab-initio Simulation Package. VASP the Guide*. Institut für Materialphysik, Universität Wien, March 2001. http://cms.mpi.univie.ac.at/vasp/.

[44] G. Kresse and J. Hafner. Ab initio molecular dynamics for liquid metals. *Phys. Rev. B*, 47(1):558–561, 1993.

[45] G. Kresse and J. Furthmüller. Efficient iterative schemes for ab initio total-energy calculations using a plane-wave basis set. *Phys. Rev. B*, 54(16):11169–11186, 1996.

[46] G. Kresse and J. Furthmüller. Efficiency of ab-initio total energy calculations for metals and semiconductors using a plane-wave basis set. *Comput. Mater. Sci.*, 6:15–50, 1996.

[47] Matthias Scheffler, Jean Pol Vigneron, and Giovanni B. Bachelet. Total-energy gradients and lattice distortions at point defects in semiconductors. *Phys. Rev. B*, 31(10):6541–6551, 1985.

[48] O. Krogh Andersen. Linear methods in band theory. *Phys. Rev. B*, 12(8):3060–3083, 1975.

[49] U. von Barth and C. D. Gelatt. Validity of the frozen-core approximation and pseudopotential theory for cohesive energy calculations. *Phys. Rev. B*, 21(6): 2222–2228, 1980.

[50] N. Troullier and José Luís Martins. Efficient pseudopotentials for plane-wave calculations. *Phys. Rev. B*, 43(3):1993–2006, 1991.

[51] Andrew M. Rappe, Karin M. Rabe, Efthimios Kaxiras, and J. D. Joannopoulos. Optimized pseudopotentials. *Phys. Rev. B*, 41(2):1227–1230, 1990.

[52] David Vanderbilt. Soft self-consistent pseudopotentials in a generalized eigenvalue formalism. *Phys. Rev. B*, 41(11):7892–7895, 1990.

[53] Alfredo Pasquarello, Kari Laasonen, Roberto Car, Changyol Lee, and David Vanderbilt. Ab initio molecular dynamics for d-electron systems: Liquid copper at 1500 K. *Phys. Rev. Lett.*, 69(13):1982–1985, 1992.

[54] Kari Laasonen, Alfredo Pasquarello, Roberto Car, Changyol Lee, and David Vanderbilt. Car-parrinello molecular dynamics with vanderbilt ultrasoft pseudopotentials. *Phys. Rev. B*, 47(16):10142–10153, 1993.

[55] G. Kresse and J. Hafner. Norm-conserving and ultrasoft pseudopotentials for the first-row and transition elements. *J. Phys.: Condens. Matter*, 6:8245–8257, 1994.

[56] J. Furthmüller, P. Käckell, F. Bechstedt, and G. Kresse. Extreme softening of vanderbilt pseudopotentials: General rules and case studies of first-row and *d*-electron elements. *Phys. Rev. B*, 61:4576–4587, 2000.

[57] P. E. Blöchl. Projector augmented-wave method. *Phys. Rev. B*, 50(24):17953–17979, 1994.

[58] G. Kresse and D. Joubert. From ultrasoft pseudopotentials to the projector augmented-wave method. *Phys. Rev. B*, 59(3):1758–1775, 1999.

[59] M. Fuchs, M. Bockstedte, E. Pehlke, and M. Scheffler. Pseudopotential study of binding properties of solids within generalized gradient approximations: The role of core-valence exchange correlation. *Phys. Rev. B*, 57(4):2134–2145, 1998.

[60] Axel Groß. *Theoretical Surface Science: A Microscopic Perspective.* Springer, 2002.

[61] F. D. Murnaghan. The compressibility of media under extreme pressure. *Proc. Nat. Acad. Sci. USA*, 30:244–247, 1944.

[62] Francis Birch. Finite strain isotherm and velocities for single-crystal and polycrystalline NaCl at high pressure and 300 k. *J. Geophys. Res.*, 83(B3):1257–1268, 1978.

[63] C.-L. Fu and K.-M. Ho. First-principles calculation of the equilibrium ground-state properties of transition metals: Applications to Nb and Mo. *Phys. Rev. B*, 28(10):5480–5486, 1983.

[64] Christian Bach and Axel Groß. Semiclassical treatment of reactions at surfaces with electronic transitions. *Faraday Diss.*, 117:99–108, 2000.

[65] Matthias Scheffler and Catherine Stampfl. Theory of adsorption on metal substrates. In K. Horn and M. Scheffler, editors, *Handbook of surface science*, volume 2. Elsevier, Amsterdam, 1999.

[66] Axel Groß. Reactions at surfaces studied by ab initio dynamics calculations. *Surf. Sci. Rep.*, 32(8):291–340, 1998.

[67] W. Brenig and M. F. Hilf. Reaction dynamics of H_2 and D_2 on Si(100) and Si(111). *J. Phys.: Condens. Matter*, 13(9):R61–R94, 2001.

[68] S. Wilke and M. Scheffler. Potential-energy surface for H_2 dissociation over Pd(100). *Phys. Rev. B*, 53(8):4926–4932, 1996.

[69] Neil W. Ashcroft and N. David Mermin. *Solid State Physics.* Saunders College, 1976.

[70] Jörg Neugebauer and Matthias Scheffler. Adsorbate-substrate and adsorbate-adsorbate interactions of Na and K adlayers on Al(111). *Phys. Rev. B*, 46(24): 16067–16080, 1992.

[71] R. F. W. Bader. *Atoms in Molecules. A Quantum Theory*, volume 22 of *International Series of Monographs on Chemistry.* Oxford University Press, 1990.

[72] R. F. W. Bader. Principle of stationary action and the definition of a proper open system. *Phys. Rev. B*, 49(19):13348–13356, 1994.

[73] A. D. Becke and K. E. Edgecombe. A simple measure of electron localization in atomic and molecular systems. *J. Chem. Phys.*, 92(9):5397–5403, 1990.

[74] B. Silvi and A. Savin. Classification of chemical bonds based on topological analysis of electron localization functions. *Nature*, 371:683–686, 1994.

[75] Andreas Savin, Reinhard Nesper, Steffen Wengert, and Thomas F. Fässler. ELF: The electron localization function. *Angew. Chem. Int. Ed. Engl.*, 36:1808–1832, 1997.

[76] B. Hammer and M. Scheffler. Local chemical reactivity of a metal alloy surface. *Phys. Rev. Lett.*, 74(17):3487–3490, 1995.

[77] A. Eichler, J. Hafner, and G. Kresse. Hydrogen adsorption on the (100) surfaces of rhodium and palladium: the influence of non-local exchange-correlation interactions. *J. Phys.: Condens. Matter*, 8:7659–7675, 1996.

[78] J. Harris and S. Andersson. H_2 dissociation at metal surfaces. *Phys. Rev. Lett.*, 55(15):1583–1586, 1985.

[79] M. H. Cohen, M. V. Ganduglia-Pirovano, and J. Kudrnovský. Orbital symmetry, reactivity, and transition metal surface chemistry. *Phys. Rev. Lett.*, 72(20):3222–3225, 1994.

[80] B. Hammer and J. K. Nørskov. Why gold is the noblest of all the metals. *Nature*, 376:238–240, 1995.

[81] P. Nordlander, S. Holloway, and J. K. Nørskov. Hydrogen adsorption on metal surfaces. *Surf. Sci.*, 136:59–81, 1984.

[82] J. K. Nørskov. Chemisorption on metal surfaces. *Rep. Prog. Phys.*, 53:1253–1295, 1990.

[83] B. Hammer and J. K. Nørskov. Electronic factors determining the reactivity of metal surfaces. *Surf. Sci.*, 343:211–220, 1995.

[84] B. Hammer, Y. Morikawa, and J. K. Nørskov. CO chemisorption at metal surfaces and overlayers. *Phys. Rev. Lett.*, 76(12):2141–2144, 1996.

[85] B. Hammer, O. H. Nielsen, and J. K. Nørskov. Structure sensitivity in adsorption: CO interaction with stepped and reconstructed Pt surfaces. *Catal. Lett.*, 46:31–35, 1997.

[86] A. Ruban, B. Hammer, P. Stoltze, H. L. Skriver, and J. K. Nørskov. Surface electronic structure and reactivity of transition and noble metals. *J. Mol. Catal. A: Chem.*, 115:421–429, 1997.

[87] B. Hammer. Adsorption, diffusion, and dissociation of NO, N and O on flat and stepped Ru(0001). *Surf. Sci.*, 459:323–348, 2000.

[88] K. Christmann. Interaction of hydrogen with solid surfaces. *Surf. Sci. Rep.*, 9: 1–163, 1988.

[89] W. Dong, G. Kresse, J. Furthmüller, and J. Hafner. Chemisorption of H on Pd(111): An ab initio approach with ultrasoft pseudopotentials. *Phys. Rev. B*, 54(3):2157–2166, 1996.

[90] W. Dong and J. Hafner. H_2 dissociative adsorption on Pd(111). *Phys. Rev. B*, 56(23):15396–15403, 1997.

[91] Venkataraman Pallassana, Matthew Neurock, Lars B. Hansen, Bjørk Hammer, and Jens K. Nørskov. Theoretical analysis of hydrogen chemisorption on Pd(111), Re(0001) and Pd_{ML}/Re(0001), Re_{ML}/Pd(111) pseudomorphic overlayers. *Phys. Rev. B*, 60(8):6146–6154, 1999.

[92] S. Wilke, D. Hennig, and R. Löber. Ab initio calculations of hydrogen adsorption on (100) surfaces of palladium and rhodium. *Phys. Rev. B*, 50(4):2548–2560, 1994.

[93] S. Wilke, D. Hennig, R. Löber, M. Methfessel, and M. Scheffler. Ab initio study of hydrogen adsorption on Pd(100). *Surf. Sci.*, 307–309:76–81, 1994.

[94] S. Wilke. Microscopic mechanisms in heterogeneous catalysis: H_2 dissociation on clean and S covered Pd(100). *Appl. Phys. A*, 63:583–593, 1996.

[95] A. Eichler, G. Kresse, and J Hafner. Ab-initio calculations of the 6D potential energy surfaces for the dissociative adsorption of H_2 on the (100) surfaces of Rh, Pd and Ag. *Surf. Sci.*, 397:116–136, 1998.

[96] Andreas Eichler, Jürgen Hafner, Axel Groß, and Matthias Scheffler. Trends in the chemical reactivity of surfaces studied by ab initio quantum-dynamics calculations. *Phys. Rev. B*, 59(20):13297–13300, 1999.

[97] W. Dong, V. Ledentu, Ph. Sautet, A. Eichler, and J. Hafner. Hydrogen adsorption on palladium: a comparative theoretical study of different surfaces. *Surf. Sci.*, 411:123–136, 1998.

[98] Axel Gross, Steffen Wilke, and Matthias Scheffler. Six-dimensional quantum dynamics of adsorption and desorption of H_2 at Pd(100): Steering and steric effects. *Phys. Rev. Lett.*, 75(14):2718–2721, 1995.

[99] Axel Gross and Matthias Scheffler. *Ab initio* quantum and molecular dynamics of the dissociative adsorption of hydrogen on Pd(100). *Phys. Rev. B*, 57:2493–2506, 1998.

[100] C. Crespos, H. F. Busnengo, W. Dong, and A. Salin. Analysis of H_2 dissociation dynamics on the Pd(111) surface. *J. Chem. Phys.*, 114(24):10954–10962, 2001.

[101] Uwe Muschiol. *Wechselwirkung von Wasserstoff mit der Re(*$10\bar{1}0$*)- und der Pd(210)-Oberfläche.* PhD thesis, Freie Universität Berlin, 1998.

[102] Pia Katharina Schmidt. *Wechselwirkung von Wasserstoff mit einer Pd(210)- und Ni(210)-Oberfläche.* PhD thesis, Freie Universität Berlin, 2002.

[103] Charles Kittel. *Introduction to Solid State Physics.* John Wiley & Sons, sixth edition, 1986.

[104] M. Methfessel, D. Hennig, and M. Scheffler. Trends of the surface relaxations, surface energies, and work functions of the 4d transition metals. *Phys. Rev. B*, 46(8):4816–4829, 1992.

[105] L. Vitos, A. V. Ruban, H. L. Skriver, and J. Kollár. The surface energy of metals. *Surf. Sci.*, 411:186–202, 1998.

[106] Michael J. Mehl and Dimitrios A. Papaconstantopoulos. Applications of a tight-binding total-energy method for transition and noble metals: Elastic constants, vacancies, and surfaces of monatomic metals. *Phys. Rev. B*, 54(7):4519–4530, 1996.

[107] W. R. Tyson and W. A. Miller. Surface free energies of solid metals: Estimation from liquid surface tension measurements. *Surf. Sci.*, 62(1):267–276, 1977.

[108] G. Chiarotti, editor. *Physics of Solid Surfaces. Subvolume b: Electronic and Vibrational Properties*, volume III.24 of *Landolt-Börnstein. Numerical Data and Functional Relationships in Science and Technology. New Series.* Springer, 1994.

[109] V. L. Moruzzi, J. F. Janak, and A. R. Williams. *Calculated Electronic Properties of Metals.* Pergamon, 1978.

[110] D. Kolthoff, H. Pfnür, A. G. Fedorus, V. Koval, and A. G. Naumovets. Multilayer relaxation of Pd(210) and Mo(211). *Surf. Sci.*, 439:224–234, 1999.

[111] X.-G. Zhang, M. A. Van Hove, G. A. Somorjai, P. J. Rous, D. Tobin, A. Gonis, J. M. MacLaren, K. Heinz, M. Michl, H. Lindner, K. Müller, M. Ehsasi, and J. H. Block. Efficient determination of multilayer relaxation in the Pt(210) stepped and densely kinked surface. *Phys. Rev. Lett.*, 67(10):1298–1301, 1991.

[112] H. Okuyama, T. Nakagawa, W. Siga, N. Takagi, M. Nishijima, and T. Aruga. Subsurface hydrogen at Pd(100) induced by gas-phase atomic hydrogen. *J. Phys. Chem. B*, 103:7876–7881, 1999.

[113] Daniel Farias, Peter Schilbe, Matthias Patting, and Karl-Heinz Rieder. The transition of chemisorbed hydrogen into subsurface sites on Pd(311). *J. Chem. Phys.*, 110(1):559–569, 1999.

[114] M. Wilde, M. Matsumoto, K. Fukutani, and T. Aruga. Depth-resolved analysis of subsurface hydrogen absorbed by Pd(100). *Surf. Sci.*, 482–485:346–352, 2001.

[115] G. Herzberg and K. P. Huber. *Molecular Spectra and Molecular Structure. IV. Constants of Diatomic Molecules.* Van Nostrand Reinhold, 1979.

[116] O. Gunnarsson, B. I. Lundqvist, and J. W. Wilkins. Contribution to the cohesive energy of simple metals: Spin-dependent effect. *Phys. Rev. B*, 10(4):1319–1327, 1974.

[117] Ph. Avouris, D. Schmeisser, and J. E. Demuth. Observation of rotational exci-

tations of H_2 adsorbed on Ag surfaces. *Phys. Rev. Lett.*, 48(3):199–202, 1982.

[118] S. Andersson and J. Harris. Observation of rotational transitions for H_2, D_2 and HD adsorbed on Cu(100). *Phys. Rev. Lett.*, 48(8):545–548, 1982.

[119] A.-S. Mårtensson, C. Nyberg, and S. Andersson. Observation of molecular H_2 chemisorption on a nickel surface. *Phys. Rev. Lett.*, 57(16):2045–2048, 1986.

[120] K. Svensson, L. Bengtsson, J. Bellman, M. Hassel, M. Persson, and S. Andersson. Two-dimensional quantum rotation of adsorbed H_2. *Phys. Rev. Lett.*, 83(1):124–127, 1999.

[121] L. Bengtsson, K. Svensson, M. Hassel, J. Bellman, M. Persson, and S. Andersson. H_2 adsorbed in a two-dimensional quantum rotor state on a stepped copper surface. *Phys. Rev. B*, 61(24):16921–16932, 2000.

[122] Georg Kresse. Dissociation and sticking of H_2 on the Ni(111), (100) and (110) substrate. *Phys. Rev. B*, 62(12):8295–8305, 2000.

[123] Ali Alavi, Peijun Hu, Thierry Deutsch, Pier Luigi Silvestrelli, and Jürg Hutter. CO oxidation on Pt(111): An ab initio density functional theory study. *Phys. Rev. Lett.*, 80(16):3650–3653, 1998.

[124] Zhi-Pan Liu and P. Hu. General trends in CO dissociation on transition metal surfaces. *J. Chem. Phys.*, 114(19):8244–8247, 2001.

[125] A. Logadottir, T. H. Rod, J. K. Nørskov, B. Hammer, S. Dahl, and C. J. H. Jacobsen. The Brønsted-Evans-Polanyi relation and the volcano plot for ammonia synthesis over transition metal catalysts. *J. Catal.*, 197:229–231, 2001.

[126] A. Eichler, G. Kresse, and J. Hafner. Quantum steering effects in the dissociative adsorption of H_2 on Rh(100). *Phys. Rev. Lett.*, 77(6):1119–1122, 1996.

[127] Gregory Mills, Hannes Jónsson, and Gregory K. Schenter. Reversible work transition state theory: application to dissociative adsorption of hydrogen. *Surf. Sci.*, 324:305–337, 1995.

[128] Graeme Henkelman and Hannes Jónsson. Improved tangent estimate in the nudged elastic band method for finding minimum energy paths and saddle points. *J. Chem. Phys.*, 113(22):9978–9985, 2000.

[129] Graeme Henkelman, Blas P. Uberuaga, and Hannes Jónsson. A climbing image nudged elastic band method for finding saddle points and minimum energy paths. *J. Chem. Phys.*, 113(22):9901–9904, 2000.

[130] George Blyholder. Molecular orbital view of chemisorbed carbon monoxide. *J. Phys. Chem.*, 68(10):2772–2778, 1964.

[131] P. Hu, D. A. King, M.-H. Lee, and M. C. Payne. Orbital mixing in CO chemisorption on transition metal surfaces. *Chem. Phys. Lett.*, 246:73–78, 1995.

[132] Hideaki Aizawa and Shinji Tsuneyuki. First-principles study of CO bonding to Pt(111): validity of the Blyholder model. *Surf. Sci.*, 399:L364–L370, 1998.

[133] H. Conrad, G. Ertl, J. Koch, and E. E. Latta. Adsorption of CO on Pd single crystal surfaces. *Surf. Sci.*, 43:462–480, 1974.

[134] A. M. Bradshaw and F. M. Hoffmann. The chemisorption of carbon monoxide on palladium single crystal surfaces: IR spectroscopic evidence for localised site

adsorption. *Surf. Sci.*, 72:513–535, 1978.

[135] Theodore E. Madey, John T. Yates, Jr., A. M. Bradshaw, and F. M. Hoffmann. Evidence for "inclined" CO on Pd(210). *Surf. Sci.*, 89:370–380, 1979.

[136] R. J. Behm, K. Christmann, G. Ertl, and M. A. Van Hove. Adsorption of CO on Pd(100). *J. Chem. Phys.*, 73:2984–2995, 1980.

[137] A. Eichler and J. Hafner. Adsorption of CO on Pd(100): Steering into less favored adsorption sites. *Phys. Rev. B*, 57(16):10110–10114, 1998.

[138] Karoliina Honkala, Päivi Pirilä, and Kari Laasonen. CO and NO adsorption and co-adsorption on the Pd(111) surface. *Surf. Sci.*, 489:72–82, 2001.

[139] M. K. Rose, T. Mitsui, J. Dunphy, A. Borg, D. F. Ogletree, M. Salmeron, and P. Sautet. Ordered structures of CO on Pd(111) studied by STM. *Surf. Sci.*, 512:48–60, 2002.

[140] M. Kittel, R. Terborg, M. Polcik, A. M. Bradshaw, R. L. Toomes, D. P. Woodruff, and E. Rotenberg. The structure of the Pd(110)(2 × 1)-CO surface. *Surf. Sci.*, 511:34–42, 2002.

[141] M. Hirsimäki and M. Valden. Adsorption and thermal behavior of CO and NO on Pd{110} and Pd{320}. *J. Chem. Phys.*, 114(5):2345–2354, 2001.

[142] Hiroyuki S. Kato, Hiroshi Okuyama, Jun Yoshinubo, and Maki Kawai. Estimation of direct and indirect interactions between CO molecules on Pd(110). *Surf. Sci.*, 513:239–248, 2002.

[143] R. D. Ramsier, K.-W. Lee, and J. T. Yates, Jr. CO adsorption on stepped Pd(112): studies by thermal and electron stimulated desorption. *Surf. Sci.*, 322: 243–255, 1995.

[144] Shinichi Katsuki and Hiroshi Taketa. Theoretical study of electronic structure for "inclined" CO chemisorbed on Pd(210) surface. *Solid State Comm.*, 39:711–713, 1981.

[145] Frank W. Kutzler and G. S. Painter. Energies of atoms with nonspherical charge densities calculated with nonlocal density-functional theory. *Phys. Rev. Lett.*, 59 (12):1285–1288, 1987.

[146] E. Christoffersen, P. Stoltze, and J. K. Nørskov. Monte Carlo simulations of adsorption-induced segregation. *Surf. Sci.*, 505:200–214, 2002.

[147] A. Föhlisch, M. Nyberg, P. Bennich, L. Triguero, J. Hasselström, O. Karis, L. G. M. Pettersson, and A. Nilsson. The bonding of CO to metal surfaces. *J. Chem. Phys.*, 112(4):1946–1958, 2000.

[148] A. Föhlisch, M. Nyberg, J. Hasselström, O. Karis, L. G. M. Pettersson, and A. Nilsson. How carbon monoxide adsorbs in different sites. *Phys. Rev. Lett.*, 85 (15):3309–3312, 2000.

[149] L. Westerlund, L. Jönsson, and S. Andersson. Formation of chemisorbed H_2 in the Ni(100)-H-CO coadsorption system. *Surf. Sci.*, 187:L669–L674, 1987.

[150] Jeff Greeley and Manos Mavrikakis. A first-principles study of methanol decomposition on Pt(111). *J. Am. Chem. Soc.*, 124:7193–7201, 2002.

[151] M. Mavrikakis, B. Hammer, and J. K. Nørskov. Effect of strain on the reactivity

of metal surfaces. *Phys. Rev. Lett.*, 81(13):2819–2822, 1998.

[152] M. Gsell, P. Jakob, and D. Menzel. Effect of substrate strain on adsorption. *Science*, 280:717–720, 1998.

[153] A. Schlapka, M. Lischka, A. Groß, and P. Jakob. Surface strain versus substrate interaction in heteroepitaxial metal layers: Pt on Ru(0001). 2003. Submitted to Phys. Rev. Lett.

[154] D. Spišák, R. Lorenz, and J. Hafner. Structure and magnetism in thin films and multilayers of hexagonal ruthenium and iron. *Phys. Rev. B*, 63:094424, 2001.

[155] H. Over, H. Bludau, M. Skottke-Klein, G. Ertl, W. Moritz, and C. T. Campbell. Coverage dependence of adsorption-site geometry in the Cs/Ru(0001) system: A low energy-electron-diffraction analysis. *Phys. Rev. B*, 45(15):8638–8649, 1992.

[156] P. Légaré, N. J. Castellani, and G. F. Cabeza. Adhesion of metal on metal. The Pt on Co case. *Surf. Sci.*, 496:L51–L54, 2002.

[157] H. Steininger, S. Lehwald, and H. Ibach. Adsorption of oxygen on Pt(111). *Surf. Sci.*, 123:1–17, 1982.

[158] U. Starke, N. Materer, A. Barbieri, R. Döll, K. Heinz, M. A. Van Hove, and G. A. Somorjai. A low-energy electron diffraction study of oxygen, water and ice adsorption on Pt(111). *Surf. Sci.*, 287/288:432–437, 1993.

[159] N. Materer, U. Starke, A. Barbieri, R. Döll, K. Heinz, M. A. Van Hove, and G. A. Somorjai. Reliability of detailed LEED structural analyses: Pt(111) and Pt(111)-p(2x2)-O. *Surf. Sci.*, 325:207–222, 1995.

[160] A. N. Artsyukhovich, V. A. Ukraintsev, and I. Harrison. Low temperature sticking and desorption dynamics of oxygen on Pt(111). *Surf. Sci.*, 347:303–318, 1996.

[161] Ulrika Engström and Roger Ryberg. Atomic oxygen on a Pt(111) surface studied by infrared spectroscopy. *Phys. Rev. Lett.*, 82(13):2741–2744, 1999.

[162] Dmitri I. Jerdev, Jooho Kim, Matthias Batzill, and Bruce E. Koel. Evidence for slow oxygen exchange between multiple adsorption sites at high oxygen coverages on Pt(111). *Surf. Sci.*, 498:L91–L96, 2002.

[163] Peter J. Feibelman, Stefanie Esch, and Thomas Michely. O binding sites on stepped Pt(111) surfaces. *Phys. Rev. Lett.*, 77(11):2257–2260, 1996.

[164] Peter J. Feibelman. d-electron frustration and the large fcc versus hcp binding preference in O adsorption on Pt(111). *Phys. Rev. B*, 56(16):10532–10537, 1997.

[165] Peter J. Feibelman, J. Hafner, and G. Kresse. Vibrations of O on stepped Pt(111). *Phys. Rev. B*, 58(4):2179–2184, 1998.

[166] Alexander Bogicevic, Johan Strömquist, and Bengt I. Lundqvist. First-principles diffusion-barrier calculation for atomic oxygen on Pt(111). *Phys. Rev. B*, 57(8): R4289–R4292, 1998.

[167] Anton Kokalj, Antonija Lesar, Milan Hodošček, and Mauro Causà. Periodic DFT study of the Pt(111): A p(1×1) atomic oxygen interaction with the surface. *J. Phys. Chem. B*, 103:7222–7232, 1999.

[168] M. Lindroos, H. Pfnür, G. Held, and D. Menzel. Adsorbate induced reconstruction by strong chemisorption: Ru(001)$p(2 \times 2)$-O. *Surf. Sci.*, 222:451–463, 1989.

[169] C. Stampfl, S. Schwegmann, H. Over, M. Scheffler, and G. Ertl. Structure and stability of a high-coverage (1 × 1) oxygen phase on Ru(0001). *Phys. Rev. Lett.*, 77(16):3371–3374, 1996.

[170] C. Stampfl and M. Scheffler. Theoretical study of O adlayers on Ru(0001). *Phys. Rev. B*, 54(4):2868–2872, 1996.

[171] Ata Roudgar and Axel Groß. Local reactivity of metal overlayers: Density functional theory calculations of Pd on Au. *Phys. Rev. B*, 67(3):033409, 2003.

[172] B. Hammer. Adsorbate-oxide interactions during the NO + CO reaction on MgO(100) supported Pd monolayer films. *Phys. Rev. Lett.*, 89(1):016102, 2002.

[173] Harald Ibach and Douglas L. Mills. *Electron energy loss spectroscopy and surface vibrations.* Academic Press, 1982.

[174] C. Puglia, A. Nilsson, B. Hernnäs, O. Karis, P. Bennich, and N. Mårtensson. Physisorbed, chemisorbed and dissociated O_2 on Pt(111) studied by different core level spectroscopy methods. *Surf. Sci.*, 342:119–133, 1995.

[175] P. D. Nolan, B. R. Lutz, P. L. Tanaka, J. E. Davis, and C. B. Mullins. Translational energy selection of molecular precursors to oxygen adsorption on Pt(111). *Phys. Rev. Lett.*, 81(15):3179–3182, 1998.

[176] P. D. Nolan, B. R. Lutz, P. L. Tanaka, J. E. Davis, and C. B. Mullins. Molecularly chemisorbed intermediates to oxygen adsorption on Pt(111): A molecular beam and electron energy-loss spectroscopy study. *J. Chem. Phys.*, 111(8):3696–3704, 1999.

[177] A. Groß, A. Eichler, J. Hafner, M. J. Mehl, and D. A. Papaconstantopoulos. Unified picture of the molecular adsorption process: O_2/Pt(111). Submitted to Surf. Sci. Lett., 2003.

[178] A. Eichler and J. Hafner. Molecular precursors in the dissociative adsorption of O_2 on Pt(111). *Phys. Rev. Lett.*, 79(22):4481–4484, 1997.

[179] A. Eichler, F. Mittendorfer, and J. Hafner. Precursor-mediated adsorption of oxygen on the (111) surfaces of platinum-group metals. *Phys. Rev. B*, 62(7): 4744–4755, 2000.

[180] P. Gambardella, Ž. Šljivančanin, B. Hammer, M. Blanc, K. Kuhnke, and K. Kern. Oxygen dissociation at Pt steps. *Phys. Rev. Lett.*, 87(5):056103, 2001.

[181] Ž. Šljivančanin and B. Hammer. Oxygen dissociation at close-packed Pt terraces, Pt steps, and Ag-covered Pt steps studied with density functional theory. *Surf. Sci.*, 515:235–244, 2002.

[182] D. F. Ogletree, M. A. Van Hove, and G. A. Somorjai. LEED intensity analysis of the structures of clean Pt(111) and of CO adsorbed on Pt(111) in the c(4 × 2) arrangement. *Surf. Sci.*, 173(2–3):351–365, 1986.

[183] Peter J. Feibelman, B. Hammer, J. K. Nørskov, F. Wagner, M. Scheffler, R. Stumpf, R. Watwe, and J. Dumesic. The CO/Pt(111) puzzle. *J. Phys. Chem. B*, 105:4018–4025, 2001.

[184] F. Buatier de Mongeot, M. Scherer, B. Gleich, E. Kopatzki, and R. J. Behm. CO adsorption and oxidation on bimetallic Pt/Ru(0001) surfaces – a combined STM

and TPD/TPR study. *Surf. Sci.*, 411:249–262, 1998.

[185] Q. Ge, S. Desai, M. Neurock, and K. Kourtakis. CO adsorption on Pt-Ru surface alloys and on the surface of Pt-Ru bulk alloy. *J. Phys. Chem. B*, 105:9533–9536, 2001.

[186] E. Christoffersen, P. Liu, A. Ruban, H. L. Skriver, and J. K. Nørskov. Anode materials for low-temperature fuel cells: A density functional theory study. *J. Catal.*, 199:123–131, 2001.

[187] K. Bleakley and P. Hu. A density functional theory study of the interaction between CO and O on a Pt surface: CO/Pt(111), O/Pt(111), and CO/O/Pt(111). *J. Am. Chem. Soc.*, 121:7644–7652, 1999.

[188] A. Eichler and J. Hafner. Reaction channels for the catalytic oxidation of CO on Pt(111). *Phys. Rev. B*, 59(8):5960–5967, 1999.

[189] Andreas Eichler. CO oxidation on transition metal surfaces: reaction rates from first principles. *Surf. Sci.*, 498:314–320, 2002.

[190] D. Geschke, T. Baştuğ, T. Jacob, S. Fritzsche, W.-D. Sepp, B. Fricke, S. Varga, and J. Anton. Adsorption of CO on cluster models of platinum (111): A four-component relativistic density functional approach. *Phys. Rev. B*, 64:235411, 2001.

[191] Ilya Grinberg, Yashar Yourdshahyan, and Andrew M. Rappe. CO on Pt(111) puzzle: A possible solution. *J. Chem. Phys.*, 117(5):2264–2270, 2002.

[192] Y. Y. Yeo, L. Vattuone, and D. A. King. Calorimetric heats for CO and oxygen adsorption and for the catalytic CO oxidation reaction on Pt{111}. *J. Chem. Phys.*, 106(1):392–401, 1997.

[193] Y. Gauthier, M. Schmid, S. Padovani, E. Lundgren, V. Buš, G. Kresse, J. Redinger, and P. Varga. Adsorption sites and ligand effect for CO on an alloy surface: A direct view. *Phys. Rev. Lett.*, 87(3):036103, 2001.

[194] N. V. Petrova and I. N. Yakovkin. Lateral interaction and CO adlayer structures on the Pt(111) surface. *Surf. Sci.*, 519:90–100, 2002.

[195] W. Kohn. An essay on condensed matter physics in the twentieth century. *Rev. Mod. Phys.*, 71(2):S59–S77, 1999.

[196] A. Eichler, J. Hafner, J. Furthmüller, and G. Kresse. Structural and electronic properties of rhodium surfaces: an ab initio approach. *Surf. Sci.*, 346:300–321, 1996.

[197] Stephen Wolfram. *The Mathematica book.* Wolfram Media, 4th edition, 1999.

List of Publications

1. Pia K. Schmidt, Klaus Christmann, Georg Kresse, Jürgen Hafner, Markus Lischka, and Axel Groß. Coexistence of atomic and molecular chemisorption states: H_2/Pd(210). *Phys. Rev. Lett.*, 87:096103, 2001.
2. Markus Lischka and Axel Groß. Hydrogen adsorption on an open metal surface: H_2/Pd(210). *Phys. Rev. B*, 65:075420, 2002.
3. Markus Lischka and Axel Groß. Hydrogen on palladium: a model system for the interaction of atoms and molecules with metal surfaces. To appear in a review volume on *Developments in Vacuum Science and Technology*, Research Signpost, 2002.